X-RAY SPECTRAL AND TIMING STUDIES OF THE HIGH MASS X-RAY BINARY PULSAR 4U 1907+09

A THESIS SUBMITTED TO
THE GRADUATE SCHOOL OF NATURAL AND APPLIED SCIENCES
OF
MIDDLE EAST TECHNICAL UNIVERSITY

BY

ŞEYDA ŞAHİNER

IN PARTIAL FULFILLMENT OF THE REQUIREMENTS
FOR
THE DEGREE OF MASTER OF SCIENCE
IN
PHYSICS

SEPTEMBER 2009

Approval of the thesis:

**X-RAY SPECTRAL AND TIMING STUDIES
OF THE HIGH MASS X-RAY BINARY PULSAR 4U 1907+09**

submitted by **ŞEYDA ŞAHİNER** in partial fulfillment of the requirements for the degree of **Master of Science in Physics Department, Middle East Technical University** by,

Prof. Dr. Canan Özgen
Dean, Graduate School of **Natural and Applied Sciences** _____________________

Prof. Dr. Sinan Bilikmen
Head of Department, **Physics** _____________________

Prof. Dr. Altan Baykal
Supervisor, **Physics Dept., METU** _____________________

Assist. Prof. Dr. S. Çağdaş İnam
Co-Supervisor, **E.E. Dept., Başkent University** _____________________

Examining Committee Members:

Prof. Dr. Ümit Kızıloğlu
Physics Dept., METU _____________________

Prof. Dr. Altan Baykal
Physics Dept., METU _____________________

Prof. Dr. Berahitdin Albayrak
Astronomy and Space Sciences Dept. Ankara University _____________________

Assist. Prof. Dr. S. Kaan Yerli
Physics Dept., METU _____________________

Assist. Prof. Dr. S. Çağdaş İnam
Electrical and Electronics Eng. Dept., Başkent University _____________________

Date: _____________________

I hereby declare that all information in this document has been obtained and presented in accordance with academic rules and ethical conduct. I also declare that, as required by these rules and conduct, I have fully cited and referenced all material and results that are not original to this work.

Name, Last name : Şeyda Şahiner

Signature :

ABSTRACT

X-RAY SPECTRAL AND TIMING STUDIES
OF THE HIGH MASS X-RAY BINARY PULSAR 4U 1907+09

Şahiner, Şeyda
M.S., Department of Physics
Supervisor: Prof. Dr. Altan Baykal
Co-Supervisor: Assist. Prof. Dr. S. Çağdaş İnam

September 2009, 105 pages

In this thesis, X-ray spectral and pulse timing analysis of the high mass X-ray binary pulsar 4U 1907+09, based on the observations with *Rossi X-ray Timing Explorer* (*RXTE*) and *International Gamma-Ray Astrophysics Laboratory* (*INTEGRAL*), are presented. *INTEGRAL* (October 2005 - November 2007) and *RXTE* (June 2007 - December 2008) observations confirm that the luminosity of the source is highly variable such that, flaring and dipping activities are observed.

The results of time-averaged energy spectra of *RXTE* and *INTEGRAL* observations are consistent with the previous studies. Orbital phase resolved spectroscopy with *RXTE* data, reveals that the Hydrogen column density varies through the orbit reaching to its maximum value just after periastron. This variation approves that the location of the absorbing material is the accretion flow. A slight spectral softening with increasing luminosity is aslo observed.

4U 1907+09 had been steadily spinning down for more than ~15 years with a rate of -3.54×10^{-14} Hz s^{-1}. *RXTE* observations of the source in 2001 showed a ~60% decrease in the spin-down rate and *INTEGRAL* observations in 2003 showed a

reversal to spin-up. The timing analysis presented in this thesis reveals a new spin-down episode with a rate of -3.59×10^{-14} Hz s^{-1}, which is close to the previous steady spin-down rate. This result implies that a recent torque reversal before June 2007 has taken place. The reversal is a rare event for 4U 1907+09 and it indicates the variations in the mass accretion rate and/or geometry.

Using *RXTE* observations, 24 new pulse periods are measured to demonstrate the period evolution. Energy resolved pulse profiles confirm that the profile has a double peak sinusoidal shape at energies below 20 keV, whereas the leading peak significantly loses its intensity above 20 keV. This energy dependence indicates that the physical circumstances of the two polar caps are different.

Keywords: Accretion, accretion disks, accretion torques, neutron stars, accretion powered pulsars, X-ray binaries, 4U 1907+09

ÖZ

YÜKSEK KÜTLELİ X-IŞINI ÇİFT YILDIZ SİSTEMİ ATARCASI
4U 1907+09 UN X-IŞINI TAYFSAL VE ZAMANLAMA ÇALIŞMALARI

Şahiner, Şeyda

Yüksek Lisans, Fizik Bölümü

Tez Yöneticisi: Prof. Dr. Altan Baykal

Ortak Tez Yöneticisi: Yrd. Doç. Dr. S. Çağdaş İnam

Eylül 2009, 105 sayfa

Bu tezde, *RXTE* ve *INTEGRAL* gözlemlerine dayanarak, yüksek kütleli X-ışını çift yıldız sistemi atarcası 4U 1907+09'un X-ışını tayfsal ve zamanlama çalışmaları sunulmaktadır. *INTEGRAL* (Ekim 2005 - Kasım 2007) ve *RXTE* (Haziran 2007 - Aralık 2008) gözlemleri parlama ve düşüşler gösterek, kaynağın değişken parlaklıkta oldugunu doğrulamaktadır.

RXTE ve *INTEGRAL* gözlemlerinin ortalama enerji tayflarından elde edilen sonuçlar önceki çalışmalarla uyumludur. *RXTE* verileri ile çeşitli yörünge evrelerinde yapılan tayf ölçümleri; hidrojen kolon yoğunluğunun, enberiden hemen sonra en yüksek değerine ulaşarak, yörünge boyunca değişim gösterdiğini ortaya çıkarmıştır. Bu değişim, soğurucu maddenin konumunun kütle aktarım akarı olduğunu onaylamaktadır. Bunun yanı sıra, parlaklıktaki artışla birlikte zayıf bir tayfsal yumuşama gözlenmiştir.

Yaklaşık 15 yıldan uzun bir süredir, 4U 1907+09'un dönme frekansı sabit hızla (-3.54×10^{-14} Hz s^{-1}) azalmaktaydı. Kaynağın 2001'deki *RXTE* gözlemleri bu hızda ~%60'lık bir azalma oldugunu göstermişti. 2003'teki *INTEGRAL* gözlemleri ise frekansın artmaya başladığını ortaya çıkarmıştı. Bu tezde sunulan zamanlama

analizleri, -3.59×10^{-14} Hz s^{-1} frekans hızı ile yeni bir azalma dönemini ortaya çıkarmıştır. Bu sonuç, Haziran 2007'den önce kütle aktarım torkunun yönünde bir değişim gerektirmektedir. 4U 1907+09 için, tork yönünde değişim nadir bir olaydır ve kütle aktarım hızında ve/veya geometrisinde değişimler oldugunu belirtir.

Atım periyodunun değişimini göstermek amacıyla, *RXTE* gözlemlerini kullanarak 24 periyot hesaplanmıştır. Enerjiye göre çözümlenmiş atım profilleri; 20 keV'nin altında profilin çift tepeli sinüsoidal bir şekile sahip olduğunu, fakat 20 keV'nin üstünde öncü tepenin önemli miktarda parlaklık kaybettiğini onaylamaktadır. Bu enerji bağıntısı iki kutup takkesinin fiziksel koşullarının farklı olduğunu belirtmektedir.

Anahtar kelimeler: Kütle aktarımı, kütle aktarım diskleri, kütle aktarım torkları, nötron yıldızları, aktarım güçlü atarcalar, X-ışını çift yıldız sistemleri, 4U 1907+09

ACKNOWLEDGMENTS

I owe my deepest gratitude to Prof. Dr. Altan Baykal for his invaluable supervision, continuous guidance and encouragement throughout my graduate study. I also gratefully acknowledge my co-supervisor Assist. Prof. Dr. S. Çağdaş İnam for his crucial contribution to this research. It would have been harder to conclude this thesis without their scientific perception, which remarkably inspire and enrich my growth as a student. It is a pleasure to pay tribute also to Assoc. Prof. Dr. Şölen Balman for the assistance she provided at all levels of data analysis and for her constructive comments.

I would like to thank my colleagues in METU Astrophysics group for useful discussions and moral motivation. I especially thank to Elif Beklen who gently grants me her time for coping with my plenty of questions. I also appreciate the friendship and endurance of my office mates, Mehtap Özbey and Yakup Pekön.

I am especially indebted to my parents, for the love, trust and support they provided me throughout my entire life. I would like to show my gratitude to my uncle Eray Paksoy who encouraged me for my graduate study. I must emphasize that I owe him very much for his guidance throughout my childhood.

I thank all my friends with whom I spent spare times to relax and entertain during the stressful thesis writing period. They tolerated all my tiresome complaints and helped me to feel confident to carry on. I especially thank to S. Eren Özmen for his love, patience and editing assistance.

I acknowledge the scholarship from The Scientific and Technological Research Council of Turkey (TÜBİTAK) through the project 106T040 and support from EU FP6 Transfer of Knowledge Project "Astrophysics of Neutron Stars" (MTKD-CT-2006-042722).

TABLE OF CONTENTS

LIST OF TABLES

LIST OF FIGURES

LIST OF ABBREVIATIONS

ADAF	Advection Dominated Accretion Flow
ASCA	Advanced Satellite for Cosmology and Astrophysics
ASM	All-Sky Monitor
BATSE	Burst and Transient Source Experiment
BeppoSAX	Beppo Satellite per Astronomia X
Be/XB	High Mass X-ray Binary with Be type Companion Star
CGRO	Compton Gamma-Ray Observatory
CRSF	Cyclotron Resonance Scattering Feature
EXOSAT	European Space Agency's X-ray Observatory Satellite
EW	Equivalent Width
FOV	Field of View
FWHM	Full width at Half Maximum
GOF	Guest Observer Facility
HEAO 1	High Energy Astronomy Observatory 1
HEXTE	High Energy X-ray Timing Experiment
HMXB	High Mass X-ray Binary
IBIS	Imager on Board the INTEGRAL Satellite
INTEGRAL	International Gamma-Ray Astrophysics Laboratory
ISDC	INTEGRAL Science Data Centre
ISGRI	INTEGRAL Soft Gamma-Ray Imager
IXAE	Indian X-Ray Astronomy Experiment

JEM-X	Joint European X-ray Monitor
LMC	Large Magellanic Clouds
LMXB	Low Mass X-ray Binary
MJD	Modified Julian Date
NFI	Narrow Field Instrument
NPEX	Negative and Positive power laws with common Exponential cutoff
OMC	Optical Monitoring Camera
OSO 7	Orbiting Solar Observatory 7
QPO	Quasi-Periodic Oscillation
PCA	Proportional Counter Array
PCU	Proportional Counter Unit
PIF	Pixel Illuminated Fraction
PL	Power Law
RLO	Roche Lobe Overflow
ROSAT	Roentgen Satellite
RXTE	Rossi X-ray Timing Explorer
SAS 3	Small Astronomy Satellite 3
SCW	Science Window
SG/XB	High Mass X-ray Binary with OB type Supergiant Companion Star
SMC	Small Magellanic Clouds
SNR	Signal to Noise Ratio
SPI	Spectrometer on INTEGRAL
XMM	X-ray Multi-Mirror Mission
XMPC	Zenon-filled Multi-layer Proportional Counter

CHAPTER 1

INTRODUCTION

The existence of neutron stars was foreseen in early 1930s by the theories predicting their birth in supernova explosions (Baade & Zwicky 1934). The discovery of the first extrasolar X-ray source Sco X-1 (Giacconi et al. 1962) turned out to be the initial evidence of thermal emission from neutron stars. The essentials of standard model for accreting neutron stars were established through the classification of Sco X-1 as a close binary system where stream of gas flows from the companion onto the neutron star (Shklovskii 1967). Soon after, the detection of periodic X-ray pulsations from two eclipsing binaries Cen X-3 (Giacconi et al. 1971b) and Her X-1 (Tananbaum et al. 1972) with NASA's first X-ray astronomy satellite *Uhuru*, confirmed that these sources are actually accretion powered pulsars. So far, the number of known accretion powered pulsars has grown to be ~110 (Ghosh 2007), with X-ray surveys performed by satellites such as *Uhuru, Ariel V, SAS 3, HEAO 1, Einstein, Tenma, EXOSAT, Ginga, ROSAT, RXTE, BeppoSAX, IXAE, XMM-Newton, Chandra* and *INTEGRAL.*

Identifying binary X-ray pulsars as rotating, accreting neutron stars; the source of power for the X-ray emission is accretion (Lamb et al. 1973). Typically, bright binary X-ray pulsars have X-ray luminosities $\sim 10^{37}$ erg s^{-1}, which require accretion rates $\sim 10^{-9}$ $M_{\odot}$ yr^{-1}. The binary companion of the neutron star is also called the mass donor of the system, since it supplies necessary matter to be accreted by losing mass through a variety of processes such as stellar wind or Roche lobe overflow (RLO). As the stream of matter approaches to the neutron star, it is disrupted by the strong magnetic field ($\sim 10^{12}$ G) of the neutron star, funneled along the field lines onto the magnetic poles and produces 'hot spots' on the polar caps (see Figure 1.1). While the accreting matter reaches the stellar surface, the release of its

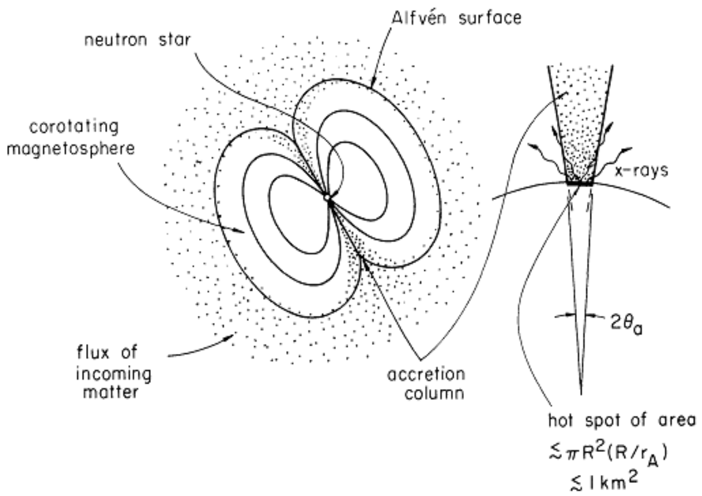

Figure 1.1: Basic diagram of accretion onto a magnetic neutron star. The left side of the figure is an overall view showing Alfvén surface, magnetic configuration and accreting matter (*dots*). The right side is a close-up view of the accretion column on the hot spot which produces X-ray emission. (Lamb et al. 1973)

gravitational energy is converted into electromagnetic radiation, primarily X-rays. If the magnetic and rotation axes of the neutron star are misaligned, the beamed emission from the hot spots is modulated with the rotation period. When the beams pass through the line of sight of the observer, a pulsation in the X-ray intensity is observed. So called ‘accretion powered pulsars’ are the neutron stars which pulsate in this manner. Pulse periods of accretion powered pulsars known so far range from 2 ms to 10^4 s (Ghosh 2007).

About 68 of the ~110 known accretion powered pulsars are in our galaxy, Milky Way; 32 in the Small Magellanic Clouds (SMC), 6 in Large Magellanic Clouds (LMC) (see Table E.1 of Ghosh 2007). The population is mostly distributed in the galactic plane (see Figure 1.2) while SMC and LMC pulsars are significantly away from the galactic plane. The distribution of pulsars in Milky Way rather depends on the mass and age of the binary system. The disk population consists of High Mass X-ray Binaries (HMXBs) and the bulge population consists of Low Mass X-ray Binaries (LMXBs). The distribution of the pulse periods of accretion powered pulsars are shown in Figure 1.3. The galactic population seems to have longer periods, which can be a selection effect (Laycock et al. 2005).

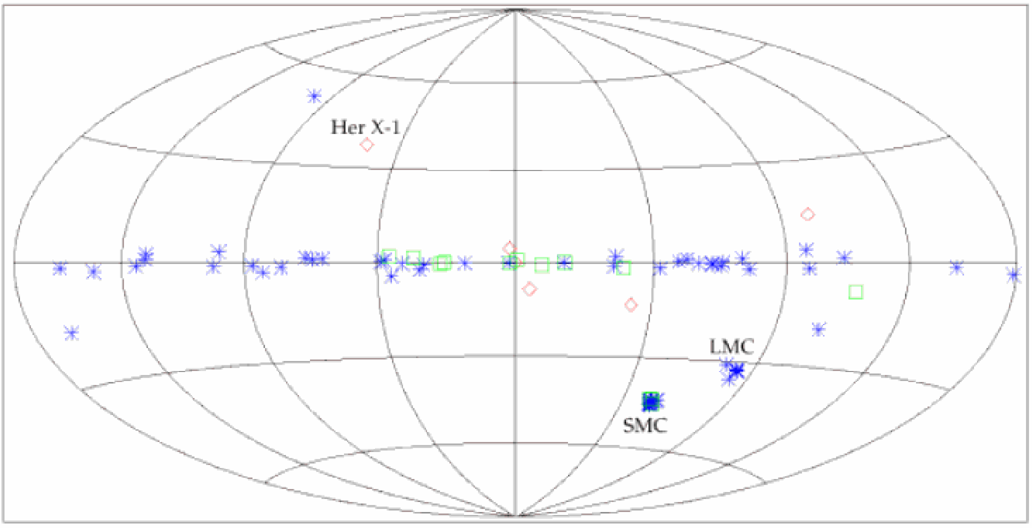

Figure 1.2: Distribution of accretion powered pulsars in galactic coordinates (Ghosh 2007). *Asterisks:* pulsars in HMXBs. *Diamonds:* pulsars in LMXBs. *Squares:* pulsars with uncertain binary classification.

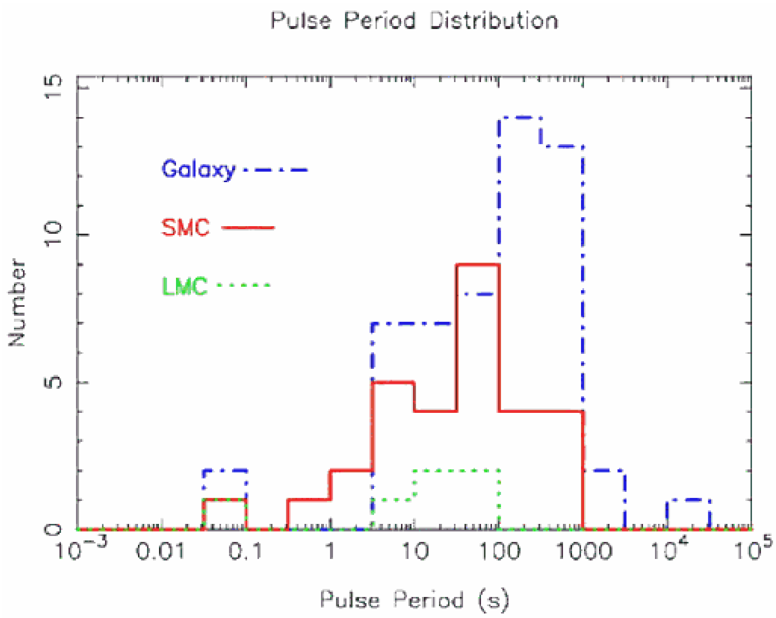

Figure 1.3: Distribution of the pulse periods of accretion powered pulsars (Laycock et al. 2005).

X-ray pulsars powered by accretion can be classified into three groups according to the characteristics of the mass donor companion star (Nagase 1989): I) LMXBs, II) HMXBs with main sequence B*e* star companions (B*e*/XBs), III) HMXBs with evolved O or B type supergiant companions (SG/XBs). Mainly, LMXBs have low mass ($M_c \leq 2\ M_\odot$); old, late type or degenerate dwarf companions while HMXBs have massive ($M_c \geq 6\ M_\odot$), young, O or B type companions.

I) LMXBs:

Although the galactic population of LMXBs is crowded, the majority does not shelter a pulsar for the reason that their weak magnetic fields ($\leq 10^9$ G) cannot affect the accretion flow significantly. The LMXBs containing accretion powered pulsars form a minor group with ~11 known systems. 7 of these systems constitute a recently developed class of objects; the accreting millisecond pulsars (Wijnands 2004). The other 4 systems do not have common characteristics (Bildsten et al. 1997 and references therein). The mass donors are a main sequence A star (Her X-1), a degenerate dwarf ($M_c \leq 0.1\ M_\odot$) (4U 1626-67), and two red giants (GX 1+4 and GRO J1744-28).

Low mass companion stars do not have strong stellar winds to feed the accretion flow (White et al. 1995). Close LMXBs are brought into contact by loss of orbital angular momentum due to gravitational radiation and/or magnetic braking. In these systems, the companion fills its critical gravitational potential lobe (i.e Roche lobe) not because of its nuclear evolution and consequent expansion but because of its shrinking orbit, since its potential lobe shrinks proportionally. So, the main mass transfer process is RLO which supplies gas to the compact object via an accretion disk.

II) B*e*/XBs:

B*e*/XBs form a major group in HMXBs. There are ~61 known B*e*/XBs containing accretion powered pulsars (4U 0115+63, V 0332+53, A 0535+26, 4U1145-619, GX 304-1, 2S 1417-624, EXO 2030+375 etc.). The naming 'B*e*' refers to the characterization of the companion by emission lines in the optical spectrum (mostly Balmer series), which arise from its circumstellar envelope (Slettebak 1988, Apparao 1994). The mass donor lying well inside its Roche Lobe, the mass transfer process is the dense stellar wind which forms an envelope of high density matter confined at the equatorial regions of the B*e* star. The compact object interacts with this envelope and produces X-rays by accreting matter.

Generally, the X-ray emission from these systems are of transient nature, showing outbursts during mass ejection episodes of the B*e* star. Two different types of outbursts are classified as Type I and Type II. Type I outbursts usually occur periodically and correlated with periastron passage of the compact object in its eccentric orbit. Type II outbursts are irregular activities with higher luminosities peaking at arbitrary orbital phases. Several authors have explained the enormous increase in the X-ray intensity during Type II outbursts with the formation of a transient accretion disk, in contrast quiescent episodes are explained by the propeller mechanism inhibiting accretion via the centrifugal barrier (Stella et al. 1986, Motch et al. 1991).

Corbet (1984) demonstrated a strong, positive correlation between the spin period, $P_{\rm spin}$, and the orbital period, $P_{\rm orb}$, of B*e*/XBs which can be described by a power-law relation $P_{\rm spin} \propto P_{\rm orb}^{\alpha}$ with the exponent in the range α ~1 - 1.5 (see Figure 1.4). It has been suggested that the neutron stars tend to adjust their $P_{\rm spin}$, according to the changing conditions of the stellar winds of B*e* companions, by reaching their equilibrium periods, $P_{\rm eq}$ (Waters & van Kerkwijk 1989). $P_{\rm eq}$ is inversely proportional to the accretion rate with a relation like $P_{\rm eq} \propto \dot{M}^{-3/7}$. Thus, as the orbit is wider accreting matter is supplied from the outer, lower density parts of the equatorial disk of the B*e* star, resulting in a lower accretion rate and a longer $P_{\rm spin}$.

III) SG/XBs:

The other group of HMXBs containing accretion powered pulsars is formed by the systems which the companion star is an evolved massive (~15 - 30 $M_{\odot}$), supergiant of O or B type. So far, the number of systems of this group is known to be ~13 (Vela X-1, Cen X-3, GX 301-2, 4U 1538-52, OAO 1657-415, 4U 1907+09 etc.), 2 of which are in the Magellanic Clouds (SMC X-1 and LMC X-4).

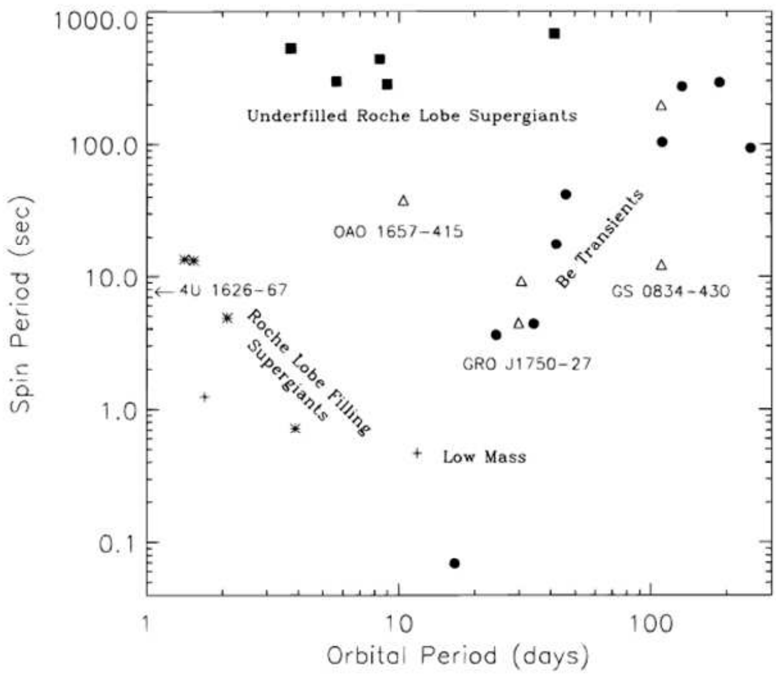

Figure 1.4: Spin period (P_{spin}) vs. orbital period (P_{orb}) plot for accretion powered pulsars, or the Corbet Diagram (Corbet 1984). *Asterisks:* SG/XBs that are Roche lobe filling. *Squares:* SG/XBs that underfill their Roche lobe. *Circles:* B*e*/XBs. *Pluses:* LMXBs. *Triangles:* binary pulsars with unknown companion type. (Bildsten et al. 1997)

SG/XBs can be further divided into two subclasses according to their dominant mass transfer mechanism: RLO or dense stellar wind, although both mechanisms can occur in some systems (Corbet 1986 and references therein). Roche Lobe filling supergiants are rather in close binaries with orbital periods less than 4 d and they have high luminosities ($L_x \geq 10^{37}$ erg s^{-1}) consistent with high accretion rates being the origin of an accretion disk. SMC X-1 (L_x ~6x10^{38} erg s^{-1}, P_{orb} ~3.9 d, P_{spin} ~0.7 s), LMC X-4 (L_x ~2x10^{38} erg s^{-1}, P_{orb} ~1.4 d, P_{spin} ~14 s) and Cen X-3 (L_x ~6x10^{37} erg s^{-1}, P_{orb} ~2.1 d, P_{spin} ~4.8 s) are good examples of RLO systems with their persistent accretion rates. The supergiants that underfill their Roche Lobes have wider orbits ($P_{orb} \geq 4$ d), therefore accretion rates and luminosities (L_x ~10^{35} - 10^{37} erg s^{-1}) are lower in accordance with the accretion of mass via dense stellar wind. Vela X-1 (L_x ~6x10^{36} erg s^{-1}, P_{orb} ~9.0 d, P_{spin} ~283 s) and 4U 1907+09 (L_x ~4x10^{36} erg s^{-1}, P_{orb} ~8.4 d, P_{spin} ~437 s) are good examples to this subclass.

As mentioned before, spin period of a pulsar is correlated with the mass accretion rate, therefore one expects to observe different periods in different subclasses of SG/XBs. The cluster of points in the upper left corner of the Corbet Diagram (see Figure 1.4) represent the wind accretion systems which have long spin periods (P_{spin} ~100 - 1000 s) due to low accretion rates. RLO systems have spin periods less than 10 s since, persistent accretion of disk matter carries steady angular momentum to the neutron star and shortens the period of rotation, i.e. spins it up (e.g. secular spin-up of Cen X-3) (Bildsten et al. 1997). The torque exerted on a wind-fed pulsar by the accreting matter is rather fluctuating with no net trend, so transitions between spin-up and spin-down episodes are observed (e.g. torque fluctuations in GX 301-2). On the Corbet Diagram (see Figure 1.4), there appears to be an anti-correlation between P_{spin} and P_{orb} of RLO systems. No correlation is seen for the wind accretors.

In this thesis, the HMXB system 4U 1907+09, which consists of an X-ray pulsar accreting material from its blue supergiant companion, is analyzed by using the observations of high energy missions, *RXTE* and *INTEGRAL*. Chapter 2 is a review on theoretical and observational aspects of accretion powered pulsars. In Chapter 3, the characteristics of 4U 1907+09 are summarized. In Chapter 4 and 5, the analysis of observations and the results of the X-ray spectral and timing studies are presented. The results of *RXTE* observations were published before in the Monthly Notices of the Royal Astronomical Society (İnam, Şahiner & Baykal et al. 2009). In this article the contributions of the author are the following; analyzing spectral data, verifying the timing results and writing the preliminary manuscript.

CHAPTER 2

ACCRETION POWERED PULSARS

2.1 Accretion Power

Considering a star of mass M and radius R, the efficiency of accretion depends on the compactness of the star: the larger the ratio M / R, the greater the efficiency. Thus, extraction of gravitational potential energy of the material which accretes onto a neutron star (R ~10 km and M ~1.4 $M_{\odot}$) is a great source of power for producing high energy radiation.

The luminosity L, of an accreting system depends on the mass accretion rate $\dot{M}$. At high luminosities, the accretion may be controlled by the radiation produced. Assuming that the accreting matter is mainly ionized hydrogen, in a steady spherically symmetric accretion, radiation exerts a force on the incident particles through Thomson scattering. If $S = L / 4\pi R^2$ is the radiant energy flux (erg s^{-1} cm^{-2}) and σ_{T} is the Thomson scattering cross-section, the force acting on the incident particles is $\sigma_{\mathrm{T}} S / c$, c being the speed of light. The radiation pushes out the particles against the gravitational force $GM\, m_{\mathrm{p}} / R^2$, where G is the gravitational constant and m_{p} is the mass of proton. When these forces become equal, the luminosity of the accreting system reaches to a maximum value, called the Eddington limit (Frank et al. 2002 and references therein);

$$
\begin{aligned}
L_{\mathrm{Edd}} &= \frac{4\pi\, GM\, m_{\mathrm{p}}\, c}{\sigma_{\mathrm{T}}} \\
&\approx 1.3\times 10^{38} \left(M / M_{\odot}\right) \quad \mathrm{erg\ s^{-1}}
\end{aligned}
\tag{2.1}
$$

At luminosities greater than the Eddington limit the radiation pressure exceeds gravitational attraction and accretion stops. This limit also implies a limit on the accretion rate $\dot{M}$. Assuming for simplicity that whole of the released gravitational potential energy of the accreted matter is converted into electromagnetic radiation; the luminosity generated by the accretion process is given by (Zel'dovich & Shakura 1969):

$$\begin{aligned} L &= \frac{GM\dot{M}}{R} \\ &\approx 1.3\times10^{37}\,\dot{M}_{17}\left(M/M_{\odot}\right)R_6^{-1}\quad \text{erg s}^{-1} \end{aligned} \tag{2.2}$$

where $\dot{M}_{17}$ is $\dot{M}$ in units 10^{17} gr s^{-1} and R_6 is R in units of 10^6 cm. Thus accretion rates of bright accretion powered pulsars with $L_x \sim 10^{37}$ erg s^{-1} are $\sim 10^{-9}$ $M_{\odot}$ yr^{-1} and the maximum limit is 10^{-10} $M_{\odot}$ yr^{-1}.

2.2 Accretion onto Neutron Stars

In order to understand the concept of accretion in the vicinity of a neutron star, one should emphasize the strong stellar magnetic field which affects the conditions. There exists a region near the neutron star where the magnetic field exerts the dominant force determining the motion of the accreting plasma. This region is called the magnetosphere. Far from the neutron star the magnetic effects are negligible and the pattern of the accretion flow is established by the angular momentum content of the matter supplied by the companion star. A stellar wind from a supergiant companion has small angular momentum, so it basically creates a radial flow. In contrast, a RLO of the companion supplies matter with large angular momentum such that the material consequently goes into orbit around the neutron star forming an accretion disk.

When magnetic stresses halt the flow at the magnetospheric boundary, an empty magnetic cavity surrounded by the plasma is created. In a steady state, the radius of the magnetosphere is determined by balancing the magnetic pressure and plasma pressure (Lamb et al. 1973):

$$\frac{B^2(r)}{4\pi} \approx \rho(r)\,v^2(r) \tag{2.3}$$

where ρ and v are the plasma density and velocity and B ($\sim\mu$ / r^3, μ being the magnetic moment) is the magnetic field strength and all are functions of radial distance r. Assuming that the velocity of the infalling plasma is equal to the free fall velocity:

$$v(r) \approx v_{\mathrm{ff}}(r) = \sqrt{\frac{2GM}{r}} \tag{2.4}$$

and that the flow is spherically symmetric, the mass accretion rate is given by:

$$\dot{M} = 4\pi\, r^2 \rho(r)\, v(r) \tag{2.5}$$

The magnetospheric radius, i.e. Alfvén radius, can be found by using Eqn.s 2.2, 2.3, 2.4 and 2.5 (Davidson & Ostriker 1973, Lamb et al. 1973):

$$\begin{aligned} r_{\mathrm{A}} &= \left(\frac{\mu^4}{2GM\dot{M}^2} \right)^{1/7} \\ &\approx 3\times10^8 \left[\frac{\mu_{30}^4}{L_{37}^2\, R_6^2} \left(\frac{M}{M_\odot} \right) \right]^{1/7} \quad \mathrm{cm} \end{aligned} \tag{2.6}$$

where μ_{30} is μ in units of 10^{30} G cm^3, L_{37} is the accretion luminosity in units of 10^{37} erg s^{-1} and R_6 is the neutron star radius in units of 10^6 cm. From above discussion it is certain that the size and structure of the magnetosphere depends on the accretion flow pattern.

The structure of the outer magnetosphere is also influenced by the rotation of the accreting material. The dynamical importance of this circulation is measured by the dimensionless angular velocity (Elsner and Lamb 1977):

$$\omega_{\mathrm{p}} = \frac{\Omega\,(r_{\mathrm{A}})}{\Omega_{\mathrm{K}}(r_{\mathrm{A}})} \tag{2.7}$$

where Ω is the angular velocity of the plasma and Ω_{K} is the angular velocity of the Keplerian orbit (see Eqn. 2.8). The rotation of the plasma is dynamically unimportant for a radial flow ($\omega_{\mathrm{p}} << 1$) and important for orbital flows ($\omega_{\mathrm{p}} \sim 1$).

2.2.1 Accretion via RLO and Disk Formation

RLO is a major process of mass transfer in accreting binaries (Frank et al. 2002 and references therein). When the companion star expands and exceeds its limiting gravitational potential, matter escapes from its outermost layers. This matter is transferred through the inner Lagrangian point, i.e. the saddle point of the Roche potential, where the 'figure of eight' shaped limiting potential crosses itself. Typical mass accretion rates are at the order of 10^{-10} - 10^{-9} $M_{\odot}$ yr^{-1}. Flow of matter is slow, but it is immediately deflected by the gravity of the neutron star causing a gain of angular momentum. First following a ballistic trajectory around the neutron star; the stream of matter collides with itself resulting in dissipation of energy via shocks and finally settles down into a circular ring of matter, the radius of which is determined by its specific angular momentum. The ring then spreads radially inward and outward due to the viscous shear stresses and an accretion disk is formed.

When the material goes into orbit, it forms a geometrically thin (vertical semi-thickness $h \ll r$), optically thick Keplerian accretion disk around the neutron star. The thermal energy density of the disk is small when compared to its mechanical energy density so that the gravitational force GM / r^2 is balanced by the centrifugal force $\Omega_{\mathrm{K}}^2\, r$. This balance condition gives the Keplerian angular velocity at any radius r from the center of neutron star:

$$\Omega_{\mathrm{K}}(r) = \sqrt{\frac{GM}{r^3}} \tag{2.8}$$

Keplerian rotation implies that material at different radii moves with different angular velocity; therefore plasma streamlines that slide past each other in the disk have chaotic thermal and turbulent motions. This concept generates viscous stresses in the disk. The most well known model of disk viscosity is called the 'α - model' (Shakura & Sunyaev 1973). In this model shear stress is related to the total pressure, $\mathcal{P}$, such that:

$$\eta\, r \left| \frac{d\,\Omega_{\mathrm{K}}}{d\,r} \right| = \alpha\, \mathcal{P} \tag{2.9}$$

where η is the effective dynamical viscosity. Theoretical works have estimated α to be in the range 0.001 - 0.1 for steady symmetric accretion disks, so the viscous stresses are negligible for such disks although it should give a sufficient contribution during instabilities.

As the temperature increases radially inward, the radial structure of an α - disk has three distinct regions: outer ($r \sim 10^{10}$ cm), middle ($r \sim 10^{8}$ cm) and inner ($r \sim 10^{6}$ cm) regions. Gas pressure dominates over radiation pressure in outer and middle regions, whereas radiation pressure is dominant in the inner region. The magnetospheres of strongly magnetized neutron stars are immersed in the gas pressure dominated regions.

Interaction between the disk and the magnetosphere is a major subject in the treatment of accretion powered pulsars. The radial inward flow of highly ionized plasma compresses the magnetic field lines; hence the magnetosphere is pinched near the disk plane and balloons outward in directions away from the disk (see Figure 2.1). The disk penetrates into the magnetic field due to several processes such as, Kelvin - Helmoltz instability, turbulent diffusion and magnetic field reconnection (Ghosh & Lamb 1979a).

First, the velocity discontinuity in the disk drives the Kelvin - Helmoltz instability which grows much faster than the slow radial inward drift of the plasma. This leads to unstable modes that disturb the inner disk and mixes the plasma with the magnetic field. Second, the vertical temperature gradient of the disk may cause large scale convection and turbulent diffusion of magnetic field into the disk then occurs since the time-scale of this diffusion is small compared to radial drift time. Third; the disk field loops reconnect within the disk, creating closed loops. These loops are distorted in a timescale less than radial drift and connect to the star. These three processes have a significant role is coupling between the disk and the neutron star (Lamb 1989, Ghosh 2007).

Once the disk and the neutron star are coupled, magnetic field lines will have their footprints on the disk moving at different angular velocities, except for the solitary ones which co-rotate with the star. The co-rotation radius, r_{co}, can be defined by using Eqn. 2.8 with $\Omega_K (r_{co}) = \Omega_s$, Ω_s being the angular velocity of the star. The

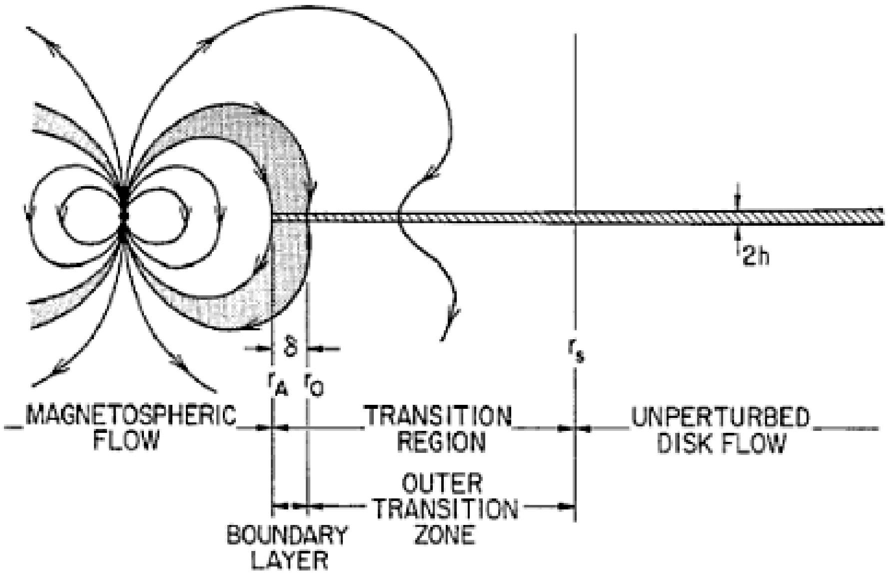

Figure 2.1: Schematics of disk accretion by a magnetic neutron star. Various regions of the flow are shown. (Ghosh & Lamb 1978)

difference | Ω_K - Ω_s | stretches the field lines in the azimuthal direction and generates an amplified toroidal field B_φ from the poloidal field B_p. The ratio of these components $\gamma_\varphi = B_\varphi / B_p$ is called the magnetic pitch, which is a measure of winding. The pitch is positive inside r_{co} whereas it is negative outside r_{co}, meaning that magnetic field affects the plasma differently (Ghosh 2007). Hence, the star can accrete if r_{co} is well outside magnetosphere. If the star rotates more rapidly than inner disk or if the mass accretion rate is not sufficient enough to squeeze the magnetosphere such that r_{co} is left inside, centrifugal barrier inhibits accretion resulting in a 'propeller' effect (Stella et al. 1986).

The disk and magnetosphere configuration described by Ghosh and Lamb (1978, 1979a) is seen in Figure 2.1. They have defined various regions that plasma enters during accretion phases. Far outside the screening radius r_s, magnetic field is screened off resulting in an unperturbed disk flow. Magnetic stresses are responsible for removal of angular momentum in the transition region between r_A and r_s. This transition region is actually divided into two parts by the boundary radius r_o where shear stresses vanish. The accreting matter is still in Keplerian rotation, i.e. not totally disturbed, in the broad outer transition region. In the narrow inner boundary region, rotation of the matter is non-Keplerian since the magnetic stresses bring matter into co-rotation with the star. The magnetospheric flow accretes onto the neutron star by moving along the field lines in the region between r_A and R. Ghosh and Lamb treated the electromagnetic boundary layer of an aligned rotator (i.e. magnetic axis is aligned with rotation axis) and found that the inner radius of the disk is $r_{in} \approx 0.5\ r_A$, where r_A is the radius of magnetosphere in the case of radial flow and r_s is in the range 10 r_{in} - 100 r_{in}.

2.2.2 Accretion via Stellar Wind

When the neutron star accretes from the dense stellar wind of its early type companion the flow is essentially radial (ω_p << 1 see Eqn. 2.7) (Shapiro & Lightman 1976, Ghosh & Lamb 1979b, Lamb 1989). The radial velocity of the accreting plasma is expected to be large at the accretion capture radius r_a (Hoyle & Lyttleton 1939):

$$\begin{aligned} r_a &\approx \frac{2GM}{v_o^2} \\ &\approx 10^{10}\left(M / M_\odot\right)\left(v_o / 10^8 \,\text{cm s}^{-1}\right)^{-2} \quad \text{cm} \end{aligned} \tag{2.10}$$

where v_o is the velocity of the wind relative to neutron star and defined as $v_o = \left(v_w^2 + v_{orb}^2\right)^{1/2}$ for a circular orbit, v_w being the wind velocity far from the neutron star (typically $v_w \sim 10^8$ cm s^{-1}) and v_{orb} being the orbital velocity of the neutron star (typically $v_{orb} \geq 10^7$ cm s^{-1}). The rate of mass accretion from the capture cross section πr_a^2 then would be:

$$\dot{M} = \rho_o v_o \pi r_a^2 \tag{2.11}$$

where ρ_o is the wind density at r_a. In fact, the accreting mass is a fraction of the stellar wind of the companion. The mass loss rate of the companion, for a spherically symmetric wind, is $\dot{M}_w = 4\pi a^2 \rho v_w$, '$a$' being the binary separation. Assuming that $v_w >> v_{orb}$, v_w is equal to the escape velocity $v_w(a) = v_{esc}(R_c) = (2GM_c / R_c)^{1/2}$ and $\rho \sim \rho_o$, the ratio can be found as:

$$\frac{\dot{M}}{-\dot{M}_{\mathrm{w}}} = \frac{1}{4}\left(\frac{M}{M_{\mathrm{c}}}\right)^2 \left(\frac{R_{\mathrm{c}}}{a}\right)^2 \sim 10^{-3} \tag{2.12}$$

where M_{c} and R_{c} are the mass and radius of the companion. Therefore, accretion from a stellar wind is an inefficient process when compared to RLO. Typical rates of mass loss by wind is rather large (10^{-6} - 10^{-5} $M_{\odot}$ yr^{-1}), such that the resulting accretion rates are sufficient enough to make the source observable (Frank et al. 2002 and references therein).

When the fast wind material is captured at r_{a}, it compresses magnetic field inward given that the field is weak there. While the plasma is decelerated by magnetic pressure, a shock wave forms near the field - plasma interface. This shock is called the magnetopause. The magnetopause traveling though the plasma heats and slows the inflow (Elsner & Lamb 1977). Eventually, compressed magnetic field becomes rigid enough to halt the inflow at the magnetospheric boundary (r_{A} defined by Eqn. 2.6).

The cooling regime of the shock-heated plasma is basically Compton cooling by inverse Compton process in which the X-ray photons cool the electrons in the accreting plasma. Consequently the ions are cooled by electrons due to collisional energy exchange. This cooled plasma should be able to enter into the magnetosphere in order to accrete onto the neutron star. The process responsible for the entry is accepted to be dominantly Rayleigh - Taylor instability (Arons & Lea 1976, Elsner & Lamb 1977). The inflowing plasma halted at the boundary becomes very dense in comparison with the magnetic cavity. Hence the boundary is unstable to small perturbations and the dense plasma descends into sparse magnetosphere.

The possibility of formation of an accretion disk with the matter captured from the stellar wind arises from the angular momentum content of the matter. Although constant density and velocity of a radial flow lead to zero angular momentum, such a stellar wind is impossible. Even in a steady wind, there are density and velocity gradients which create circulation in the flow by deforming the capture cross section. These gradients break the symmetry such that, the angular momenta of matter accreting from different parts of capture cross section are imbalanced causing a net angular momentum (Ghosh 2007 and references therein).

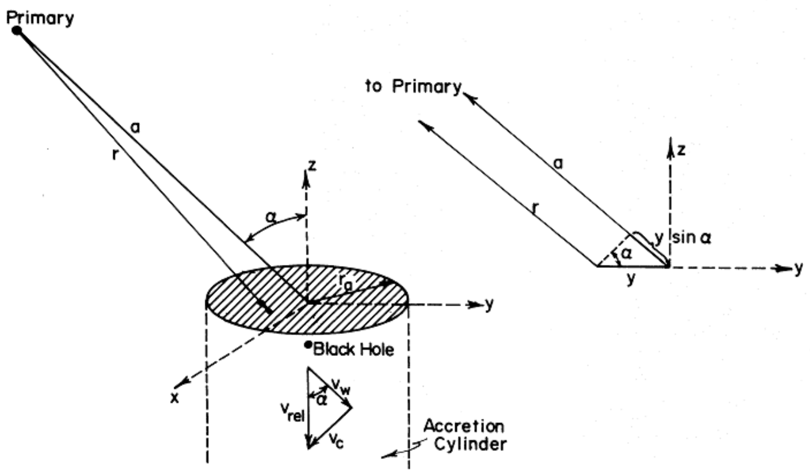

Figure 2.2: Shapiro and Lightman (1976) estimation of angular momentum content of stellar wind material.

Calculations of velocity and density gradients in a radial inflow were pioneered by Shapiro and Lightman (1976). They considered an accretion cylinder of radius r_a oriented along v_o, which is tilted at an angle $\alpha = \tan^{-1}(v_{orb} / v_w)$ with respect to the line joining the centers of two stars (see Figure 2.2). The density and velocity expressions given by this configuration were:

$$\rho(x, y) = \rho(a) - \left(\frac{d\rho}{dr}\right)_a y \sin\alpha \qquad v(x, y) = v(a) - \left(\frac{dv}{dr}\right)_a y \sin\alpha \tag{2.13}$$

and the equations given below were found for the gradients:

$$\left(\frac{d\rho}{dr}\right)_a = \frac{-2\rho(a)}{a} \qquad \left(\frac{dv}{dr}\right)_a = \frac{v_o}{a}\left(\frac{v_{orb}}{v_o}\right)^2 \tag{2.14}$$

These two gradients contribute to the net angular momentum with opposite signs, since ρ and v change in opposite sense with increasing r. The contribution of velocity gradient is smaller than the contribution of density gradient by a factor of $(v_{orb} / v_o)^2$, where $v_{orb} / v_o \leq 0.1$ for SG/XBs (Ghosh 2007).

In order to find the rate of change of the angular momentum $\dot{J}$ of the neutron star, Shapiro and Lightman (1976) evaluated the integral below (see Eqn. 2.15) over the accretion cylinder cross section, by substituting the density gradient and neglecting the velocity gradient:

$$\dot{J} = \int \rho(x,y)\, v^2(x,y)\, y\, dx\, dy$$
$$= \dot{M}\, \frac{v_{\mathrm{orb}}\, r_{\mathrm{a}}^2}{2a} \tag{2.15}$$

Consequently, the specific angular momentum per unit mass of the matter accreting from the stellar wind is found as:

$$\ell_{\mathrm{w}} = \frac{\dot{J}}{\dot{M}} \approx \frac{1}{2}\, \Omega_{\mathrm{orb}}\, r_{\mathrm{a}}^2 \tag{2.16}$$

where Ω_{orb} is the orbital angular velocity of the neutron star. If ℓ_{w} is above a critical value, formation of an accretion disk is possible. This critical value is determined by properties of such disks. The specific angular momentum of disk matter at any radius r is given by:

$$\ell_{\mathrm{K}} = \Omega_{\mathrm{K}} r^2 = \sqrt{GM\, r} \tag{2.17}$$

Evaluating Eqn. 2.17 with a typical value ℓ_{w} of a spherically symmetric wind, an outer radius for a disk can be found as $r_{\mathrm{out}} \sim 10^7$ cm. Since inner radius of a disk is given as $r_{\mathrm{A}} \sim 10^8$ cm, calculated r_{out} is less then r_{in}, which is not logical and means that an accretion disk may not exist.

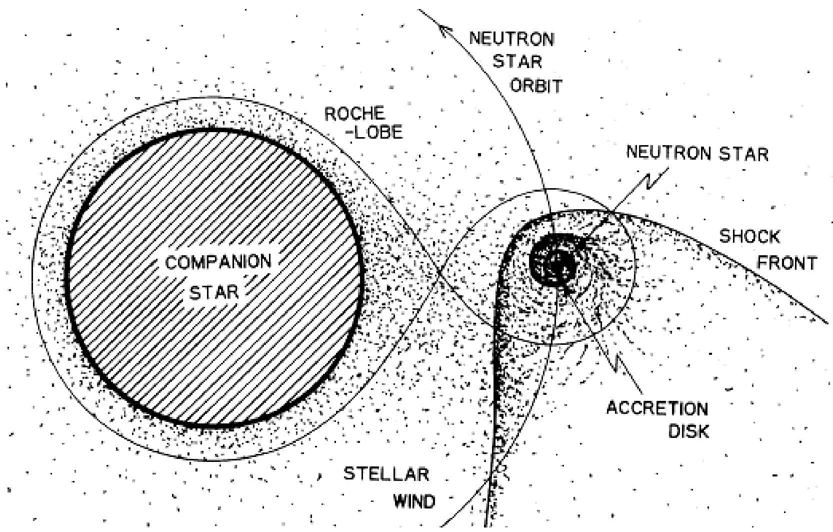

Figure 2.3: An artist conception of an accretion disk formed in the stellar wind shock (Nagase 1989).

The real case is far from symmetry in view of the fact that homogeneity of the stellar wind is disrupted by the neutron star. The interaction of the accreting plasma with the shock fronts may form a flow with large ℓ_w thereby temporary accretion disks (see Figure 2.3) (Börner et al 1987, Blondin et al. 1990). Hydrodynamic calculations of Matsuda et al. (1987) indicate that specific angular momentum of the accreting matter can be rather large with both negative and positive signs depending on the initial conditions and even for small asymmetries either prograde or retrograde accretion disks can form behind the bow shock.

2.3 Accretion Torques and Pulse Frequency Changes

Pulse timing measurements clarify that the pulse (or spin) periods of most pulsars change with time. The change is associated with the torque exerted on the star. For accretion powered pulsars, the origin of external torque is the accretion of matter with a specific angular momentum (Pringle & Rees 1972, Lamb et al. 1973). In addition there are internal torques due to coupling between the superfluid interior and the solid outer crust of the neutron star. The resulting net torque is produced by filtering of external torque fluctuations in the vicinity of the coupling between the solid crust and superfluid interior (Lamb et al. 1978a, b). The observed change in angular velocity of a star is thereby a representation of the net torque. Accretion torque plays an important role in torque fluctuations; since the accretion geometry, the amount of accreting plasma and the angular momentum of plasma are variable in a binary system. Comparison of pulse timing measurements with theories on accretion processes assist insights about the accretion characteristics and the internal properties of neutron stars. Long term trends in measurements imply the time averaged circulation of the accreting plasma, the stellar magnetic field strength and the moment of inertia of the star, while short term trends probe the stability of the accretion process and the internal dynamical properties of the star (Lamb 1989).

Most commonly, a secular decrease in the pulse period, or equivalently an increase in pulse frequency, with time is observed as the pulsar gains angular momentum from the accreting material. This trend is often called the spin-up of the pulsar, where as a decrease in the pulse frequency is called the spin-down.

2.3.1 Accretion Torque in Disk-fed Pulsars

The accretion torque exerted by a Keplerian disk flow was first considered by Pringle and Rees (1972), Davidson and Ostriker (1973), Lamb et al. (1973). The specific angular momentum of the matter at the inner edge of the disk can be defined by evaluating Eqn. 2.17 as $\ell_{\mathrm{in}} = \sqrt{GM\, r_{\mathrm{in}}}$. If it is assumed that ℓ_{in} is transferred to the star, the accretion torque is then:

$$N_{\mathrm{o}} = \dot{M}\, \ell_{\mathrm{in}} \tag{2.18}$$

Here, only the contribution of the material stress is considered for simplicity. Magnetic and viscous stresses should make important contributions to the torque in more realistic cases.

One needs to examine the conservation of angular momentum to understand the rotational response of the neutron star to the accretion torque. The angular momentum of a star can be written as $J_{\mathrm{s}} = I_{\mathrm{s}}\, \Omega_{\mathrm{s},}$ where I_{s} is the moment of inertia of the star. Conserving angular momentum, the rate of change of angular momentum of the star is equal to the torque expressed in Eqn. 2.18:

$$\dot{J}_{\mathrm{s}} = \frac{d}{dt}\left(I_{\mathrm{s}}\, \Omega_{\mathrm{s}}\right) = \dot{M}\, \ell_{\mathrm{in}} \tag{2.19}$$

The rate of change of angular velocity of the star can be derived from Eqn. 2.19 as (Ghosh et al. 1977):

$$\dot{\Omega}_{\mathrm{s}} = \frac{\dot{M}}{M}\left(\frac{\ell_{\mathrm{in}}}{\ell_{\mathrm{s}}} - \frac{d \ln I_{\mathrm{s}}}{d \ln M}\right)\Omega_{\mathrm{s}} \tag{2.20}$$

where $\ell_{\mathrm{s}} = J_{\mathrm{s}}\, M = \Omega_{\mathrm{s}}\, R_{\mathrm{g}}^2$ is the specific angular momentum of the star, $R_{\mathrm{g}} = \sqrt{I_{\mathrm{s}} / M}$ being the radius of gyration. Thus, the response of the star can be characterized by the term inside parenthesis. The $\ell_{\mathrm{in}} / \ell_{\mathrm{s}}$ term tends to spin-up the star whereas $\left(d \ln I_{\mathrm{s}} / d \ln M\right)$, i.e. logarithmic increase in the moment of inertia per unit increase in stellar mass due to accretion, tends to spin-down the star. Setting a dimensionless parameter:

$$\varsigma = \frac{\ell_{\rm in}}{\ell_{\rm s}}\left(\frac{d\ln M}{d\ln I_{\rm s}}\right)$$

$$= \frac{\ell_{\rm in}}{\Omega_{\rm s} R_{\rm g}^2}\left(\frac{d\ln M}{d\ln I_{\rm s}}\right) = \frac{\ell_{\rm in}}{\Omega_{\rm s}}\left(\frac{dM}{dI_{\rm s}}\right) \quad (2.21)$$

Eqn. 2.20 becomes:

$$\dot{\Omega}_{\rm s} = (\varsigma - 1)\frac{\dot{M}}{M}\left(\frac{d\ln I_{\rm s}}{d\ln M}\right)\Omega_{\rm s} \quad (2.22)$$

Accordingly, for $\zeta > 1$ the star spins up and for $\zeta < 1$ it spins down.

Derivation of the rate of change of the rotational energy of the star, with a similar method, reveals that:

$$\dot{E}_{\rm rot} = \frac{d}{dt}\left(\frac{1}{2} I_{\rm s}\,\Omega_{\rm s}^2\right)$$

$$= 2\left(\varsigma - \frac{1}{2}\right)\frac{\dot{M}}{M}\left(\frac{d\ln I_{\rm s}}{d\ln M}\right)E_{\rm rot} \quad (2.23)$$

the star loses rotational energy for $\zeta < ½$ and gains rotational energy for $\zeta > ½$. So, for $½ < \zeta < 1$, the star spins down although it gains rotational energy. The logarithmic derivative $(d\ln I_{\rm s} / d\ln M)$ is generally ~1 for intermediate mass neutron stars. Assuming $R_{\rm g} \approx R$ and using Eqn. 2.17, Eqn. 2.21 reduces to:

$$\varsigma \approx \frac{\ell_{\rm in}}{\ell_{\rm s}} = \frac{\Omega_{\rm K}\,(r_{\rm in})}{\Omega_{\rm s}}\left(\frac{r_{\rm in}}{R}\right)^2 \quad (2.24)$$

Since $r_{\rm in} >> R$, even if $\Omega_{\rm K} << \Omega_{\rm s}$ the dimensionless parameter is much bigger than 1 which means that, spin-up term dominates over spin-down term for the simple case considered.

In general, the rate of change of the angular momentum $\dot{J}_{\rm s}$ of a neutron star due to accretion torque, N, is given by the integral over any surface S that encloses the star:

$$\dot{J}_{\mathrm{s}} = N = -\int_S (\vec{r} \times \vec{\Pi}) \cdot \hat{n}\, dS \tag{2.25}$$

where $\vec{\Pi}$ is the momentum flux density tensor, $\hat{n}$ is a unit vector normal to the surface directed outward and $\vec{r}$ is the position vector originating from the center of the star. For a time independent, axisymmetric, steady accretion flow Eqn. 2.25 is calculated to be (Ghosh et al. 1977, Ghosh & Lamb 1979a, b):

$$N = \int_S \left(-\rho \varpi^2\, \Omega \vec{v}_{\mathrm{p}} + \varpi\, \frac{B_{\varphi} \vec{B}_{\mathrm{p}}}{4\pi} + \eta\, \varpi^2\, \nabla\Omega \right) \cdot \hat{n}\, dS \tag{2.26}$$

where ϖ is the cylindrical radius, v_{p} and Ω are poloidal and angular velocity of the plasma. The three terms inside the parenthesis in Eqn. 2.26 represent the contributions of material, magnetic and viscous stresses respectively. The relative sizes of these three contributions depend on the surface used to evaluate the integral.

Ghosh and Lamb (1979b) defined three surfaces to evaluate Eqn. 2.26 (see Figure 2.4); S_1 close to the star just at the magnetospheric boundary, S_2 at the outer transition zone and S_3 at far outside. The total torque N is the sum of torques exerted from S_1, S_2 and S_3: $N = N_1 + N_2 + N_3$. Viscous stresses are negligible on S_1 and magnetic stresses have no component perpendicular to S_1, hence N_{o} given by Eqn. 2.18 is a good approximation for the torque contribution N_1:

$$\begin{aligned} N_1 &= \rho\, v_{\mathrm{r}}\, r_{\mathrm{in}}^2\, \Omega_{\mathrm{K}}(r_{\mathrm{in}}) \times 2\pi\, r_{\mathrm{in}} \times 2h \\ &= \dot{M} \sqrt{GM\, r_{\mathrm{in}}} = N_{\mathrm{o}} \end{aligned} \tag{2.27}$$

In contrast; viscous stresses have no component perpendicular to S_2 and material stresses are negligible since no matter crosses S_2, so the contribution N_2 is given by the magnetic stresses $N_2 \sim N_{\mathrm{mgn}}$:

$$\begin{aligned} N_2 = N_{\mathrm{mgn}} &= \int_{S_2} r\, \frac{B_{\mathrm{z}}\, B_{\varphi}}{4\pi}\, dS \\ &= \int_{r_{\mathrm{in}}}^{r_{\mathrm{s}}} \gamma_{\varphi} B_{\mathrm{z}}^2\, r^2 dr \end{aligned} \tag{2.28}$$

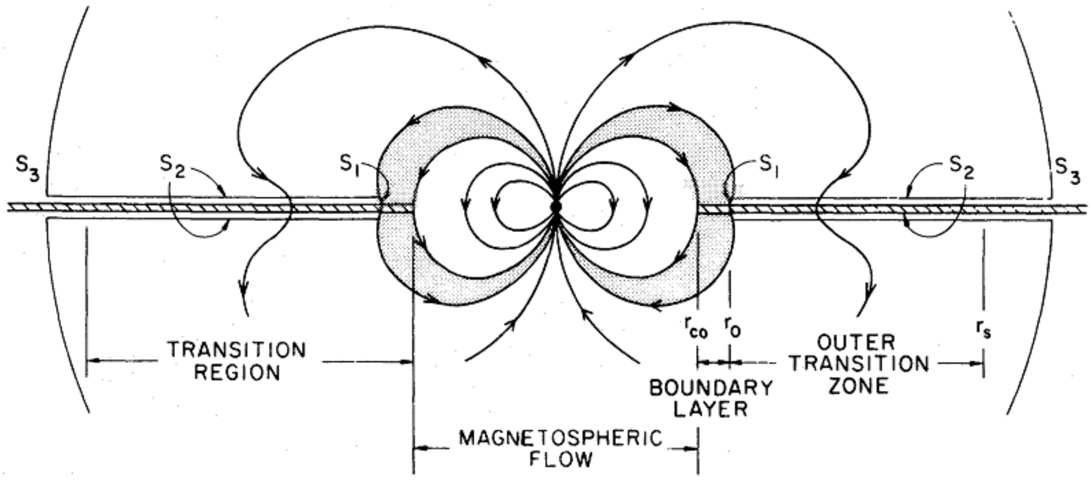

Figure 2.4: Side view of accretion flow and the surfaces used to evaluate Eqn. 2.20 (Ghosh & Lamb 1979b). S_1: cylindrical surface of radius r_{in} and height $2h$. S_2: Two plane surfaces just above and below the disk. S_3: two hemispherical surfaces at infinity.

where the magnetic pitch γ_φ defined before is used. The contribution N_3 is totally negligible because the magnetic stress falls off much more rapidly than r^3 on S_3.

Finally, the total torque can be written as:

$$N = N_{\mathrm{o}} + N_{\mathrm{mgn}} = n(\omega_{\mathrm{s}})\,N_{\mathrm{o}} \tag{2.29}$$

where n (ω_{s}) is a dimensionless function which measures the variation of the torque and it depends on the fastness parameter ω_{s}. The dimensionless torque can be approximated as (Ghosh & Lamb 1991):

$$n(\omega_{\mathrm{s}}) \approx 1.4\left(\frac{1-\omega_{\mathrm{s}}/\omega_{\mathrm{c}}}{1-\omega_{\mathrm{s}}}\right) \tag{2.30}$$

The fastness parameter is a ratio of the angular velocity of the star, Ω_{s}, to the Keplerian angular velocity at inner disk:

$$\begin{aligned} \omega_{\mathrm{s}} &= \frac{\Omega_{\mathrm{s}}}{\Omega_{\mathrm{K}}(r_{\mathrm{in}})} \\ &\approx 1.2\, P_{\mathrm{spin}}^{-1}\, \dot{M}_{17}^{-3/7}\, \mu_{30}^{6/7}\left(\frac{M}{M_{\odot}}\right)^{-5/7} \end{aligned} \tag{2.31}$$

Dependence of ω_s on the magnetic field strength and mass accretion rate derive important implications. First, when the magnetic field is weaker ω_s gets smaller and n (ω_s) gets larger causing a spin-up. Second, if the mass accretion rate is smaller ω_s gets larger and n (ω_s) gets smaller causing a spin-down.

In Eqn. 2.30, ω_c is a critical value of fastness parameter for a radius at which the accretion torque is expected to vanish. Lamb (1989) determined that ω_c is between ~0.35 - 0.85. For slowly rotating neutron stars ($\omega_s << 1$), n (ω_s) takes its maximum value ~1.4, so that N ~1.4 N_o ~N_o is the maximum spin-up torque. For faster rotators, n (ω_s) decreases with increasing ω_s and vanishes at the critical value ω_c. For $\omega_s > \omega_c$, n (ω_s) becomes negative resulting in a spin-down torque. Above a maximum value ω_{max} ~1, steady accretion is not possible.

The nature of the net torque exerted on the star can be understood better when the torques N_o and N_{mgn} are separately examined (see Eqn. 2.29). N_o is the contribution of material stresses and it can only carry a positive angular momentum which causes a spin-up. The sign of N_{mgn} (see Eqn.2.28) is determined by the magnetic pitch, so the behavior of the function n (ω_s) in fact depends on the pitch (Ghosh 2007). If $\Omega_K > \Omega_s$ the pitch is forward while it is backward for $\Omega_K < \Omega_s$. Therefore N_{mgn} changes sign at the co-rotation radius causing spin-up for $r_{in} < r < r_{co}$ and spin-down for $r_{co} < r < r_s$ (see Figure 2.4). For a slow rotator ($\omega_s << \omega_c$) r_{co} exceeds r_s (since $r_{co} \propto \Omega_s^{-2/3}$) and N_{mgn} is entirely positive. As the star rotates faster, r_{co} moves inside r_s and N_{mgn} becomes smaller and then negative. At the point of critical fastness ω_c, N_{mgn} cancels N_o and the net torque vanishes. For the case of fast rotators ($\omega_s > \omega_c$, r_{co} ~r_{in}) negative N_{mgn} dominates over N_o, so the net torque results a spin-down.

Therefore, in the pioneering model of Ghosh and Lamb (1979b) the fastness, ω_s, of the neutron star determines whether it will spin-up or spin-down. For the case of a slowly rotating neutron star in the same direction as the accretion disk, the transfer of positive angular momentum spins up the neutron star. On the other hand, if the star rotates in the opposite direction of the accretion disk, it spins down. If the neutron star rotates rapidly, it spins down for either direction. Ghosh and Lamb have also found a scaling for the rate of change of the pulse period:

$$-\dot{P} = n(\omega_s) f_N(\mu, M) \left(PL^{3/7}\right)^2$$
$$-\dot{P} = f_{GL}(\mu, M, PL^{3/7}) \tag{2.32}$$

where f_N is a function that depends on μ and M and noting that the fastness shows a scaling $f_\omega(\mu, M)/(PL^{3/7})$ (see Eqn. 2.31), consequently the scaling of $\dot{P}$ is given by a function f_{GL} (Ghosh 2007). Since L is correlated with $\dot{M}$ (see Eqn. 2.2) an increase in $\dot{M}$ results in a decrease in fastness and the star experiences a strong spin-up torque. When $\dot{M}$ deceases, ω_s increases, spin-up torque falls off and eventually spin-down torque rises up. Observations of Be/XBs during their outbursts show rapid spin-up episodes, which support the f_{GL} scaling.

2.3.2 Accretion Torque in Wind-fed Pulsars

As discussed in section 2.2.2 matter accreting from a stellar wind may have large specific angular momentum due to velocity and density gradients. Given that the radial velocity of the accreting plasma is high, the plasma pressure at the capture radius r_a would be large. Since the magnetosphere of the neutron star lies well below r_a magnetic stresses can not dominate, so the resulting torque exerted on the neutron star is dominated by material stresses (Ghosh & Lamb 1979b, Lamb 1989, Ghosh 2007). Analogous to Eqn. 2.18 the torque expression is:

$$N = \dot{M}\,\ell_w \tag{2.33}$$

where $\dot{M}$ and ℓ_w are defined through Eqn. 2.11 and Eqn. 2.16 respectively. Using Eqn.s 2.10, 2.11 and 2.16, the torque exerted by the matter accreting from the stellar wind becomes (Ghosh & Lamb 1979b):

$$N \approx \frac{\pi^2 \rho_o (2GM)^4}{P_{orb}\, v_o^7} \tag{2.34}$$

More detailed calculations of the angular momentum capture rate when there are velocity and density gradients are done by Wang (1981), Anzer et al. (1987) and

Ho (1988), in order to explain torque reversals in wind-fed systems. The specific angular momentum is revised to be:

$$\ell_{\mathrm{w}} = \frac{1}{2}\eta_{\mathrm{w}}\ \Omega_{\mathrm{orb}}\ r_{\mathrm{a}}^{2} \tag{2.35}$$

where η_{w} is a dimensionless parameter, at the order of unity for uniform radial velocity. In the presence of both radial and azimuthal velocity and density gradients, η_{w} can be negative implying a spin-down torque.

The stellar winds of early type stars are known to vary irregularly on any time-scale from minutes to years (Nagase 1989). These variations may prevent steady flows and create unstable circulations in the flow, which reverses direction quasi-periodically with associated outbursts of mass inflow to the neutron star. This is the well known flip-flop behavior of wind fed HMXBs (e.g. Vela X-1, GX 301-2) in which spin-up and spin-down transitions are observed in short time-scales.

2.3.3. Recent Studies on Torque Reversal

Former pulse timing measurements of accretion powered pulsars with satellites such as *Einstein, Hakucho, Tenma, EXOSAT, Ginga* etc. only revealed long term averages of accretion torques, since pointed observations were rarely done. Ghosh & Lamb model of accretion torques, described in previous sections above (see Eqn. 2.29), was mostly satisfactory to explain these secular period changes (Nagase 1989). However, subsequent continuous observations with *BATSE* instrument on board *Compton Gamma Ray Observatory* (*CGRO*, launched in 1991) denoted that the real picture is more complex. The long term monitoring capability of *BATSE* enlightened the short term effects of accretion torque. *BATSE* data of some disk-fed pulsars displayed bimodal behavior with sudden transitions between spin-up and spin-down (i.e. torque reversals) on time-scales less than 10 d, which is hard to explain with simple models (Bildsten et al. 1997, Nelson et al. 1997).

The spin behavior of Cen X-3 is a prominent example of bimodal torques. *BATSE* observations have shown that Cen X-3 exhibits 10 - 100 d steady spin-up and spin-down episodes with comparable magnitude but opposite sign (Bildsten et al.

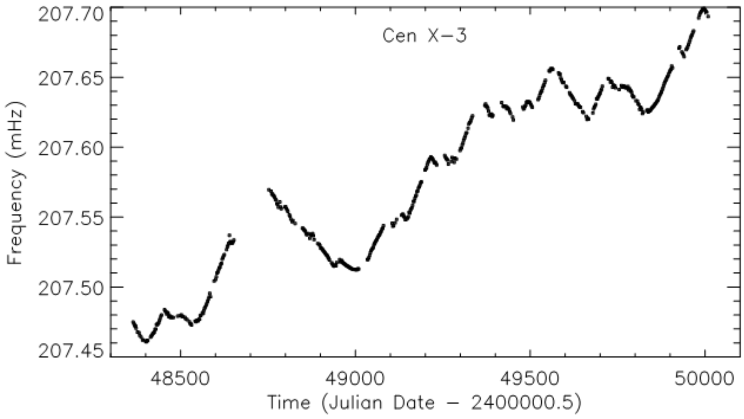

Figure 2.5: Pulse timing measurements of Cen X-3 from BATSE observations (Bildsten et al. 1997).

1997, Nelson et al. 1997) (see Figure 2.5). Accretion disk theory can only explain this behavior with repeated step function-like changes in mass accretion rate which is unlikely in view of the fact that no significant luminosity change is observed. Nelson et al. (1997), on the basis of a previous suggestion (Makishima et al. 1988), have suggested that a disk reversing in the sense of rotation may be the cause of transitions. Even though transient formation of retrograde accretion disks is known to occur in numerical simulations of wind fed systems, the situation is implausible for RLO systems where matter enters the disk in prograde orbit. The torque reversals of the wind-fed system GX 1+4 has become a regular example of retrograde disk formation since Chakrabarty et al. (1997a) found that GX 1+4 spins down more rapidly during short term flares observed with *BATSE*. The anti-correlation between the torque and luminosity is not compatible with the standard theory, in which the spin-down torque reduces during high accretion phases. This anti-correlation is possible if the accreted material carries negative angular momentum indicating a circulation in the opposite direction to the star (Murray et al. 1999).

Van Kerkwijk et al. (1998) suggested a modification of the Nelson et al. (1997) picture, such that only the inner part of the accretion disk changes its direction of rotation. The phenomenon depends on the idea that the disk is unstable to warping when there is strong irradiation by the neutron star (Pringle 1996). The behavior of irradiated disks in binary systems has been studied in detail by Wijers and Pringle

(1999). The numerical simulations have shown that the inner disk may sometimes so warped that it is tilted more than 90 degrees, meaning a rotation in the opposite direction. The formation of this retrograde inner disk is the source of negative torque causing a spin-down (van Kerkwijk et al. 1998). Generally if the spin-down is due to this phenomenon, as the inner disk precesses more disk surface would be exposed to the neutron star, hence one would expect increased scattering, stronger fluorescence lines and absorption edges. One problem of this model is that, the time-scales of flipped over inner disks is uncertain. Inclination being stable with no restoring mechanism for the original prograde configuration is in contradiction with the observed spin-up, spin-down episodes of roughly equal times.

An alternative model for torque reversals have been suggested by Yi et al. (1997). In this model, as soon as the mass accretion rate becomes smaller than a critical value (10^{15} - 10^{16} g s^{-1}), the inner disk may make a transition from a former Keplerian flow to a sub-Keplerian advection dominated accretion flow (ADAF). The new angular velocity of the flow is written as:

$$\Omega'(r) = A\,\Omega_{\mathrm{K}}(r) \tag{2.36}$$

where $A < 1$ is a constant. A sudden transition to Ω' reduces the co-rotation radius such that:

$$r'_{\mathrm{co}} = A^{2/3}\, r_{\mathrm{co}} \tag{2.37}$$

Consequent increase in the fastness parameter, $\omega'_{\mathrm{s}} = \omega_{\mathrm{s}} / A$, implies that a transition from spin-up to spin-down is possible at low accretion rates, however this is not maintained by observations. This model also requires a gradual modulation of accretion rate on a time-scale ranging from a year to a few decades. A supportive example for this model is 4U 1626-67, which have shown two decades of smooth spin-up before reversing to spin-down in 1991 (Chakrabarty et al. 1997b). Some significant spectral changes related to the torque reversal of 4U 1626-67 is reported (Chakrabarty et al. 1997b) which can be associated with transition to ADAF (Yi & Wheeler 1998).

Another mechanism that can explain a torque reversal is proposed to be bimodal magnetic torques within the presence of intrinsic magnetic field in the accretion disk (Torkelsson 1998). If the orientation of the disk field is assumed to be independent of angular velocities of the disk and the star, the direction of the magnetic torque is arbitrary. Lovelace et al. (1999) also proposed a magnetic model for propeller driven outflows, in which the inner radius of the disk depends on the angular velocity of the star. They have shown that, for a given Ω_s, there are two solutions of r_o with one bigger than r_{co} and the other smaller than r_{co}, such that propeller becomes off and on, respectively. Consequently, chaotic transitions between spin-up and spin-down are triggered with the ratio of opposite torques at the order of unity, which agrees with observations of Cen X-3.

Locsei and Melatos (2004) have presented a time dependent model of the interaction between the disk and the magnetosphere, in which structure of the magnetosphere is determined by balancing outward diffusion and inward advection of the stellar magnetic field at the inner edge of the disc. In this model the system possesses two stable equilibria for certain conditions, corresponding to spin-up and spin-down episodes. The nature of the equilibria is managed by the ratio of the viscous diffusion rate to the magnetic diffusion rate (i.e. Magnetic Prandtl number, P_m) and the ratio of the co-rotation radius to the Alfvén radius, ξ. Locsei and Melatos have shown that, for $\xi \geq P_m^{0.3}$ the system has two stable torque states with opposite signs and in the absence of extraneous perturbations; an initial spin-up vanishes as ξ decreases causing a transition to spin-down. This situation is eventually followed by an evolution toward a state of zero torque, therefore the model can not exhibit repeated torque reversals.

A recent model, based on the earlier models considering only material torque, makes use of the fact that the magnetic axis is tilted with respect to the axis of rotation of the neutron star (Perna et al. 2006). If the accretion disk is assumed to be formed in the equatorial plane of the neutron star, the magnetic field strength depends on the azimuthal angle; therefore an asymmetric magnetospheric boundary is produced. Variable boundary radius can lead to different regions where $r_a < r_{co}$ in some and $r_a > r_{co}$ in others such that; the propeller effect is locally at work, while accretion from other regions is possible. Perna et al. (2006) have shown that, for magnetic axis inclinations greater than a critical value (~25° - 45°), cyclic torque reversal episodes may be generated without a significant change in the mass accretion rate. The time-scale of cyclic episodes in fact depends on the accretion rate, magnetic field strength and axis inclination and the degree of elasticity regulating the interaction of the disk with the magnetosphere, but no external perturbations are required to trigger the torque reversals. The main drawback of this model is that the disk is assumed to be flat in the equatorial plane of the neutron star, though it is expected to be warped and precessing in more realistic disk models. This model also neglects other possible sources of torque, such as magnetic and viscous stresses.

2.4 Pulse Profiles

The basic geometry of a pulsar's pulse profile depends on three distinct directions, the direction of the rotation axis and the magnetic axis of the pulsar and the direction the line of sight of the observer (Wang & Welter 1981, White et al 1983, Nagase 1989, Ghosh 2007). The conditions become more complex when the physics of the emission process and the transfer of the emitted radiation through magnetized plasma are considered. Since the surrounding plasma is highly anisotropic depending on the energy of the emitted photons, the pulse profile depends on the energy and the X-ray luminosity. This phenomenon is supported by the observations such that the pulse shapes and amplitudes of pulsars show dramatic differences. Nagase (1989) has grouped the pulse profiles of accretion powered pulsars into several patterns, the examples of which can be found in Fig. 2.6:

a) Single peak sinusoidal profiles which have little energy dependence (e.g. X Per, GX 304-1)
b) Double peak sinusoidal profiles with different amplitudes which have little energy dependence (e.g. SMC X-1, GX 301-2, 4U 1538-52),
c) Asymmetric single peak profiles with some additional features which have little energy dependence (e.g. Cen X-3, GX 1+4)
d) Single sinusoidal peak profiles at high and low energies, which turn into a close double peak profile at intermediate energies (e.g. Her X-1, 4U 1626-67)
e) Double peak sinusoidal profiles at high energy and complex multiple peak structure at low energy (e.g. Vela X-1, A 0535+26)

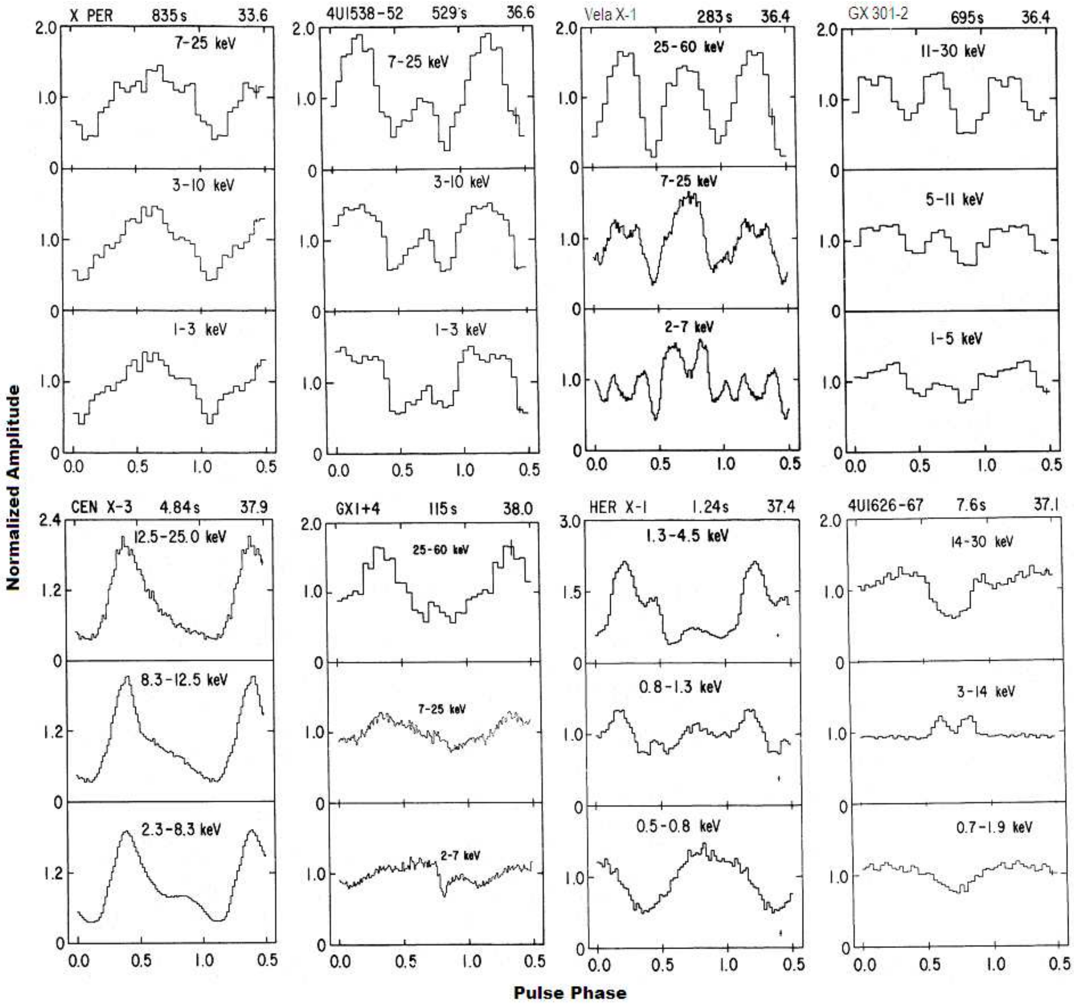

Figure 2.6: Energy resolved folded pulse profiles of 8 accretion powered pulsars. Source names, pulse periods and log of luminosities are given at the top of each panel. (White et al. 1983)

Let the angles of magnetic axis and line of sight with respect to rotation axis be α and β. If $\alpha + \beta < \pi / 2$ one magnetic pole is visible and the pulse profile has single peak. If $\alpha + \beta > \pi / 2$ both poles are visible and the pulse profile has double peaks (Wang & Welter 1981). Asymmetric pulse profiles are produced by two polar cap emission regions with different sizes or in some cases by an offset of the magnetic axis (Parmar et al. 1989, Leahy 1991).

The shape of the beaming reflects the fundamental properties of the accretion process. The beam shape of a pulse is described as a pencil beam when most of the radiation is emitted along the magnetic axis, whereas it is described as a fan beam when it is emitted perpendicular (Wang & Welter 1981). The triggering mechanism of perpendicular emission is a radiative shock which forms if the luminosity of the emission is high. The limiting luminosity can be found by solving one dimensional hydrodynamic and radiative diffusion equations (Basko and Sunyaev 1976, White et al. 1983):

$$L_{\mathrm{lim}} \approx 5\times10^{36} \frac{\sigma_{\mathrm{T}}}{\sigma_{\mathrm{s}}} r_5 \, R_6^{-1} \left(\frac{M}{1.4 M_{\odot}} \right) \quad \mathrm{erg\ s^{-1}} \tag{2.38}$$

where r_5 is the radius of the accretion column in units of 10^5 cm, R_6 is the radius of the neutron star in units of 10^6 cm and σ_{s} is the effective scattering cross section of photons relative the Thomson value σ_{T}. L_{lim} distinguishes two zones in the accretion column; the free fall zone and the shock wave zone.

At luminosities less than L_{lim} the outgoing radiation does not shock the inflowing material and the material loses its energy via Coulomb interactions in the outer layers of the neutron star (Meszaros et al. 1980). The emission region is a thin slab, the free fall zone, and reduced scattering along the magnetic field lines produces a pencil beam (White et al. 1995 and references therein). In this case, pulse profiles are much simpler with little energy dependence. Since low luminosity is a fact for low accretion rate, typically, spherical stellar wind accretors like widely separated B*e*/XBs tend to have lower amplitudes and less structured pulsations (e.g. X Per in Figure 2.6).

At luminosities more than L_{lim} the inflowing material loses its energy in the radiative shock and the emission is a fan beam. The scattering cross section of photons depends on the propagation direction of the emission at low energies; on the other hand it is independent for higher energies (Nagel 1981a, b). Thus, the resulting pulse profiles are energy dependent with complex structures at low energies. 4U 1626-67 and Her X-1 (see Figure 2.6) are good examples with pulse phase reversals between different energy bands, which in turn can be explained by a change in the beam shape from pencil to fan. The complex pulse profile of Vela X-1 at low energies can also be explained with the fan beam model.

2.5 Quasi-Periodic Oscillations

Quasi-periodic oscillations (QPOs) are rather aperiodic variabilities in the X-ray intensity. QPOs can be distinguished as broad peaks in the power spectrum, in contrast to very sharp peaks due to the pulse characteristics of accretion powered pulsars. One can calculate the quality factor, Q, of a peak in order to determine a QPO, $Q = \nu / \lambda$ where ν and λ are the centroid frequency and the width of the peak. A peak with $Q \geq 2$ is defined as a QPO.

The QPO phenomenon occurs in most of the accreting compact objects and is associated with the accretion flows. Models proposed to explain this phenomenon can be basically categorized into three:

a) Models involving accretion flow instabilities; are mostly applied to luminous objects close to Eddington limit (Lamb 1988, Fortner et al. 1989)

b) The Keplerian frequency model; defines QPOs as frequencies of the inner edge of a Keplerian disk, $\nu_{\text{QPO}} = \nu_{\text{K}}$ (van der Klis et al. 1987)

c) The beat frequency model; interprets QPOs as the beat frequency between the neutron star spin frequency and the Keplerian frequency at the inner edge of the accretion disk, $\nu_{\text{QPO}} = \nu_{\text{K}} - \nu_{\text{s}}$ (Alpar & Shaham 1985)

In fact the properties of QPOs in LMXBs are studied well (for recent review see; van der Klis 2006), this subject is beyond the scope of this work. Detection of QPOs in accretion powered pulsars in HMXBs is summarized here.

Low frequency QPOs were first detected in the B*e*/XB EXO 2030+375 (Angelini et al. 1989) and the number of HMXBs that show QPOs has grown to be around 10 soon afterwards. The frequencies of QPOs in these systems are in the range 10 - 400 mHz (Ghosh 2007). QPOs in accretion powered pulsars are expected to be probes to processes in the inner accretion disks and therefore the properties of accretion torques exerted on the neutron star (Ghosh 1998). If one makes use of the beat frequency model, the fastness parameter ω_s of the pulsar could be calculable as:

$$\omega_s = \frac{\nu_s}{\nu_s + \nu_{QPO}} \tag{2.39}$$

which is of central importance in accretion torque theory of Ghosh and Lamb (1977, 1979a, b). Since the inner radius of an accretion disk scales with the mass accretion rate, so with the luminosity, one should expect an increase in ν_{QPO} with increasing luminosity. Observational evidence only in two sources, EXO 2030+375 and A 0535+26 (Finger et al. 1996) made this argument untenable. However, for pulsars that ν_{QPO} does not change significantly (such as 4U 1626-67, Kommers et al. 1998; Cen X-3, Finger 1999) detection of asymmetric sidebands, the lower sidebands being stronger than the higher ones, suggests that the orbital frequency of the disk contributes to the QPO signal.

High frequency QPOs are reported by Jernigan et al. (2000) for Cen X-3 at frequencies ~300 and ~760 Hz. This is the only example of strongly magnetized neutron stars that have millisecond oscillations nevertheless, the origin of these oscillations remains to be understood. Jernigan et al. (2000) interpreted these QPOs in terms of a model called photon bubble, where photon bubbles rise up by buoyancy through the accreted material and produce a flash of radiation when they burst at the top (Klein et al. 1996).

2.6 Energy Spectra

The character of emission from accretion powered pulsars is basically thermal, although the strong magnetic field has complicating effects on the propagation of radiation. The process that converts the energy into radiation is essentially blackbody emission from the heated stellar surface and the hot ionized plasma. By Stefan's law;

$$L = \sigma_{\text{SB}}\ A_{\text{cap}}\ T_{\text{b}}^{4} \tag{2.40}$$

where σ_{SB} is the Stefan - Boltzmann constant, A_{cap} is the polar cap area and T_{b} is the blackbody temperature. For a typical pulsar with L ~10^{36} erg s^{-1} and A_{cap} ~1 km^2, T_{b} can be found as ~10^7 K which corresponds to a peak at photon energies ~3 keV. X-ray spectra of accretion powered pulsars peak at a similar value, despite the fact that they show harder spectra with more complex emission mechanisms.

2.6.1 Continuum Emission

The energy spectra of X-ray pulsars are generally fitted by a functional form (White et al. 1983, Coburn et al. 2002):

$$N(E) = N_{\text{o}}\ E^{-\Gamma} \times \begin{cases} 1 \quad , & E \le E_{\text{cut}} \\ \\ e^{(E_{\text{cut}} - E)/E_{\text{f}}} \quad , & E \ge E_{\text{cut}} \end{cases} \tag{2.41}$$

characterized by a power law $E^{-\Gamma}$ with the photon index Γ in the range 0 - 1 up to a high energy cutoff E_{cut}. Above this cutoff energy the spectra decay more steeply by the exponential roll-off, where the e-folding energy is given by E_{f}. Typical values for

Table 2.1: Spectral parameters of accretion powered pulsars fitted by Eqn. 2.41. (Coburn et al. 2002)

System	Γ	E_{cut} (keV)	E_{f} (keV)
Her X-1	0.93	22.0	10.8
4U 0115+63	0.26	10.0	9.3
Cen X-3	1.24	21.3	6.67
4U 1626-67	0.88	6.8	38.8
XTE J1946+274	1.14	22.0	8.3
Vela X-1	0.00	17.9	8.8
4U 1907+09	1.236	13.5	9.8
4U 1538-52	1.161	13.6	11.9
GX 301-2	-0.02	17.3	6.7
4U 0532+309	1.82	57	50

E_{cut} and E_f both are in the range 10 - 20 keV (see Table 2.1). N_o is a normalization of photons per keV cm^2 s at 1 keV.

Several X-ray pulsars show an excess at low energies in the range ~0.1 - 4 keV (e.g. Her X-1 with kT ~0.11 keV (McCray et al 1982)). So called soft excess can be fitted with blackbody emission models and its origins have been discussed to be the hot material of polar caps or accretion disks and in some cases scattering of hard X-ray emission by the stellar wind (Baykal 2005).

2.6.2 Absorption Properties

The photoelectric absorption of soft X-rays is expected due to cool homogeneous circumstellar matter in the line of sight between the observer and the source of emission (Nagase 1989):

$$M(E) = \exp\left(n_{\mathrm{H}}\ \sigma(E)\right) \tag{2.42}$$

where n_{H} is the hydrogen absorption column density (in units of 10^{22} atoms cm^{-2}) and σ (E) is the photoelectric cross-section. In some accretion powered pulsars (e.g. Vela X-1 (Haberl & White 1990), 4U 1907+09 (Roberts et al. 2001)), n_{H} is highly variable over the binary orbit and can range up to ~10^{23} - 10^{24} atoms cm^{-2} (see Figure 2.7). This variation is a probe to the density distribution of the accreting matter and outer atmosphere of the companion. The observed increase in absorption at periastron passage or eclipse ingress may be due to a gas stream from the companion trailing behind the neutron star (Haberl et al. 1989). An anti-correlation between the soft excess and the X-ray luminosity of the source suggests an increase in ionization with increasing luminosity, which forms a photo-ionized region around the X-ray source that causes reduction of opacity at low energies.

2.6.3 Fluorescent Iron Lines

Another feature in spectra of accretion powered pulsars is an emission line around energy ~6.4 keV corresponding to iron (Fe) Kα line. A Kα X-ray line results from the radiative transition of an L-shell electron to the K-shell (2p to 1s) of a metal

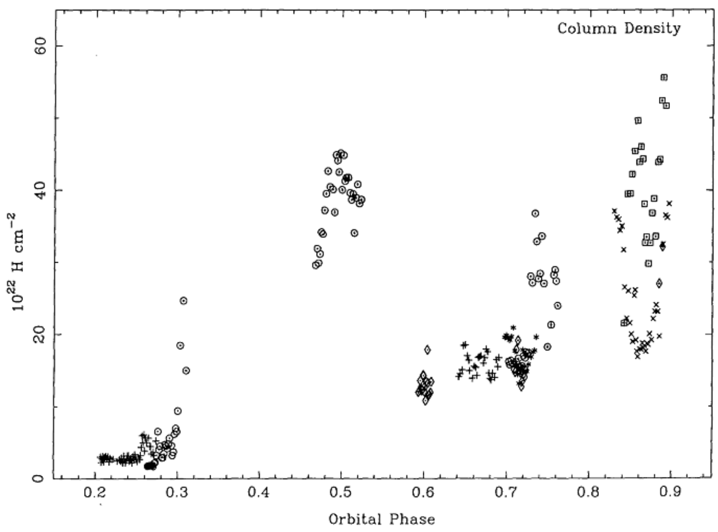

Figure 2.7: Absorption column density vs. orbital phase diagram for Vela X-1 (Haberl & White 1990). Different symbols indicate measurements from different binary cycles. The base level of absorption increases by a factor of 10 from phase 0.2 to 0.85 indicating the trailing denser material.

atom or an ion. The measured equivalent-widths (EW) of the *Fe* Kα line are relatively large $\geq$ 100 eV (White et al. 1983). White et al. (1983) discussed the origin of the line emitting region in the view of the fact that the matter should be relatively low ionized and cool. They ruled out the fluorescence of the plasma above hot spots and surface of the neutron star, since the former would be fully ionized by the intense radiation field and the latter would be red shifted by gravitation. This leaves two potential sites for the emission to be the stellar wind of the companion and the magnetosphere of the neutron star. In accretion powered pulsars, the correlation of Fe line intensity and the continuum intensity is the evidence that the iron line is produced by fluorescence of X-ray emission absorbed by the cool matter surrounding the pulsar (Ohashi et al 1984, Leahy et al. 1989). When n_{H} vs. Fe line EW values are plotted the correlation between the emission line and the absorbing matter is obvious for $n_{\mathrm{H}} \geq 10^{23}$ atoms cm^{-2} (see Figure 2.8).

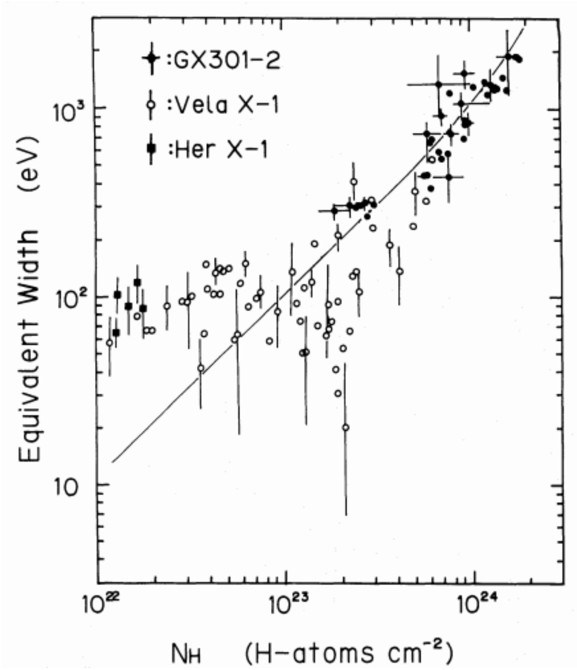

Figure 2.8: The measured equivalent-width (EW) of the Fe line vs. the column density of the absorbing matter (n_H) along the line of sight. The solid line indicates the predicted EW for a spectrum of photon index ~1.2 (Nagase 1989 and references therein).

2.6.4 Cyclotron Features

As an effect of the strong magnetic field of the neutron stars, cyclotron resonance scattering features (CRSFs) are observed in X-ray energies above 10 keV. The physical process causing CRSFs is the resonant scattering of photons by electrons whose energy states are quantized into Landau levels by the magnetic field (Meszaros 1992). Harmonically spaced line features in the spectra (E_o, 2 E_o, 3 E_o etc.) may arise as a result of the quantized energy levels of electrons. This feature is commonly known as cyclotron lines and the line energy can be used for direct measurement of the surface magnetic field.

For a non-relativistic electron spiraling around the magnetic field lines, the Larmor frequency implies that most of the radiation is emitted as a spectral line centered at the fundamental cyclotron resonance frequency:

$$\nu_{\rm cyc} = \frac{eB}{m_{\rm e}c} \tag{2.43}$$

where e and $m_{\rm e}$ are the charge and mass of electron. The corresponding energy for the frequency is $E_{\rm cyc} = \hbar\, \nu_{\rm cyc}$, $\hbar$ being the Planck constant. The observed resonance energy, $E_{\rm o}$ is actually red-shifted by the neutron stars gravitational field, $E_{\rm o} = E_{\rm cyc}(1+z)^{-1}$, where z is the gravitational red-shift. The relation of the observed line energy with the magnetic field is given by the equation:

$$E_{\rm o} = 11.6\, B_{12}(1+z)^{-1} \quad \text{keV} \tag{2.44}$$

where B_{12} is B in units of 10^{12} G. The red-shift factor can be calculated by the relation:

$$(1+z)^{-1} = \left(1 - \frac{2GM}{Rc^2}\right)^{1/2} \tag{2.45}$$

where R is the distance of the region where the line is formed from the center of the neutron star. Assuming $M = 1.4\ M_\odot$ and $R = 10^6$ cm one can calculate $(1+z)^{-1}$ as 0.76.

First discovery of CRSFs by Trümper et al. (1978) in Her X-1 ($E_{\rm o}$ ~40 keV) is followed by an enhancement in early 1990s due to the broad energy band of the satellite *Ginga*. Recent studies of Coburn et al. (2002) raised the number of accretion power pulsars that show CRSFs to ~13. Generally, CRSFs are modeled by Lorentzian or Gaussian distribution functions:

$$H(E) = -\ \frac{\tau\sigma^2 (E/E_{\rm o})^2}{(E-E_{\rm o})^2 + \sigma^2} \qquad \text{Lorentzian} \tag{2.46}$$

$$H(E) = \tau \exp\left(-\frac{(E-E_{\rm o})^2}{2\sigma^2}\right) \qquad \text{Gaussian} \tag{2.47}$$

where σ and τ are the width and optical depth of the line at energy $E_{\rm o}$. Since the basic continuum $N(E)$ is defined by Eqn. 2.41, CRSFs models modify the continuum as:

$$N(E) \rightarrow N(E)\ \exp(-H(E)) \tag{2.48}$$

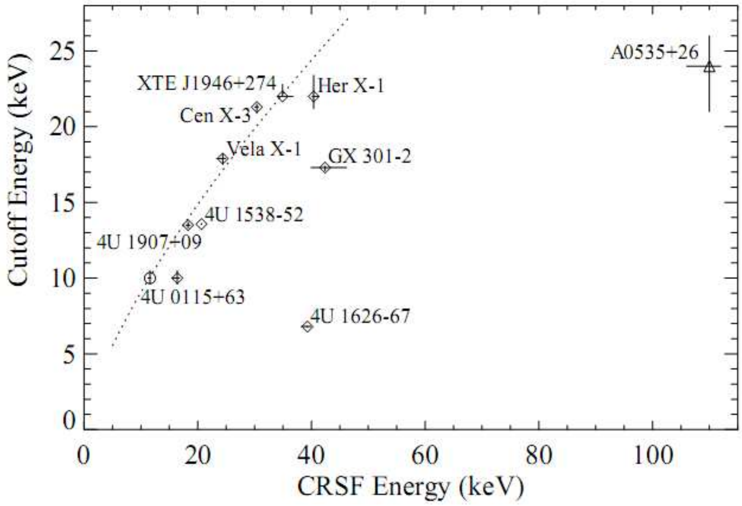

Figure 2.9: Cutoff energy E_{cut} vs. CRSF energy E_o for accretion powered pulsars (Coburn et al. 2002). The dotted line represents the power law correlation for $E_o \leq 35$ keV.

Table 2.2: Cyclotron line measurements and surface magnetic field strengths of accretion powered pulsars (Coburn et al. 2002)

System	E_o (keV)	B (10^{12} G)
Her X-1	40.4	4.5
4U 0115+63	11.6	1.3
Cen X-3	30.4	3.4
4U 1626-67	39.3	4.4
XTE J1946+274	34.9	3.9
Vela X-1	24.4	2.7
4U 1907+09	18.3	2.1
4U 1538-52	20.66	2.3
GX 301-2	42.4	4.8
4U 0532+309	28.6	3.2

Some of the cyclotron line measurements and the surface magnetic field strengths calculated by Eqn. 2.44 are given in Table 2.2.

One of the most interesting results obtained from the analysis of CRSFs is the positive correlation of cyclotron line energy with the high energy cutoff (Makishima et al. 1999, Coburn et al. 2002), which suggests that the high energy break of the spectra is related to the magnetic field (Tanaka 1986). Makishima et al. (1999) found that the relation is consistent with a power law of the form $E_{\mathrm{cut}} \propto E_{\mathrm{o}}^{0.7}$. At CRSF energies above 35 keV this trend saturates since relativistic effects become important (see Figure 2.9).

Two other correlations are reported for the parameters of CRSFs (Coburn et al. 2002). A correlation between the line width σ and energy E_{o} indicates that, electrons moving freely only along the magnetic field lines would result in a Doppler broadening at small viewing angles with respect to the magnetic field and the line is expected to be narrower at larger angles. Another correlation between the relative line width σ / E_{o} and optical depth τ indicates that, CRSFs become broader as they become deeper.

CHAPTER 3

4U 1907+09

The HMXB system 4U 1907+09, discovered in early 1970s by the *Uhuru* survey (Giaconni et al. 1971a), consists of an X-ray pulsar accreting material from its blue supergiant companion. 4U 1907+09 has been identified as a variable X-ray source during the observations of various X-ray missions such as; *OSO 7* (Markert et al. 1979), *Ariel V* (Seward et al. 1976, Marshall & Ricketts 1980), *HEAO 1* (Schwartz et al. 1980), *Tenma* (Makishima et al. 1984), *EXOSAT* (Cook & Page 1987), *Ginga* (Makishima & Mihara 1992, Mihara 1995, Makishima et al. 1999), *XMPC* (Chitnis et al. 1993), *BeppoSAX* (Cusumano et al. 1998), *RXTE* (in't Zand et al. 1997, 1998, Baykal et al. 2001, Roberts et al. 2001, Coburn et al. 2002, Baykal et al. 2006), *ASCA* (Roberts et al. 2001), *IXAE* (Mukerjee et al. 2001) and *INTEGRAL* (Fritz et al. 2006).

The binary orbital period of 4U 1907+09 was first determined to be ~8.4 d by Marshall and Ricketts (1980). They reported that the folded orbital profile shows two maxima where the separation of the large primary and the small secondary is roughly ~0.45 orbital phase. Further observations confirmed that the two peaks were actually

Table 3.1: Orbital solution of 4U 1907+09 taken from in't Zand et al. 1998. Confidence intervals are quoted at 1σ level.

Parameter	Symbol	Value
Orbital Epoch	$T_{\pi/2}$	MJD 50134.76±0.06
Orbital Period	P_{orb}	8.3753±0.0001 d
Eccentricity	e	0.28±0.04
Longitude of periastron	ω	$330^{\circ}\pm7$
Projected semi-major axis	$a_{\mathrm{x}}\sin i$	83±2 lt-s

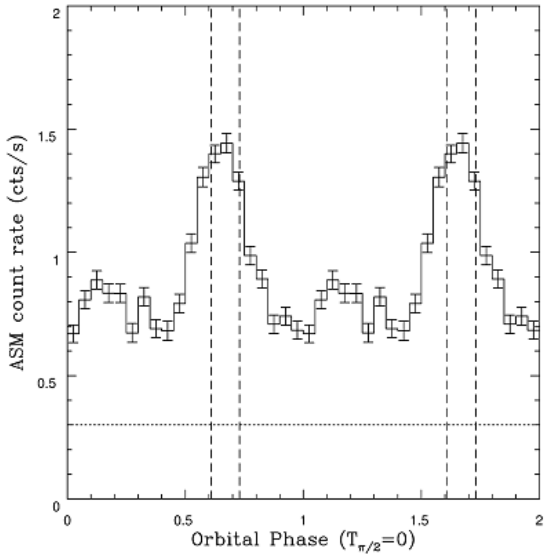

Figure 3.1: 4U 1907+09 *RXTE* - *ASM* light curve folded on 8.3753 d orbital period. Orbital epoch is used from in’t Zand et al. 1998 (see Table 3.1). The vertical dashed lines correspond to time of periastron passage within 68% confidence region. The dotted line is the level of positive flux bias. (Roberts et al. 2001)

phase-locked, the primary corresponding to periastron and the secondary to apastron (see Figure 3.1) (Cook & Page 1987, in’t Zand et al. 1998). Moreover, it was found that the pulsar is in an eccentric (e ~0.2) orbit around its companion (Makishima et al. 1984, Cook & Page 1987). A precise study of *RXTE* observations by in’t Zand et al. (1998) revised the orbital parameters of the system (see Table 3.1).

The spectral classification of the companion star has been a matter of debate for a long time. The companion was first identified optically as a highly reddened M_V = 16.4 magnitude star (Schwartz et al. 1980). It was proposed at that time that the companion is an O or B type supergiant based on the presence of strong and broad Hα emission. However, the presence of the two maxima per orbital period had led to the hypothesis of an equatorial disk like envelope around a B*e* type stellar companion (Makishima et al. 1984, Iye 1986, Cook & Page 1987). The neutron star was thought to be traversing this disk twice per orbit and consequently the accretion rate, therefore the X-ray flux, increasing temporarily. Although the high resolution spectroscopic measurements by Iye (1986) strengthened the suggestion of a B*e* companion, the position of 4U 1907+09 in the Corbet diagram (see Figure 1.4)

(Corbet 1984, 1986) was pointing that the companion is more likely to be a supergiant that underfills its Roche Lobe. Another contradiction to the B*e* scenario mentioned by Van Kerkwijk et al. (1989), was the strong interstellar absorption being inconsistent with the calculated distance (< 1.5 kpc). Recently, optical (Cox et al. 2005a, b) and infrared (Nespoli et al. 2008) studies have accomplished the debate. A lower limit of 5 kpc for the distance is set and an O8 - O9 Ia supergiant companion with dense stellar wind is proposed for the system (Cox et al. 2005a) (see Table 3.2 for more optical properties). Infrared studies have also confirmed and refined the spectral type as O8.5 Iab supergiant (Nespoli et al. 2008).

A standard power spectrum analysis of *Tenma* observations revealed another periodicity ~437 s, which was subsequently depicted as the spin period of the pulsar (Makishima et al. 1984). A double peak pulse profile with variable pulse amplitude was reported. Energy dependent pulse profiles were studied by in't Zand et al. (1998) (see Figure 3.2) and it was found that the profile is insensitive to energy between 2 and 20 keV, whereas dramatic changes are present above 20 keV with one peak disappearing. The energy dependence of the pulse profile reflects the fact that the physical circumstances of the two polar caps are different. Pulse characteristics of 4U 1907+09 was also analyzed by Mukerjee et al. (2001) and it was found that the pulsed fraction is almost constant at ~30% although the relative intensities of the two peaks are variable within days.

Table 3.2: Properties of the optical companion to 4U 1907+09. (Cox et al. 2005a)

Parameter	Symbol	Value
Visual Magnitude	M_V	16.37 mag
Color Excess	$E_{(B-V)}$	3.45 mag
Spectral Type	-	O8 - 09 Ia
Rotational Velocity	$v_r \sin i$	100 km s^{-1}
Effective Temperature	T_{eff}	30500 K
Mass	M_c	27 $M_\odot$
Radius	R_c	26 $R_\odot$
Luminosity	L_c	5×10^5 $L_\odot$
Mass Loss Rate	$\dot{M}$	7×10^{-6} $M_\odot$ yr^{-1}
Distance	d	5 kpc
Terminal Wind Velocity	v_∞	1710 km s^{-1}

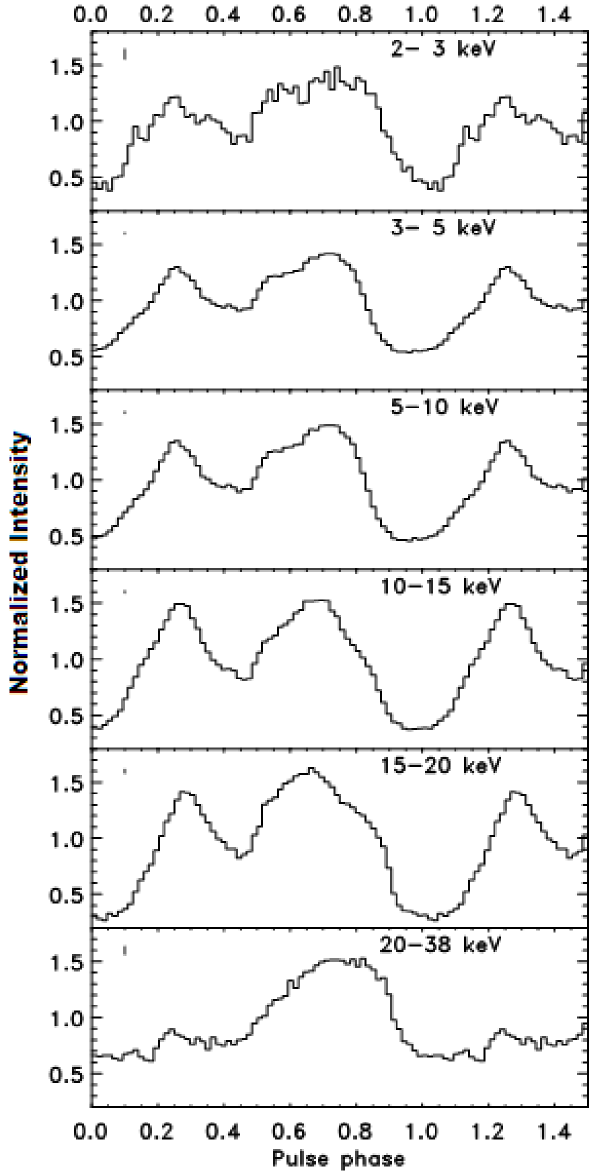

Figure 3.2: Pulse profiles of 4U 1907+09 for 6 different energy bands between 2 - 38 keV. Corresponding energy bands are given at the top of each panel and the statistical 1σ error is shown in the upper left corner. (in't Zand et al. 1998)

The historical measurements of pulse period (see Table 3.3 and Figure 3.3) confirm that the pulsar had been steadily spinning down for more than ~15 years with an average rate of +0.225 s yr^{-1} (Cook & Page 1987, in't Zand et al. 1998, Baykal et al. 2001, Mukerjee et al. 2001). Afterwards, *RXTE* observations in 2001 showed a significant deviation from the steady spin-down rate with a pulse derivative of +0.115s yr^{-1}, approximately ~0.60 times lower than previous measurements (Baykal et al. 2006). It has recently been reported that the pulse period evolution has shown a torque reversal with a negative pulse derivative -0.158 s yr^{-1}, verifying a spin-up episode from MJD 53131 onwards (Fritz et al. 2006).

4U 1907+09 is a variable X-ray source, it shows intensity peaks called flaring activity and intensity fades below the detection threshold called dipping activity (in't

Table 3.3: The historical pulse period measurements of 4U 1907+09.

Date (MJD)	Instrument & Reference	Pulse Period (s)	Date (MJD)	Instrument & Reference	Pulse Period (s)
45576.5	*Tenma*, (1)	437.483±0.004	52061.5	*RXTE*, (5)	441.0595±0.0063
45850.7	*EXOSAT*, (2)	437.649±0.019	52088.0	*RXTE*, (5)	441.0650±0.0063
48156.6	*Ginga*, (3)	439.19±0.02	52117.4	*RXTE*, (5)	441.0821±0.0062
50134.8	*RXTE*, (4)	440.341±0.014	52141.2	*RXTE*, (5)	441.0853±0.0082
50424.3	*RXTE*, (5)	440.4854±0.0109	52191.4	*RXTE*, (5)	441.1067±0.0046
50440.4	*RXTE*, (6)	440.4877±0.0085	52217.2	*RXTE*, (5)	441.1072±0.0077
50460.9	*RXTE*, (5)	440.5116±0.0075	52254.3	*RXTE*, (5)	441.1259±0.0074
50502.1	*RXTE*, (5)	440.5518±0.0053	52292.0	*RXTE*, (5)	441.1468±0.0065
50547.1	*RXTE*, (5)	440.5681±0.0064	52328.8	*RXTE*, (5)	441.1353±0.0090
50581.1	*RXTE*, (5)	440.5794±0.0097	52739.3	*INTEGRAL*, (7)	441.253±0.005
50606.0	*RXTE*, (5)	440.6003±0.0115	52767.1	*INTEGRAL*, (7)	441.253±0.005
50631.9	*RXTE*, (5)	440.6189±0.0089	53083.9	*INTEGRAL*, (7)	441.283±0.005
50665.5	*RXTE*, (5)	440.6323±0.0069	53121.1	*INTEGRAL*, (7)	441.274±0.005
50699.4	*RXTE*, (5)	440.6460±0.0087	53133.4	*INTEGRAL*, (7)	441.297±0.005
50726.8	*RXTE*, (5)	440.6595±0.0105	53253.6	*INTEGRAL*, (7)	441.224±0.010
50754.1	*RXTE*, (5)	440.6785±0.0088	53291.3	*INTEGRAL*, (7)	441.201±0.005
50782.5	*RXTE*, (5)	440.6910±0.0097	53314.0	*INTEGRAL*, (7)	441.188±0.005
51021.9	*RXTE*, (6)	440.7045±0.0032	53324.7	*INTEGRAL*, (7)	441.183±0.005
51080.9	*RXTE*, (6)	440.7598±0.0010	53443.4	*INTEGRAL*, (7)	441.154±0.005
51993.8	*RXTE*, (5)	441.0484±0.0072	53473.3	*INTEGRAL*, (7)	441.139±0.005
52016.8	*RXTE*, (5)	441.0583±0.0071	53503.8	*INTEGRAL*, (7)	441.124±0.005

References: (1) Makishima et al. 1984, (2) Cook & Page 1987, (3) Mihara 1995, (4) in't Zand et al. 1998, (5) Baykal et al. 2006, (6) Baykal et al. 2001, (7) Fritz et al. 2006

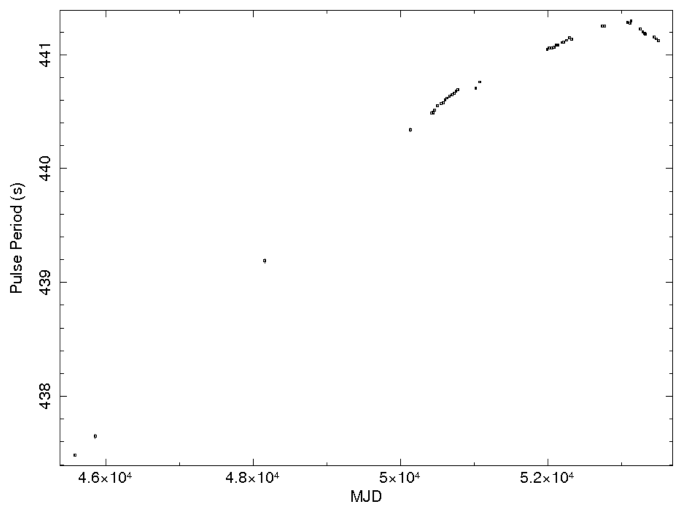

Figure 3.3: Pulse period history of 4U 1907+09 (see Table 3.3 for data and references).

Zand et al. 1997). It is reported that ~20% of the observations were in dipping state with no detectable pulsed emission and the typical time-scale of the dips was between few minutes to 1.5 hours. In't Zand et al. (1997) also noted the absence of strongly increased absorption during the dips. Therefore; these variations in the X-ray flux are accepted to be the evidences of the instability in mass accretion rate from the inhomogeneous wind of companion star, such that the dipping states are associated with the cessation of accretion. A sudden increase of intensity on time-scale of hours is often observed from 4U 1907+09 and it is correlated with enhancement of accreting material (Makishima et al. 1984, in't Zand et al. 1998, Mukerjee et al. 2001, Fritz et al. 2006). Detailed timing analysis of these flaring episodes revealed QPOs with frequencies ~0.055 Hz (in't Zand et al. 1998) and ~0.069 Hz (Mukerjee et al. 2001).

In order to explain the long term spin-down behavior of some pulsars (i.e. G-X 1+4, 4U 1626-67, Vela X-1) as in the case of 4U 1907+09; mainly two scenarios are considered: inhibition of accretion and formation of a transient accretion disk.

The centrifugal inhibition of accretion (i.e. propeller effect) occurs when the magnetospheric radius (r_m) extends beyond co-rotation radius (r_{co}). Mukerjee et al.

(2001) calculated r_{co} ~$9.8\text{x}10^9$ cm and r_m ~$4.1\text{x}10^8$ cm for the typical non-dip luminosity of 4U 1907+09 where $r_{co} > r_m$. As discussed in section 2.2.1 of the previous chapter, propeller mechanism may turn on if the mass accretion rate is low enough such that the material is not sufficient to squeeze the magnetosphere. The limit to the luminosity that turn off the propeller mechanism can be derived from the condition $r_{co} = r_m$ (Illarionov & Sunyaev 1975):

$$L = 2\times10^{37}\, R_6^{-1}\, \mu_{30}^2\, P_{\text{spin}}^{-7/3} \left(\frac{M}{1.4\,M_\odot}\right)^{-2/3} \quad \text{erg s}^{-1} \qquad (3.1)$$

The limiting luminosity is $6\text{x}10^{31}$ erg s^{-1} for the case of 4U 1907+09. The dipping states of the pulsar are candidate episodes for propeller regime since the count rates are below detection threshold at those times.

The detection of QPOs during flaring states of 4U 1907+09 is an indicator for the formation of a transient accretion disk. As discussed in section 2.5 of the previous chapter, basic models of QPOs fall into three categories. The model that involves accretion flow instabilities can not be applied for the QPOs of 4U 1907+09 since the luminosity of this system ($4\text{x}10^{36}$ erg s^{-1}) is far from Eddington limit (see Eqn. 2.1). Other models considering the relation of the QPO frequency with the Keplerian motion of the accreting material are plausible. In these models the radius of a putative disk depends on the QPO frequency. So, by using Eqn. 2.8 and the ~0.069 Hz QPO (Mukerjee et al. 2001), the radius is estimated as r_{disk} ~$9.9\text{x}10^8$ cm which is below r_{co}. If the disk is retrograde it can supply the necessary negative torque that causes spin-down. The observed torque is generally expressed as:

$$N_{\text{obs}} = 2\pi I_s \left|\dot{\nu}\right| \qquad (3.2)$$

If one uses the moment of inertia of a neutron star, $I_s = 10^{45}$ gr cm^2 and the rate of change of frequency of 4U 1907+09, $\dot{\nu} = -3.54\text{x}10^{-14}$ Hz s^{-1} the observed torque is found as $2.3\text{x}10^{32}$ gr cm^2. The characteristic torque supplied by all accreting material at r_{disk} is expressed as:

$$N_{\text{char}} = \eta \dot{M} \left(GM\, r_{\text{disk}}\right)^{1/2} \qquad (3.3)$$

where η is the duty cycle. Here, $\dot{M}$ can be calculated from the luminosity by using Eqn. 2.2 and it is found for the flaring luminosity of 4U 1907+09 as 1.8×10^{16} gr s^{-1}. Consequently, N_{char} is found as $\eta(80\times10^{32}$ gr $cm^2)$. A duty cycle of 0.0295 is estimated by equalizing Eqn. 3.2 and 3.3. This duty cycle corresponds to duration of 0.247 d which is too short when compared to the observed flaring time-scales. However, the brightening of 4U 1907+09 during periastron passage due to increased $\dot{M}$, have a duration of ~0.92 d and this is long enough for a disk formation.

As discussed in section 2.3.3 of the previous chapter, the retrograde disk model implies a torque and luminosity correlation (Murray et al. 1999). Furthermore, another model considering a transition to sub-Keplerian ADAF requires spectral changes (Yi et al. 1997). The recent torque reversal of 4U 1907+09 is difficult to reconcile with these models since neither effect is present through the torque variations (Baykal et al. 2006, Fritz et al. 2006). Fritz et al. (2006) stated that the most appropriate model to explain a torque reversal without a significant change in X-ray flux, is the model of Perna et al. (2006) in which a torque reversal is possible without a change in the mass accretion rate.

X-ray spectra of 4U 1907+09 studied by various missions (Schwartz et al. 1980, Marshall & Ricketts 1980, Makishima et al. 1984, Cook & Page 1987, Chitnis et al. 1993, Mihara 1995, in't Zand et al. 1997, Cusumano et al. 1998, Makishima et al. 1999, Roberts et al. 2001, Coburn et al. 2002, Baykal et al. 2006, Fritz et al. 2006) can be basically described by a power law with an exponential cutoff at ~13 keV (see Eqn. 2.41). The power law photon index is between ~0.8 and ~1.5 (see Figure 3.4a). The continuum is modified by photoelectric absorption with a highly variable hydrogen column density (n_H) over the binary orbit, between 1×10^{22} cm^{-2} and 9×10^{22} cm^{-2} (in't Zand et al. 1997). The increase in n_H just after periastron passage of the pulsar (see Figure 3.4b), implies that the location of the absorbing material is the dense stellar wind of the companion star (Roberts et al 2001). Leahy (2001) and Roberts et al. (2001) modeled the absorption profile according to theoretical wind models in order to describe the existence of the secondary maximum in the folded orbital profile (see Fig. 3.1 and 3.4b). They have proposed that the most probable

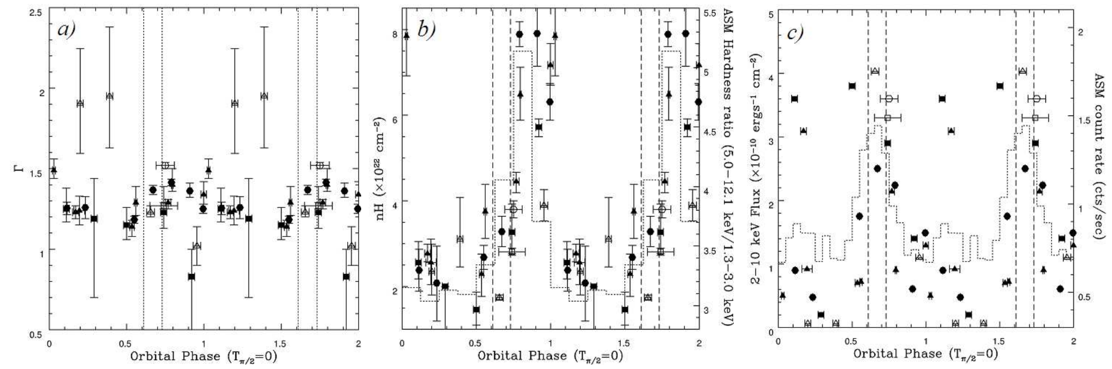

Figure 3.4: Multi-mission measurement of a) photon index (Γ), b) hydrogen column density (n_H), c) 2 - 10 keV flux; as a function of orbital phase (Roberts et al. 2001 and references therein). *Open triangles*: *ASCA*, *filled triangles*: February 1996 *RXTE*, *open squares*: *BeppoSAX*, *filled squares*: *EXOSAT*, *open hexagons*: Tenma and *filled hexagons*: December 1996 *RXTE* measurements. The histogram in Fig. b) is the *RXTE* - *ASM* hardness ratio of the count rates from channel 3 over channel 1. The histogram in Fig. c) is the folded light curve from *RXTE* - *ASM*. The vertical dashed lines in all panels correspond to time of periastron passage within 68% confidence region.

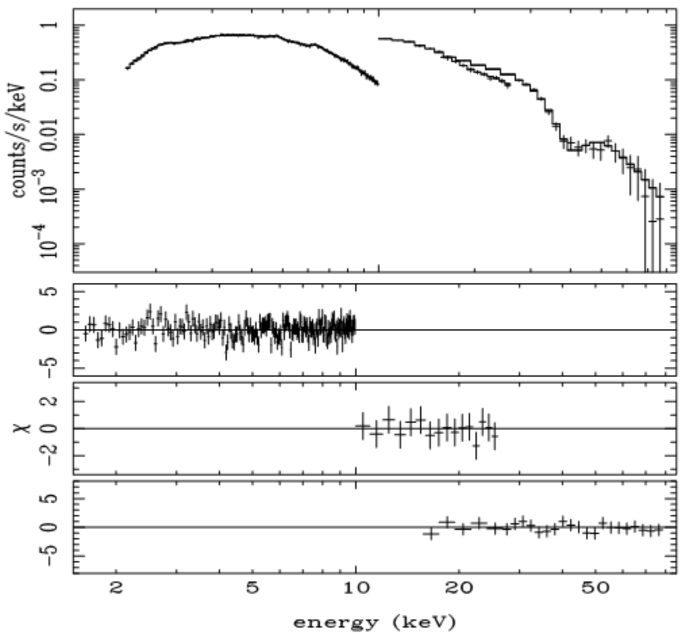

Figure 3.5: 1.6 - 80 keV spectrum of 4U 1907+09 with the best fit model (top panel). Residuals are shown separately for each *NFI* on board *BeppoSAX* (bottom three panels) (Cusumano et al. 1998).

mechanism for 4U 1907+09 is accretion from a spherical wind with equatorially enhanced dense spiral stream of gas around the companion star.

The extensive study of energy spectra of 4U 1907+09 observations with *Ginga* (Mihara 1995, Makishima et al. 1999) and *BeppoSAX* (Cusumano et al. 1998) exhibit CRSFs at ~18.8 keV and ~39.4 keV which correspond to the fundamental and the second harmonic cyclotron lines. Various models used to fit the CRSFs are given by Eqn.s 2.46 and 2.47. As discussed in section 2.6.4 of the previous chapter, CRSFs can be used for direct measurement of the surface magnetic field strength of the star. Equating Eqn.s 3.44 and 3.45 for 4U 1907+09 gives a value of $2.1\text{x}10^{12}$ G for the surface magnetic field strength (Cusumano et al. 1998). Mihara (1995) and Makishima et al. (1999) analyzed pulse phase resolved spectra to examine the changes of the CRSFs through the pulse period. They obtained the observed cyclotron line energy in the range 17 - 21 keV and found that the line becomes deepest during the leading edge of the main peak of the pulse profile.

Another feature reported in the spectra of 4U 1907+09 is a narrow emission line around 6.4 keV corresponding to Fe Kα line (Makishima et al. 1984, Mihara 1995, Cusumano et al. 1998, Makishima et al. 1999). However, an appropriate determination of the background by considering nearby supernova W49B and Galactic ridge emission ruled out the existence of a Fe line in the *RXTE* spectra (in't Zand et al. 1997, Roberts et al. 2001, Baykal et al. 2006). A recent analysis of *Suzaku* observations has provided the best determination of the weak line at 6.4 keV with an EW ~70 eV and also the first detection of a soft excess below 2 keV (Pottschmidt et al. 2007).

CHAPTER 4

OBSERVATIONS AND DATA ANALYSIS

X-ray spectral and timing studies of the HMXB 4U 1907+09 presented in this thesis is based on *RXTE - PCA* and *INTEGRAL - JEM-X* and *IBIS-ISGRI* observations. In this chapter, a brief description of observations, instruments, data reduction procedures and analysis techniques are provided.

4.1 *RXTE* Observations

RXTE monitoring observations of 4U 1907+09 with the proposal ID 93036 were held on between June 2007 and December 2008. There are 39 pointed observations each having an average exposure time ~2 ks. Details of these observations are given in Table 4.1.

There are three main instruments on board *RXTE* satellite: *PCA* (2 - 60 keV; Jahoda et al. 1996), *HEXTE* (15 - 250 keV; Rothschild et al. 1998) and *ASM* (2 - 10 keV; Levine et al. 1996). The data products of *Proportional Counter Array* (*PCA*) are reduced for the analysis in this thesis.

PCA is a pointed instrument (Jahoda et al. 1996) which consists of five co-aligned identical proportional counter units (PCUs). The detectors are sensitive in the energy range 2 - 60 keV. The effective area of each detector is approximately ~1300 cm^2 and the energy resolution is 18% at 6 keV. A field of view (FOV) of 1° at full width at half maximum (FWHM) is small enough that, with the large geometric area, *PCA* provides a highly sensitive time resolution. Operations are carried on with various PCUs turned off during observations in order to extend the life time of the instrument. The number of running PCUs during the observations of 4U 1907+09 varies between one and three.

Table 4.1: Log of *RXTE* observations of 4U 1907+09.

Observation ID	Exposure (s)	Mid-time (MJD)	Orbital Phase	State	Mean *PCA* count/s	Pulsed Fraction
93036-01-01-00	1903	54280.65	0.01	Source on	178.02±1.37	0.41±0.03
93036-01-02-00	1956	54282.41	0.22	Partial dip	36.83±0.48	0.24±0.07
93036-01-03-00	1775	54284.37	0.46	Dip	45.20±0.42	0.07±0.04
93036-01-04-00	1825	54299.64	0.28	Source on	170.96±1.39	0.43±0.03
93036-01-05-00	1752	54314.35	0.04	Partial dip	33.97±0.72	0.33±0.11
93036-01-06-00	1758	54330.40	0.95	Partial dip	86.14±1.10	0.25±0.07
93036-01-07-00	2080	54346.23	0.84	Source on	133.91±1.00	0.40±0.03
93036-01-08-00	1888	54360.36	0.53	Source on	337.20±2.07	0.38±0.02
93036-01-09-00	1704	54374.18	0.18	Partial dip	51.98±1.43	0.51±0.13
93036-01-10-00	1776	54388.52	0.89	Source on	203.70±2.03	0.47±0.04
93036-01-11-00	2760	54403.96	0.74	Source on	323.99±2.00	0.38±0.02
93036-01-12-00	1832	54417.97	0.41	Source on	167.81±1.19	0.32±0.03
93036-01-13-00	2009	54434.07	0.33	Partial dip	186.46±2.53	0.44±0.08
93036-01-14-00	1953	54450.24	0.26	Partial dip	85.16±1.11	0.23±0.06
93036-01-15-00	1920	54462.07	0.68	Source on	238.80±1.59	0.37±0.02
93036-01-16-00	2016	54478.76	0.67	Source on	290.97±2.04	0.34±0.03
93036-01-17-00	1920	54493.81	0.47	Source on	189.43±1.73	0.46±0.04
93036-01-18-00	1889	54509.27	0.31	Dip	26.53±0.47	0.14±0.09
93036-01-19-00	1656	54524.98	0.19	Source on	184.88±1.59	0.44±0.04
93036-01-20-00	1664	54539.69	0.94	Partial dip	55.14±0.99	0.32±0.09
93036-01-21-00	1534	54554.03	0.66	Source on	228.95±1.77	0.39±0.03
93036-01-22-00	2159	54569.15	0.46	Source on	239.38±1.62	0.45±0.03
93036-01-23-00	1571	54584.38	0.28	Partial dip	20.10±0.58	0.33±0.18
93036-01-24-00	1867	54599.50	0.08	Source on	111.48±1.01	0.39±0.04
93036-01-25-00	2022	54614.75	0.90	Source on	128.71±1.36	0.33±0.05
93036-01-26-00	1936	54629.27	0.64	Partial dip	68.36±0.56	0.11±0.04
93036-01-27-00	2387	54644.45	0.45	Source on	105.65±1.02	0.43±0.05
93036-01-28-00	1952	54659.77	0.28	Source on	122.50±1.20	0.37±0.05
93036-01-29-00	2117	54674.61	0.05	Source on	227.29±2.22	0.54±0.04
93036-01-30-00	1896	54689.53	0.83	Source on	145.44±1.21	0.41±0.04
93036-01-31-00	1775	54705.45	0.73	Source on	330.53±2.44	0.42±0.03
93036-01-32-00	1943	54719.84	0.45	Dip	15.24±0.59	0.23±0.21
93036-01-33-00	1785	54734.02	0.15	Partial dip	52.09±0.84	0.34±0.09
93036-01-34-00	1927	54749.14	0.95	Partial dip	67.89±1.19	0.39±0.10
93036-01-35-00	1926	54764.39	0.77	Source on	203.67±1.36	0.31±0.03
93036-01-36-00	1679	54779.32	0.55	Dip	56.19±0.53	0.08±0.05
93036-01-37-00	1971	54795.07	0.44	Source on	171.75±1.52	0.48±0.04
93036-01-38-00	2232	54809.20	0.12	Source on	101.16±0.99	0.41±0.05
93036-01-39-00	2079	54825.16	0.03	Source on	246.14±1.63	0.38±0.03

The standard *RXTE* analysis software 'HEASOFT v.6.4' is used for data reduction. The filtering applied to the data comprises excluding the times when, elevation angle is less than 10° and offset from the source is greater than 0.02°. Electron contamination of PCU2 is also confirmed to be less than 0.1. The latest *PCA* background estimator models supplied by the *RXTE* Guest Observer Facility (GOF), Epoch 5C are used to generate the background light curves and spectra. The model estimation is based on the rate of very large solar events, spacecraft activation and cosmic X-ray emission.

4.1.1 Spectral Analysis

According to the announcements done by the *PCA* instrument team, background levels of PCU0 and PCU1 have increased due to the loss of their propane layers. As it is recommended not to use data of these PCUs for spectral extraction, the only data products taken into consideration during spectral analysis belong to PCU2. The 'Standard2f' mode data with 128 energy channels and a time resolution of 16 s are examined for the spectral extraction. The energy range is restricted to 3 - 25 keV taking into consideration the fact that *PCA* instrument count statistics is poor beyond this range. The spectral analysis is done by using the program 'XSPEC v.12.3.1'. A systematic error of 2% is applied during analysis to account for the uncertainties in the response matrices produced by using the task 'PCARSP' and in background modeling (Wilms et al. 1999).

Along with the basic estimation of *PCA* background models produced by using the task 'PCABACKEST', additional background estimation is needed because 4U 1907+09 is near the Galactic plane and the supernova remnant W49B. As mentioned before in the previous chapter, 4U 1907+09 has dipping episodes. During the dip states no significant pulsed emission is observed (see Figure A.2 of Appendix A for the light curves & Table 4.1 for the pulsed fractions) and the count rates are consistent with the diffuse emission from the Galactic ridge (see Table 4.1). About 20% of the processed *RXTE* observations are detected to be in dip state, so an average dip state spectrum is analyzed for comparison (see Figure 4.1). Models of diffuse emission from Galactic ridge consists of Raymond - Smith thermal plasma

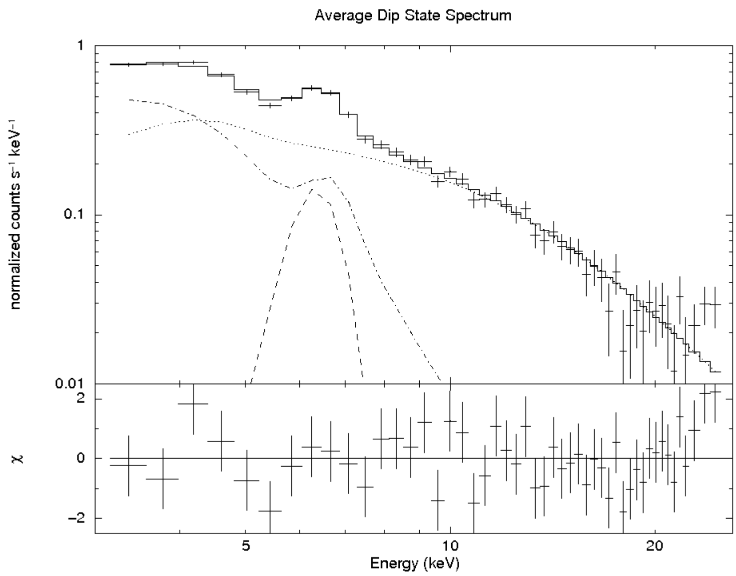

Figure 4.1: Average dip state spectrum modeled with power law (*dotted line*), Raymond - Smith thermal plasma (*dashed-dotted line*) and a Gaussian at 6.4 keV (*dashed line*). Bottom panel shows the residuals of the fit.

Table 4.2: Best-fit spectral parameters of dip state spectrum.

Model Component	Parameter	Value
Absorption	n_{H} (10^{22} cm^{-2})	$1.61^{+2.16}_{-1.61}$
Power Law	Photon index	$1.49^{+0.17}_{-0.24}$
	Normalization	$3.79^{+2.17}_{-1.73} \times 10^{-3}$
Raymond - Smith	kT (keV)	$1.78^{+0.59}_{-0.44}$
	Abundance	1.00 (Frozen)
	Normalization	$5.45^{+5.21}_{-2.19} \times 10^{-2}$
Gaussian	Line Energy (keV)	6.4 (Frozen)
	Sigma (eV)	$27.44^{+19.01}_{-27.44}$
	Normalization	$1.67^{+0.53}_{-0.64} \times 10^{-4}$

*Red. χ^2 = 1.057 (42 d.o.f.)

**Unabsorbed Flux at 3 - 25 keV = $5.51^{+0.01}_{-2.84} \times 10^{-11}$ $erg\ cm^{-2}\ s^{-1}$

and power law components (Valinia & Marshall 1998). Since W49B has a strong emission feature at 6.4 keV (Miceli et al. 2006), an additional Gaussian model component is added during the analysis of dip state spectrum. It is found that the spectral parameters are consistent with the previous results (see Table 4.2). Consequently, the model estimated background is directly subtracted from each individual observation by using the task 'MATHPHA' and the resulting spectrum is used as source spectrum whereas the overall dip state spectrum is used as background spectrum in 'XSPEC'.

4.1.2 Timing Analysis

The loss of propane layers of PCU0 and PCU1 do not affect high resolution timing, therefore no PCU selection is done for the timing analysis. Since the timing resolution of Standard2f mode data is low, the Good-Xenon mode data are preferred with 256 energy channels and 1 s long binning. Model estimated background is subtracted from the data by using the task 'LCMATH' and the light curves are corrected for the variance in number of active PCUs by using the task 'CORRECTLC'. Furthermore, corrections to the barycenter of the Solar system ('FXBARY' task) and to the binary orbital motion of 4U1907+09 are done. For the correction of binary orbital motion, the orbital parameters deduced by in't Zand et al. (1998) are used (see Table 3.1).

Non-dipping light curves are analyzed to perform the pulse timing measurements. Each ~2 ks long light curve segment is folded on a statistically independent trial period (Leahy et al. 1983). A template pulse profile is constructed from the first three observations with a total exposure of ~6 ks by folding the data on the period giving the maximum χ^2. The template pulse, $g(\phi)$, and independent sample pulses, $f(\phi)$, are represented by Fourier series (Deeter & Boynton 1985):

$$g(\phi) = G_{\mathrm{o}} + \sum_{\mathrm{k}=1}^{m} G_{\mathrm{k}} \cos \mathrm{k}\left(\phi - \phi_{\mathrm{k}}\right) \tag{4.1}$$

$$f(\phi) = F_{\mathrm{o}} + \sum_{\mathrm{k}=1}^{m} F_{\mathrm{k}} \cos \mathrm{k}\left(\phi - \phi_{\mathrm{k}} + \Delta\phi_{\mathrm{k}}\right) \tag{4.2}$$

where m is the harmonic number. Comparison of $g(\phi)$ and $f(\phi)$ harmonic by harmonic gives the estimate of $\Delta\phi_k$ and the sample pulse phase is determined by the pulse phase offset $\delta\phi$ between the sample and the master pulse.

In order to estimate pulse frequency derivatives, the pulse phase offsets calculated from the cross-correlation analysis are fitted to a cubic polynomial:

$$\delta\phi = \phi_o + \delta\nu\left(t - t_o\right) + \frac{1}{2}\dot{\nu}\left(t - t_o\right)^2 + \frac{1}{6}\ddot{\nu}\left(t - t_o\right)^3 \qquad (4.3)$$

which is a third-order Taylor expansion. Here, t_o is the mid-time of the observation, ϕ_o is the phase offset at t_o, δv is the deviation from the mean pulse frequency, $\dot{\nu}$ and $\ddot{\nu}$ are the first and second pulse frequency derivatives. The results of this analysis are given in the next chapter.

Energy resolved light curves are constructed in order to search for variations in the pulse profile. Three energy bands are chosen as 3 - 10 keV, 10 - 20 keV and 20 - 40 keV. Corresponding channels are determined from the energy - channel conversion table provided by GOF. Light curves are folded on the corresponding pulse periods found in the pulse timing analysis. Pulse profiles are plotted with number of bins equal 20, by using the task 'EFOLD'. Pulsed fractions of each observation given in Table 4.1 are derived from the average pulse profiles by using the below equation:

$$PF = \left(I_{\max} - I_{\min}\right) / \left(I_{\max} + I_{\min}\right) \qquad (4.4)$$

where $I_{\max}$ and $I_{\min}$ are the maximum and minimum intensities of the pulse profile. The error of pulse fractions are calculated from the mean error of the bins, ΔI, using the equation:

$$\Delta PF = \frac{4\,\Delta I\, I_{\max}}{\left(I_{\max} + I_{\min}\right)^2} \qquad (4.5)$$

4.2 *INTEGRAL* Observations

The *INTEGRAL* observations analyzed in this thesis are obtained from the *INTEGRAL* Science Data Centre (ISDC) archive. All publicly available pointing observations subsequent to the previous study of 4U 1907+09 (Fritz et al. 2006) are selected considering both the good *IBIS-ISGRI* and *JEM-X* times to be above 1 ks. Selected observations, where the source is in the FOV, are held on between October 2005 and November 2007. The data consist of a total of 611 science windows (SCWs) (each ~3 ks) within revolutions 366 and 623. The log of *INTEGRAL* observations is given in Table 4.3.

There are four instruments on board the *INTEGRAL* satellite (Winkler et al. 2003): *OMC* (500 - 850 nm; Mas-Hesse et al. 2003) *JEM-X* (3 keV - 35 keV; Lund et al. 2003), *IBIS* (15 keV - 10 MeV; Ubertini et al. 2003) and *SPI* (20 keV - 8MeV; Vedrenne et al. 2003). The data products of *JEM-X* and *IBIS-ISGRI* detectors are analyzed in this thesis.

Imager on Board the INTEGRAL Satellite (*IBIS*) is a coded mask instrument. *IBIS* has a fully coded FOV of $8^{\circ}.3 \times 8^{\circ}.0$ and 12' angular resolution (FWHM) (Ubertini et al. 2003). *INTEGRAL Soft Gamma-Ray Imager* (*ISGRI*) is the upper layer of the *IBIS* instrument which operates in the energy range 15 keV - 1 MeV with an energy resolution of ~8% at 60 keV (Lebrun et al. 2003). *Joint European X-ray Monitor* (*JEM-X*) consists of two identical coded mask instruments, each of which having a fully coded FOV of $4^{\circ}.8$ diameter and 3' angular resolution (FWHM) (Lund et al. 2003). The energy resolution of *JEM-X* is ~13% at 10 keV. Operations are carried on with only one of the two *JEM-X* detectors turned on due to loss in sensitivity resulting from erosion of the microstrip anodes inside the detectors. During the observations analyzed in this thesis, *JEM-X1* was operating.

The data reduction of *INTEGRAL* observations is performed by 'OSA v.7.0'. The standard pipeline processing comprises gain correction, good-time handling, dead-time derivation, background correction and energy reconstruction.

Images in two energy bands (20 - 40 keV and 40 - 60 keV) are produced from *IBIS-ISGRI* data with the use of an input catalogue consisting strong sources in the

Table 4.3: Log of *INTEGRAL* observations of 4U 1907+09.

Revolution	Exposure of *IBIS* (ks)	Time (MJD)	Orbital Phase	Mean count/s (in 20 - 40 keV)
366	84.74	53655.73 - 53657.87	0.40 - 0.65	1.46±0.11
367	91.36	53659.44 - 53660.87	0.84 - 0.01	2.54±0.10
368	104.54	53661.32 - 53663.65	0.07 - 0.35	1.15±0.10
369	38.14	53664.35 - 53664.97	0.43 - 0.50	0.13±0.16
373	98.07	53676.32 - 53677.49	0.86 - 0.00	2.01±0.09
375	2.17	53684.71	0.86	4.64±0.57
379	97.26	53694.27 - 53695.53	0.00 - 0.15	1.58±0.10
415	2.17	53801.97	0.86	3.92±0.71
423	143.02	53825.89 - 53828.27	0.72 - 0.00	1.91±0.09
427	2.17	53839.94	0.39	1.60±0.69
431	16.58	53850.03 - 53852.14	0.60 - 0.85	1.89±0.24
435	4.34	53861.90	0.02	0.17±0.52
441	2.26	53881.71	0.38	1.59±0.61
476	20.98	53984.12 - 53984.37	0.61 - 0.64	10.06±0.29
478	20.19	53990.10 - 53990.34	0.32 - 0.35	4.55±0.26
480	20.19	53996.08 - 53996.32	0.04 - 0.06	0.47±0.24
481	17.17	54001.40 - 54001.61	0.67 - 0.70	5.20±0.27
486	17.17	54016.35 - 54016.55	0.46 - 0.48	-0.07±0.25
489	17.19	54025.29 - 54025.50	0.52 - 0.55	1.82±0.27
491	21.60	54029.13 - 54029.38	0.98 - 0.01	0.59±0.23
493	17.16	54037.27 - 54037.47	0.95 - 0.98	2.79±0.27
495	20.02	54040.95 - 54041.19	0.39 - 0.42	3.73±0.26
497	20.18	54046.93 - 54047.17	0.11 - 0.14	0.72±0.23
499	20.01	54052.92 - 54053.16	0.82 - 0.85	0.85±0.24
501	20.01	54058.87 - 54059.11	0.53 - 0.56	0.47±0.23
537	20.07	54166.76 - 54167.00	0.42 - 0.44	0.98±0.24
539	22.34	54173.02 - 54173.28	0.16 - 0.19	2.15±0.22
540	20.92	54177.35 - 54177.60	0.68 - 0.71	7.48±0.26
542	20.08	54181.72 - 54181.96	0.20 - 0.23	0.93±0.24
544	20.07	54187.70 - 54187.94	0.92 - 0.94	0.90±0.24
546	20.97	54195.47 - 54195.72	0.84 - 0.87	2.12±0.24
549	21.60	54202.66 - 54202.92	0.70 - 0.73	2.18±0.23
551	20.19	54208.66 - 54208.90	0.42 - 0.45	3.52±0.24
553	20.03	54214.46 - 54214.70	0.11 - 0.14	3.28±0.24
555	78.69	54220.82 - 54222.84	0.87 - 0.11	1.44±0.12
556	91.44	54223.44 - 54225.74	0.18 - 0.46	2.56±0.12
557	20.12	54226.43 - 54226.67	0.54 - 0.57	1.50±0.24
559	20.12	54232.42 - 54232.66	0.25 - 0.28	0.57±0.26
561	17.26	54240.71 - 54240.74	0.24 - 0.27	0.93±0.26
599	20.15	54352.07 - 54352.31	0.54 - 0.57	4.99±0.26
601	20.04	54358.22 - 54358.46	0.28 - 0.30	1.64±0.22
603	20.04	54364.35 - 54364.59	0.01 - 0.04	0.18±0.22

Table 4.3: (continued)

Revolution	Exposure of *IBIS* (ks)	Time (MJD)	Orbital Phase	Mean count/s (in 20 - 40 keV)
607	20.05	54376.17 - 54376.41	0.42 - 0.45	1.04±0.24
608	85.72	54379.17 - 54381.52	0.78 - 0.06	1.41±0.11
609	75.76	54382.01 - 54384.39	0.12 - 0.40	1.53±0.12
610	20.05	54385.14 - 54385.38	0.49 - 0.52	2.93±0.24
611	20.04	54389.73 - 54389.97	0.04 - 0.07	0.39±0.23
612	80.10	54391.13 - 54393.45	0.21 - 0.48	1.20±0.11
613	87.13	54393.94 - 54396.36	0.54 - 0.83	2.18±0.11
614	20.01	54396.93 - 54397.17	0.90 - 0.93	1.53±0.23
615	22.67	54401.89 - 54402.16	0.49 - 0.52	0.43±0.22
617	18.80	54405.92 - 54406.14	0.97 - 0.00	-0.20±0.22
619	20.15	54413.71 - 54413.95	0.90 - 0.93	1.18±0.22
621	20.01	54417.86 - 54418.10	0.40 - 0.43	1.02±0.21
623	17.32	54423.89 - 54424.11	0.12 - 0.14	0.69±0.23

FOV: Ser X-1, XTE J1855-026, 4U 1909+07, SS 433, IGR J19140+0951, GRS 1915+105 and 4U 1907+09. The source positions are fixed at values given in the ISDC reference catalogue version 28. The third 'SEARCHMODE' is preferred for an efficient cleaning of ghost images caused by the coded mask modulation. The software is allowed to clean negative ghosts along with the positive ones by selecting 'NEGMODELS' to be 1. No pixel spread of counts is permitted to optimize the flux and signal-to-noise ratio (SNR) evaluation. The background maps provided by the ISGRI team are used for background correction. The standard tools of 'OSA v.7.0' are used to extract X-ray spectra of *IBIS-ISGRI* observations. Spectra are extracted in the energy range 18 - 80 keV by applying a user defined response matrix. Light curves are created by the tool 'II_LIGHT' distributed with 'OSA' which allows high resolution timing. 'II_LIGHT' uses Pixel Illuminated Fraction (PIF), while the standard light curve extraction tool of OSA builds shadowgrams for each requested time and energy bin to create light curves. Extracted light curves with 10 s long binning, are corrected to the solar system barycenter by using the task 'BARYCENT'.

Mosaic images in two energy bands (3 - 15 keV and 15 - 35 keV) are produced from *JEM-X1* data with the use of an input catalogue consisting

4U 1907+09 since the source is too weak to be detected in SCW level. The source position is fixed to be the catalogue position. X-ray spectra and background subtracted light curves are extracted using standard tools in ‘OSA v.7.0’. *JEM-X1* spectra with 256 energy channels are regrouped by a factor of 4 by using the task ‘GRPPHA’ in order to increase the SNR.

The analysis of X-ray spectra is done with the program ‘XSPEC v.12.5.0’. During simultaneous fitting of 4 - 20 keV *JEM-X1* and 18 - 80 keV *IBIS-ISGRI* spectra, a constant factor is included in the model to account for the normalization uncertainty between the two instruments. A systematic error of 4% is applied during the analysis (Goldwurm et al. 2003).

CHAPTER 5

OBSERVATIONAL RESULTS AND DISCUSSION

5.1 Energy Spectra

The basic spectral features of accretion powered pulsars have been described in section 2.6 of the second chapter. As discussed in the third chapter, X-ray spectra of 4U 1907+09 shows all features attributed to accretion powered pulsars; such as a power law continuum with an exponential cutoff, variable photoelectric absorption, cyclotron absorption lines and Iron Kα emission line.

X-ray spectra of 4U 1907+09, obtained by analyzing the data introduced in Table 4.1 and 4.3, are first modeled with a simple power law (PL), a high energy cutoff (see Eqn. 2.41) and photoelectric absorption (see Eqn. 2.42). The reduced χ^2 values of this elementary fit are not acceptable with values bigger than 2. The major deviations of the model from the data are seen around ~20 keV, ~40 keV and ~6 - 7 keV.

The existence of CRSFs at ~18.8 keV and ~39.4 keV were reported by Mihara (1995), Cusumano et al. (1998) and Makishima et al. (1999). Among the several models tested to fit CRSFs, best results are obtained when a component of cyclotron absorption ('cyclabs' model in 'XSPEC'; Mihara et al. 1990, Makishima et al. 1990) is added to the elementary model. This model consists of two Lorentzian distribution functions (see Eqn. 2.46) corresponding to two harmonically spaced lines, i.e. the fundamental and the second harmonic. The fundamental line energy is first tried to be fixed at the reported value, but better statistics is achieved when it is set free. The depth of the second harmonic is set to be zero wherever the spectral data does not cover the required energy range.

The residuals of the fits around ~6 - 7 keV correspond to the weak Fe emission line of 4U 1907+09. This feature has recently been approved by Pottschmidt et al. (2007) with the line energy being ~6.4 keV and the EW ~70 eV. In order to model this feature, a component of a simple Gaussian line profile with fixed energy is added to the model. Generally, the addition of the Gaussian did not improve the fits causing most of the other parameters to be pegged. The main reason of this failure is that, the sensitivity of the instruments used in the observations (*RXTE - PCA, INTEGRAL - JEM-X*) is not enough to resolve the line. It is necessary to observe the source with high resolution spectroscopic instruments like *XMM-Newton*, in order to identify the feature around 7 keV.

Although the simple PL model is successful to describe the continuum, another model called NPEX is tested on the data. This model is introduced by Mihara (1995) with the attempt to better describe the continuum in the view of the fact that the local slope of pulsar spectra often flattens before it cuts off steeply. NPEX model consists of negative and positive power laws with a common exponential cutoff factor. The functional form is:

$$C\,(E) = \left(A_{\mathrm{n}}\, E^{-\alpha} + A_{\mathrm{p}}\, E^{+\beta}\right) \exp\left(-\frac{E}{E_{\mathrm{fold}}}\right) \tag{5.1}$$

where A_{n} and A_{p} are the normalizations of the negative and positive power laws respectively (Makishima et al. 1999). The negative power law dominates over the positive one at low energies such that; the model reduces to a simple PL. However; the positive power law dominating at higher energies, simulates a slightly concave

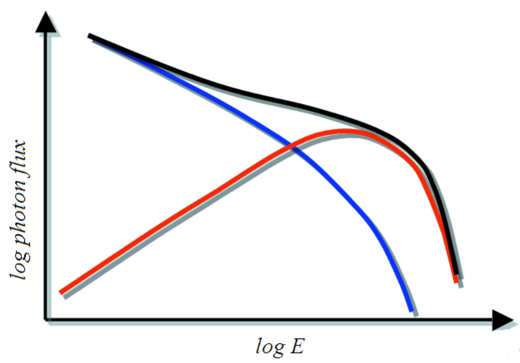

Figure 5.1: An illustration of the NPEX model.

curvature on the log-log plot (see Figure 5.1). When the positive index β is set to be equal to 2, the positive power law component actually simulates the Wien hump at $E \sim E_{\mathrm{fold}}$. NPEX model physically represents the thermal Comptonization in plasma of temperature T, where $E_{\mathrm{fold}} = kT$. At energies much higher than kT, a thermal rollover is demonstrated by the model.

Modeling the spectra of 4U 1907+09 with NPEX gives reasonable results but the single parameter errors are mostly found bigger than the simple PL model. Moreover, it was again not possible to constrain the Fe line parameters. Makishima et al. (1999) have discussed that NPEX model is better for data that covers wide energy range, whereas simple PL model is more adequate in narrower energy bands. This discussion is essentially supported by the results of the analysis; since NPEX is more satisfactory when it is used to model *INTEGRAL* spectra which cover a wider energy range than *RXTE* spectra.

5.1.1 *RXTE* Spectra

The *RXTE - PCA* spectra in the energy range 3 - 25 keV are fitted with the models described in the section above. In this part; first, the best fit results of the time-averaged overall spectrum is given in subsection 5.1.1.1. Second, the best fit results of the orbital phase resolved spectra are given in subsection 5.1.1.2.

5.1.1.1 Time Averaged Spectrum

The overall spectrum of non-dip observations, with a total exposure time of ~56 ks, is first modeled with the elementary model, a simple PL with an exponential cutoff and photoelectric absorption. This fit was unacceptable with a reduced χ^2 value of 2.79 and deviating residuals around ~20 keV and ~7 keV (see Figure 5.2). Adding the model component 'cyclabs' fairly improved the fit; such that the reduced χ^2 value decreased to 1.07. The fundamental line energy is set as a free parameter and the depth of the second harmonic is fixed at zero. Further analysis by adding a Gaussian for the Fe line gave a reduced χ^2 value of 0.93 but it was not possible to set the Gaussian parameters as free. Therefore, line energy and sigma are fixed at values

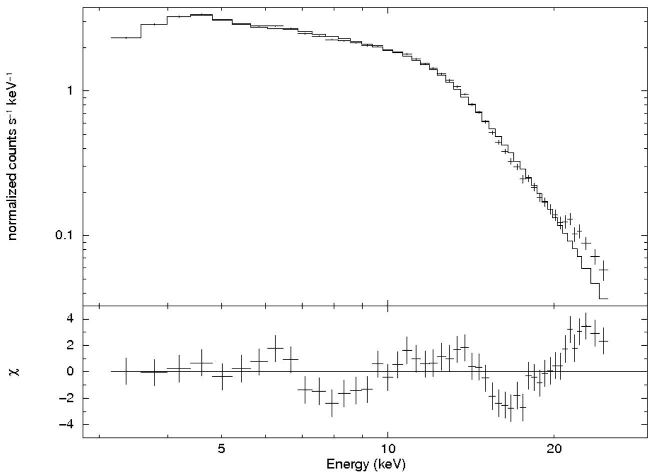

Figure 5.2: Overall *RXTE - PCA* spectrum of 4U 1907+09 fitted with a simple PL, an exponential cutoff and photoelectric absorption. The upper panel shows the data and the model. The lower panel shows the residuals of the fit. Deviation of the residuals around ~20 keV and ~7 keV are clear (Red. χ^2 = 2.79).

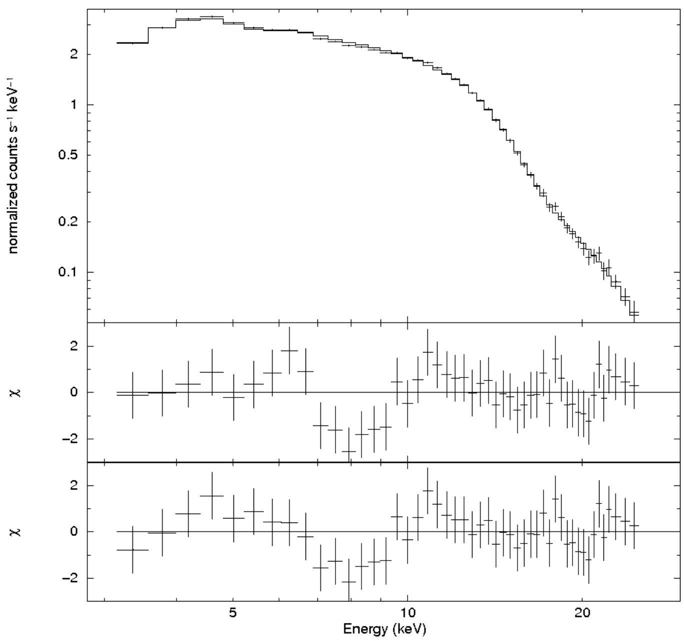

Figure 5.3: The best fit of the overall *RXTE - PCA* spectrum of 4U 1907+09 with the composite PL models. The upper panel shows the data and the model. The middle panel shows the residuals after the addition of the model component 'cyclabs' (Red. χ^2 = 1.07). The bottom panel shows the residuals of the further modeling with a Gaussian fixed at 6.4 keV (Red. χ^2 = 0.93).

found by Pottschmidt et al. (2007). The best fit of the composite PL model is presented in Figure 5.3 and corresponding parameters are given in Table 5.1.

As it can be seen in Figure 5.3, even for the best fit model there exists a deviation of residuals around ~7 - 9 keV. This feature was realized previously by Coburn et al. (2002). They were first tempted to associate the feature with a CRSF at ~9 keV, making the ~18 keV CRSF the second harmonic. However, they found that the feature is too broad to be a line since it modifies the continuum over a large energy range. Furthermore, 10 sources in the sample of Coburn et al. (2002) all showing a wiggle in the range 8 - 12 keV, led them to propose that the feature is inherent in accretion powered pulsar spectra.

The NPEX model introduced in section 5.1 is capable of modeling the slightly concave feature around ~7 - 9 keV, since the two component power law model can replicate the broad modification of the continuum. As a result, the overall

Table 5.1: Best fit parameters for the composite PL models. All uncertainties are calculated at 90% confidence level.

Parameter	PL * cyclabs	PL * cyclabs + Gaussian
n_{H} (10^{22} cm^{-2})	$3.44^{+0.76}_{-0.75}$	$2.56^{+0.95}_{-0.95}$
PL Photon index	$1.16^{+0.05}_{-0.06}$	$1.10^{+0.07}_{-0.06}$
PL Norm. (10^{-2} cts cm^{-2} s^{-1})	$2.33^{+0.29}_{-0.27}$	$2.01^{+0.34}_{-0.29}$
E_{cut} (keV)	$12.71^{+0.51}_{-0.41}$	$12.73^{+0.44}_{-0.48}$
E_{fold} (keV)	$10.00^{+1.31}_{-1.06}$	$9.37^{+1.25}_{-1.02}$
E_{Fe} (keV)	-	6.4 (Frozen)
σ_{Fe} (eV)	-	70 (Frozen)
Fe Norm. (10^{-4} cts cm^{-2} s^{-1})	-	$1.71^{+1.18}_{-0.20}$
E_{cyc} (keV)	$17.03^{+0.38}_{-0.44}$	$17.00^{+0.41}_{-0.29}$
τ_{cyc}	$0.41^{+0.09}_{-0.09}$	$0.42^{+0.09}_{-0.09}$
σ_{cyc} (keV)	$2.25^{+0.77}_{-0.73}$	$2.38^{+0.35}_{-0.81}$
Unabsorbed flux at 3 - 25 keV (10^{-10} erg cm^{-2} s^{-1})	$3.99^{+0.01}_{-0.05}$	$3.92^{+0.01}_{-0.06}$
Reduced χ^2	1.07 (41 d.o.f.)	0.93 (40 d.o.f.)

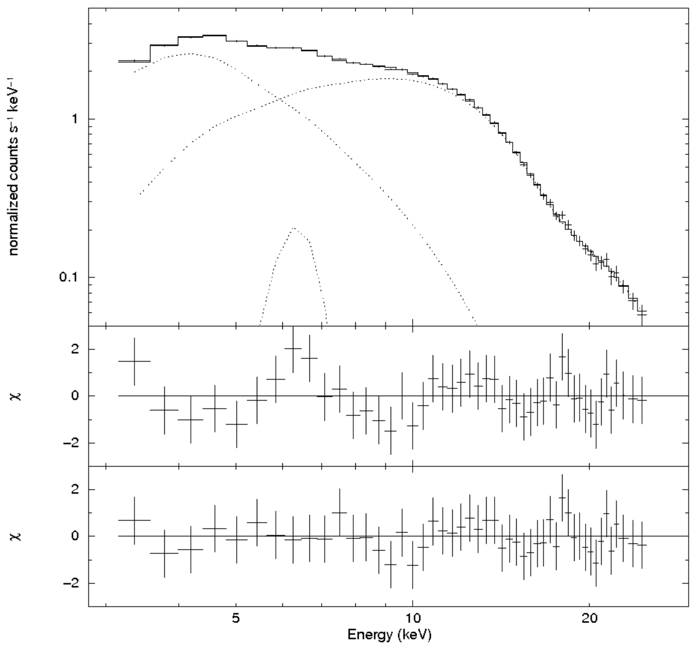

Figure 5.4: The best fit of the overall *RXTE - PCA* spectrum of 4U 1907+09 with the composite NPEX models. The upper panel shows the data, the model and additive model components (*dotted lines*). The middle panel shows the residuals after the addition of the model component 'cyclabs' (Red. χ^2 = 0.79). The bottom panel shows the residuals of the further modeling with a Gaussian fixed at 6.4 keV (Red. χ^2 = 0.47).

spectrum of 4U 1907+09 is secondly modeled with NPEX plus photoelectric absorption, cyclotron absorption and a Gaussian at 6.4 keV. The best fit of this model is presented in Figure 5.4 and corresponding parameters are given in Table 5.2.

The main difference between simple PL and NPEX modeling is the high n_{H} values found in NPEX modeling. Although there are a few bins to confine the photoelectric absorption in the 3 - 25 keV spectra, simple PL model is successful to better constrain the column density. The tentative measurements with NPEX model may be a reason of the two component modeling of the continuum. The negative power law component in NPEX is found steeper than it is found in the simple PL model. Consequently, more absorption is appointed in order to fit the model to the data. Moreover, e-folding energies found by NPEX modeling are about half of the values of simple PL modeling. This difference may be attributed to the dissimilar nature of the exponential cutoff components in these models. Cyclotron absorption line parameters of the two modeling are found similar within the error ranges. However the fundamental line energy is found to be around ~17 keV, which is less than the previously reported value ~18.8 keV (Cusumano et al. 1998) while the depth and width are agreeable. The shift of the line energy may be due to the averaging of the observations.

Nevertheless, all spectral parameters of NPEX modeling are consistent with the work of Mihara (1995) and Makishima et al. (1999) the fit is statistically artificial with reduced χ^2 values less than 1. Furthermore, the contour plots of simple PL model are rounder than NPEX model, which means the correlation of model parameters have lower degrees. Therefore the results of the simple PL fits are more reliable, since artificial correlations in NPEX cannot correctly reflect the physical nature of the parameters. The choice of the historical simple PL model is also more

Table 5.2: Best fit parameters for the composite NPEX models. All uncertainties are calculated at 90% confidence level.

Parameter	NPEX * cyclabs	NPEX * cyclabs + Gaussian
n_H (10^{22} cm^{-2})	$11.09^{+2.17}_{-1.98}$	$10.97^{+2.23}_{-1.15}$
PL Photon index (negative)	$2.01^{+0.38}_{-0.32}$	$2.20^{+0.45}_{-0.30}$
PL Norm. (10^{-1} cts cm^{-2} s^{-1})	$3.15^{+3.20}_{-1.44}$	$3.95^{+5.67}_{-0.21}$
PL Photon index (positive)	2.00 (Frozen)	2.00 (Frozen)
PL Norm. (10^{-4} cts cm^{-2} s^{-1})	$2.08^{+0.51}_{-0.50}$	$2.07^{+0.59}_{-0.44}$
E_{fold} (keV)	$3.89^{+0.45}_{-0.26}$	$3.95^{+0.28}_{-0.28}$
E_{Fe} (keV)	-	6.4 (Frozen)
σ_{Fe} (eV)	-	70 (Frozen)
Fe Norm. (10^{-4} cts cm^{-2} s^{-1})	-	$2.47^{+1.10}_{-1.10}$
E_{cyc} (keV)	$17.10^{+0.25}_{-0.21}$	$17.09^{+0.21}_{-0.29}$
τ_{cyc}	$0.70^{+0.18}_{-0.12}$	$0.74^{+0.19}_{-0.15}$
σ_{cyc} (keV)	$3.41^{+1.11}_{-0.77}$	$3.71^{+1.14}_{-0.94}$
Unabsorbed flux at 3 - 25 keV (10^{-10} erg cm^{-2} s^{-1})	$4.75^{+0.29}_{-0.63}$	$4.73^{+0.39}_{-0.58}$
Reduced χ^2	0.79 (41 d.o.f.)	0.47 (40 d.o.f.)

convenient, because a comparison with earlier results can be done in order to realize possible changes in the conditions of the source.

5.1.1.2 Orbital Phase Resolved Spectra

The processed *RXTE* observations allow the investigation of the variation in the spectral parameters through the binary orbit; since they spread over a variety of orbital phases (see Table 4.1). Therefore, 3 - 25 keV spectra of each non-dip observation are individually modeled in order to find the orbital variation in the parameters. Both simple PL and NPEX models are used to fit the individual spectra. Although constraining the cyclotron absorption parameters were possible, addition of a Gaussian component was unlikely since individual spectra do not have a good quality due to the short exposure times (~2 ks). The best fit plots and residual panels of two different models are given in Figure B.1 of Appendix B.

When the results of the simple PL and NPEX models were compared, it was seen that the errors of the parameters were enlarged in NPEX. Along with the reasons discussed at the end of the section 5.1.1.1, it is therefore found appropriate to use the simple PL parameters in order to search for orbital variations. Four sample parameter sets, corresponding to four observations with different orbital phases, are listed in Table 5.3. Best fit parameters of all 26 non-dip observations are plotted over observation mid-time in Figure 5.5.

Orbital variations of unabsorbed flux, column density and photon index are plotted in Figure 5.6. The results are very similar to the results of previous studies (see Figure 3.4 for comparison). The unabsorbed flux values varying between 1.7 - 7.7×10^{-10} erg cm^{-2} s^{-1}, approve that 4U 1907+09 is a variable X-ray source. When the first panel of Figure 5.6 is compared with the folded orbital profile of the source (see Figure 3.1) an analogous distribution is easily seen with the large primary maxima during periastron passage of the pulsar in its orbit around the companion star. The reason of this increase in flux is the increase in the mass accretion rate during periastron passage. As more mass interacts with the magnetic field of the pulsar, more X-ray photons are produced.

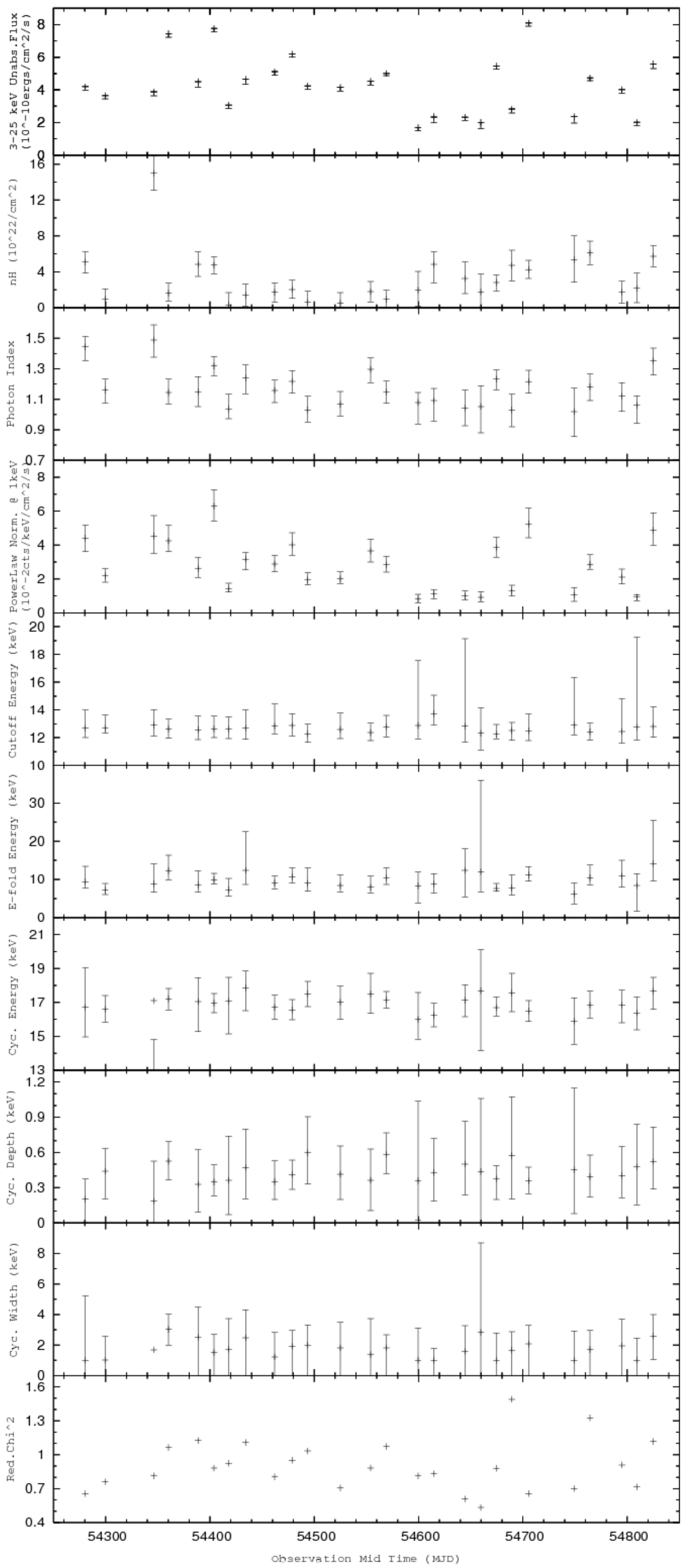

Figure 5.5: Best fit spectral parameters of 26 non-dip observations.

Orbital dependence of Hydrogen column density (n_H) is evident from the second panel of Figure 5.6. The base value of n_H is around ~2x10^{22} cm^{-2}. It increases up to a maximal value of ~5.7x10^{22} cm^{-2} just after the periastron passage and it remains at high values until the apastron, where it reduces to its base value again. The orbital variability of n_H is a probe to the density distribution of the accreting matter. The increase in the mass accretion rate during the periastron passage is followed by an increase in n_H, meaning that the density of the absorbing matter is enhanced. Preservation of the maximal absorption from periastron to apastron implies that the gas stream from the companion trails behind the pulsar until the apastron. Therefore, the orbital dependence of n_H approves that the location of the absorbing material is the accretion flow.

The orbital dependence of the power law photon index is less significant when compared to column density (see Figure 5.6). The photon index varies gradually (±0.2) around its mean value ~1.2, although there seems to be an increasing trend at periastron. The photon index is rather expected to be dependent

Table 5.3: Sample spectral parameters corresponding to four different orbital phases of 4U 1907+09. All uncertainties are calculated at 90% confidence level.

Observation ID	93036-01-29-00	93036-01-04-00	93036-01-16-00	93036-01-10-00
Obs. mid-time (MJD)	54674.61	54299.64	54478.76	54388.52
Orbital phase	0.05	0.28	0.67	0.89
n_H (10^{22} cm^{-2})	$2.94^{+0.91}_{-1.03}$	$1.08^{+1.21}_{-1.08}$	$2.09^{+1.06}_{-0.96}$	$5.02^{+1.39}_{-1.38}$
PL Photon index	$1.24^{+0.07}_{-0.07}$	$1.16^{+0.08}_{-0.09}$	$1.22^{+0.08}_{-0.07}$	$1.15^{+0.10}_{-0.10}$
PL Norm. (10^{-2} cts cm^{-2} s^{-1})	$3.90^{+0.65}_{-0.59}$	$2.19^{+0.45}_{-0.39}$	$4.00^{+0.75}_{-0.60}$	$2.64^{+0.67}_{-0.53}$
E_{cut} (keV)	$12.26^{+0.82}_{-0.35}$	$12.74^{+1.01}_{-0.44}$	$12.88^{+0.90}_{-0.74}$	$12.61^{+0.98}_{-0.74}$
E_{fold} (keV)	$7.67^{+1.54}_{-0.78}$	$7.27^{+1.96}_{-1.26}$	$10.88^{+2.49}_{-1.73}$	$8.78^{+3.89}_{-2.19}$
E_{cyc} (keV)	$16.74^{+0.65}_{-0.59}$	$16.70^{+0.78}_{-0.76}$	$16.63^{+0.58}_{-0.58}$	$17.17^{+1.23}_{-1.66}$
τ_{cyc}	$0.41^{+0.13}_{-0.19}$	$0.47^{+0.23}_{-0.24}$	$0.43^{+0.13}_{-0.13}$	$0.37^{+0.30}_{-0.13}$
σ_{cyc} (keV)	$1.00^{+1.91}_{-1.00}$	$1.14^{+1.47}_{-1.14}$	$1.95^{+0.98}_{-0.95}$	$2.53^{+1.79}_{-2.53}$
Unabs. flux at 3 - 25 keV (10^{-10} erg cm^{-2} s^{-1})	$5.46^{+0.02}_{-0.21}$	$3.62^{+0.08}_{-0.14}$	$6.18^{+0.01}_{-0.18}$	$4.50^{+0.02}_{-0.22}$
Reduced χ^2 (41 d.o.f.)	0.86	0.79	0.99	1.16

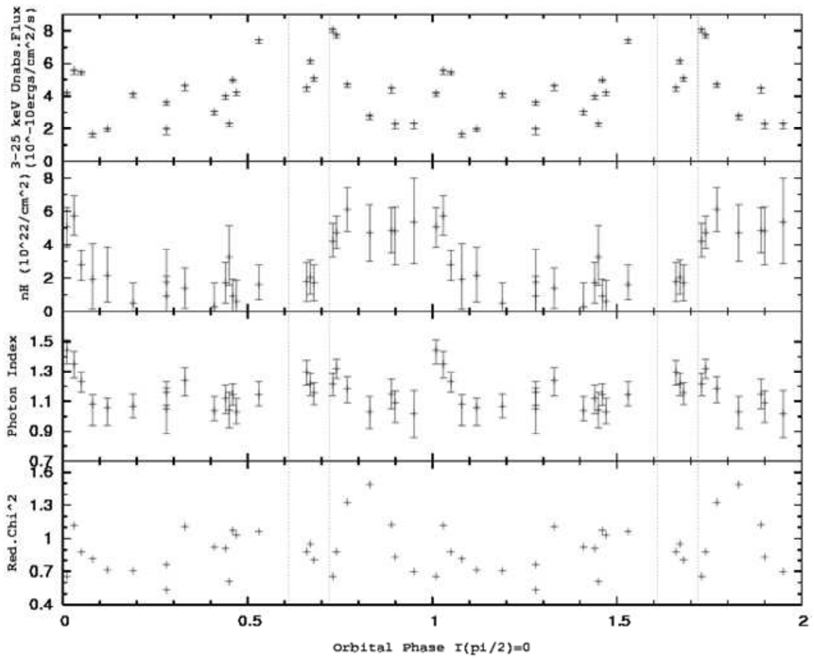

Figure 5.6: Variations of spectral parameters through binary orbit. The data points are repeated for a cycle for clarity. From top to bottom; unabsorbed flux at 3 - 25 keV, column density, photon index and reduced χ^2 are plotted over orbital phase respectively. The vertical dashed lines in all panels correspond to time of periastron passage within 68% confidence level.

on the flux, such that an increase in the periastron should be a consequence of the higher flux values. In order to search for the possible relation between the unabsorbed flux and photon index Figure 5.7 is plotted. In the upper panel of Figure 5.7 it is evident that the photon index slightly increases with increasing flux. This relation shows that the spectra of 4U 1907+09 softens during high flux episodes.

As it can be seen from the lower panel of Figure 5.7, the results show no correlation between column density and flux, which is contradicting. In fact, a reduction of opacity is expected due to an increase in ionization with increasing flux. This inconsistency may be arising from the variability of mass accretion rate. In order to search for a possible correlation, only the results of periastron observations may be used. However the number of observations with required orbital phase is only three, which is insufficient for a firm analysis.

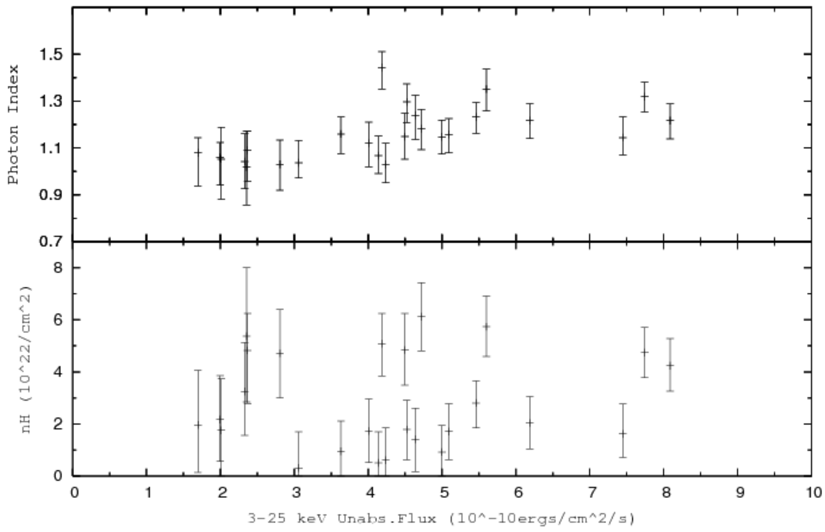

Figure 5.7: Variations of photon index (upper panel) and column density (lower panel) with flux. There is a slight increase in photon index with increasing flux, whereas no correlation is evident between column density and flux.

The orbital phase resolved spectroscopy shows that high energy cutoff and exponential folding energy are constant through the orbit, with the mean values ~12.7 keV and ~9.6 keV respectively. The CRSFs parameters are also found to be unchanging through the orbit. The cyclotron absorption line energy is found to be between ~15 keV and ~19 keV within 1σ error. The mean values of the depth and the width of the line are ~0.4 and ~1.7 keV respectively. These results are consistent with the previous studies of the source, although the estimated uncertainties are quite high (see Figure 5.5) due to the poor quality of individual *PCA* spectra with exposure time ~2 ks.

5.1.2 *INTEGRAL* Spectra

An overall *INTEGRAL* spectrum of 4U 1907+09 is analyzed by simultaneous fitting of the spectra generated from the data of the two detectors *JEM-X1* and *IBIS-ISGRI*. The total exposure times of 4 - 20 keV *JEM-X1* and 18 - 80 keV *IBIS-ISGRI* spectra are ~1860 ks and ~1230 ks respectively. Both composite PL and NPEX models are tried, as in the case of *RXTE - PCA* (see section 5.1.1.1). The constant

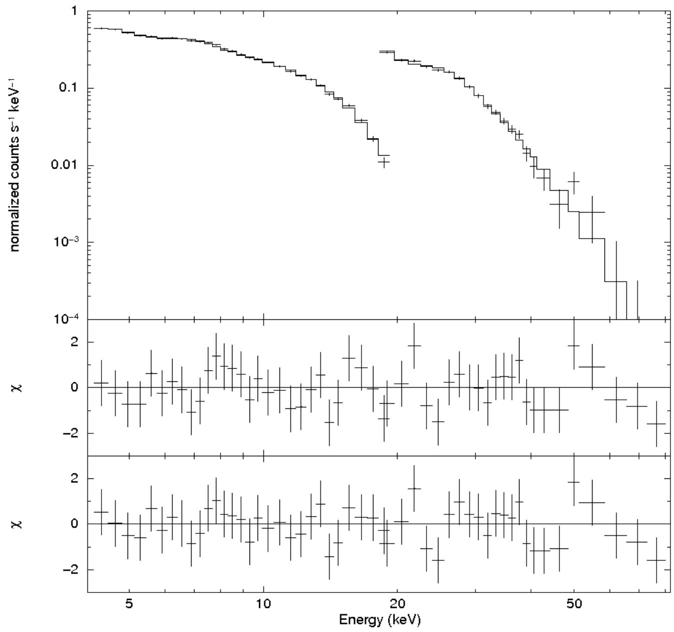

Figure 5.8: The best fit of the overall *INTEGRAL* spectrum of 4U 1907+09. The upper panel shows the data and the model. The middle panel shows the residuals of the composite PL model (Red. χ^2 = 0.97). The bottom panel shows the residuals of the composite NPEX model (Red. χ^2 = 0.87).

factor included to account for the normalization uncertainty between the two detectors, is found to be within the expected range, i.e. ~0.6 - 0.7 (Kirsch et al. 2005). The best fit plots are presented in Figure 5.8 and corresponding parameters are given in Table 5.4.

The energy range of the *INTEGRAL* spectrum is inappropriate to constrain the hydrogen absorption; however it was possible to find a limiting value for column density consistent with previous studies. The Fe emission line parameters are set to be fixed at values found by Fritz et al. (2006); the previous *INTEGRAL* study of the source spectrum. The line energy is observed to be shifted to ~7.1 keV due to instrumental aspects, similar to the results of the previous study.

As the broadband spectrum covers the required energy range for the analysis of CRSFs, an attempt is made to constrain both the fundamental line and the second harmonic parameters. The use of the model component ‘cyclabs’ was unsuccessful in finding the parameters of the second harmonic. In fact, this model tries to fit two

Lorentzian distribution functions (see Eqn. 2.46) corresponding to two harmonically spaced lines. Therefore, another attempt is made by using two Gaussian absorption components with independent energies (see Eqn. 2.47); however it was again not possible to constrain the second harmonic. Consequent analysis of the energy bins where the second harmonic should exist, showed that the SNR above 40 keV is low. The effort to increase the SNR by further rebinning the data was not useful either. Although the attempt to model the second harmonic at ~39.4 keV was unsuccessful, the parameters of the fundamental line at ~18.8 keV are found to be consistent in all

Table 5.4: Best fit parameters for the overall *INTEGRAL* spectrum. All uncertainties are calculated at 90% confidence level.

Parameter	PL	NPEX
Constant factor for *JEM-X*	$0.68^{+0.09}_{-0.08}$	$0.67^{+0.09}_{-0.08}$
Constant factor for *IBIS-ISGRI*	1.00 (Frozen)	1.00 (Frozen)
n_H (10^{22} cm^{-2})	2.74 (< 6.25)	0.00 (< 3.16)
PL Photon index (negative)	$1.97^{+0.17}_{-0.18}$	$0.63^{+0.25}_{-0.12}$
PL Norm. (10^{-1} cts cm^{-2} s^{-1})	$3.60^{+2.02}_{-1.23}$	$1.16^{+1.94}_{-0.97}$
PL Photon index (positive)	-	2.00 (Frozen)
PL Norm. (10^{-4} cts cm^{-2} s^{-1})	-	$1.27^{+0.85}_{-0.90}$
E_{cut} (keV)	$21.95^{+1.55}_{-1.59}$	-
E_{fold} (keV)	$6.67^{+0.82}_{-0.85}$	$4.18^{+0.32}_{-0.23}$
E_{Fe} (keV)	7.1 (Frozen)	7.1 (Frozen)
σ_{Fe} (eV)	0 (Frozen)	0 (Frozen)
Fe Norm. (10^{-4} cts cm^{-2} s^{-1})	$13.33^{+6.15}_{-6.00}$	$6.61^{+3.48}_{-3.60}$
E_{cyc} (keV)	$19.05^{+0.36}_{-0.35}$	$18.90^{+0.33}_{-0.33}$
τ_{cyc}	$1.66^{+0.23}_{-0.17}$	$1.46^{+0.56}_{-0.28}$
σ_{cyc} (keV)	$3.38^{+1.06}_{-0.69}$	$1.85^{+0.71}_{-0.33}$
Unabsorbed flux at 4 - 20 keV (10^{-10} erg cm^{-2} s^{-1})	$5.71^{+0.50}_{-0.75}$	$5.40^{+0.81}_{-1.73}$
Unabsorbed flux at 20 - 40 keV (10^{-11} erg cm^{-2} s^{-1})	$9.09^{+4.05}_{-4.29}$	$9.17^{+3.27}_{-7.18}$
Reduced χ^2	0.97 (54 d.o.f.)	0.87 (54 d.o.f)

tries. The results given in Figure 5.8 and Table 5.4 are obtained by setting the depth of the second harmonic to be zero.

The best fit values of high energy cutoff and e-folding energies found with composite PL model are a little different than the previous studies. For example, Cusumano et al. (1998) found both parameters as ~12 keV by using the regular exponential cutoff model (see Eqn. 2.41) to fit the broadband *BeppoSAX* spectrum. However, Fritz et al. (2006) used an improved model, called the Fermi - Dirac cutoff ('fdcut'; Tanaka 1986), to confine the cutoff parameters in the *INTEGRAL* spectrum and found the cutoff and e-folding energy to be $\sim 30^{+5}_{-8}$ and $\sim 7^{+3}_{-2}$ respectively. The 'fdcut' model defines the nature of the cutoff with a smooth function:

$$N(E) = N_{\mathrm{o}}\ E^{-\Gamma} \left[\ \exp\left(\frac{E - E_{\mathrm{cut}}}{E_{\mathrm{fold}}}\right) + 1\ \right]^{-1} \tag{5.2}$$

whereas the regular model suffers from the sudden break at $E = E_{\mathrm{cut}}$ (see Eqn. 2.41). Coburn et al. (2002) discussed that the 'fdcut' model reproduces pulsar continua more conveniently and that it gives similar results to the regular model. The regular cutoff model is used in fitting the spectrum of 4U 1907+09 and the best fit values of the parameters are within the error range of the results of Fritz et al. (2006). The difference between the *INTEGRAL* results and the previous results may be an instrumental effect.

In modeling the *INTEGRAL* spectrum, NPEX model is more satisfactory than PL model with less fluctuation in residuals and smaller error bars (see Figure 5.8 and Table 5.4), whereas the situation was the opposite in modeling the RXTE spectra (see section 5.1.1.1). The success of NPEX over a wide energy range is actually predicted by the creators of the NPEX model (Mihara 1995, Makishima et al. 1999). However, a meaningful comparison of the best fit parameters across the models is impossible because of the different functional forms. Hence, no physical conclusion can be done for the difference of the photon index values between the two models.

5.2 Pulse Timing Measurements

As recent pulse timing measurements of 4U 1907+09 (see Figure 3.3; Fritz et al. 2006) have revealed a torque reversal for the first time, further observations were necessary to determine the nature of the system. *RXTE*, with its high resolution timing, is an excellent mission appropriate for this type of research; therefore new measurements of pulse period with the observations given in Table 4.1 have the central importance at this study.

The technique used for the timing analysis of background subtracted non-dipping light curves was introduced in section 4.1.2 of the previous chapter. The pulse phase offsets calculated from cross-correlation analysis of template pulse profile with the average profiles from each ~2 ks long observation are plotted in Figure 5.9. In order to estimate the pulse frequency derivative, pulse phase results are first fitted to a quadratic polynomial, however the residuals of this fit showed a fluctuation such that there exists a second derivative. Therefore the cubic polynomial given by Eqn. 4.3 is used for a better fit. The results of the fit giving the timing solution of the source are presented in Table 5.5.

The pulse frequency derivative, calculated from a sequence of 25 pulse phases from the observations between June 2007 and August 2008, shows that 4U 1907+09 is spinning down with an average rate of 0.221 s yr^{-1}. This result

Table 5.5: Pulse timing solution of 4U 1907+09 from *RXTE* observations.

Parameter	Value
Epoch (MJD)	54467.6(1)
Spin frequency (ν)	2.266460(2)x10^{-3} Hz
Pulse Period (P)	441.2167(4) s
$\dot{\nu}$	− 3.59(2)x10^{-14} Hz s^{-1}
$\dot{P}$	6.99(4)x10^{-9} s s^{-1}
$\ddot{\nu}$	− 5.3(4)x10^{-22} Hz s^{-2}
$\ddot{P}$	1.03(8)x10^{-16} s s^{-2}
RMS Residuals (cubic)	0.048

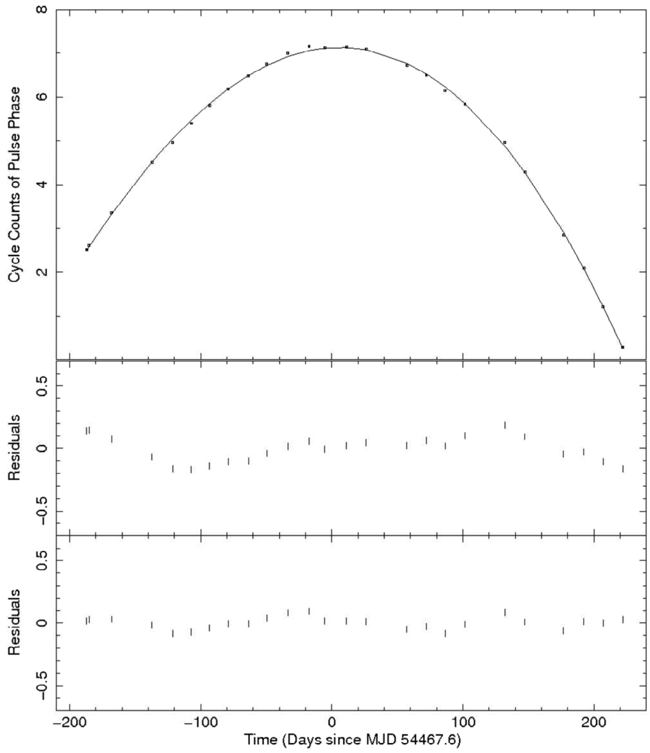

Figure 5.9: Cycle count plot of 4U 1907+09 with respect to the pulse period 441.2167 s. The upper panel shows the fit to the cubic polynomial given by Eqn. 4.3. The middle panel shows the residuals after the removal of quadratic polynomial. The lower panel shows the residuals after the removal of cubic polynomial.

implies that the source underwent a new torque reversal before June 2007, since the source was found to be spinning up in the previous timing study (Fritz et al. 2006). The new spin-down rate is close to the long term spin-down rate between August 1983 and September 1998 (Baykal et al. 2001). The existence of a negative second derivative of the pulse frequency denotes that the spin-down rate of the source is increasing with the acceleration of 0.1 s yr^{-2}.

In order to demonstrate the pulse period evolution of the source, 24 new pulse periods are estimated by calculating individual derivatives form each pair of pulse phases of Figure 5.9. Therefore, corresponding time of a measured pulse period is the mid-point of the employed pair. Pulse period measurements are presented in Table 5.6. Combining these results with the previous measurements given in Table 3.3,

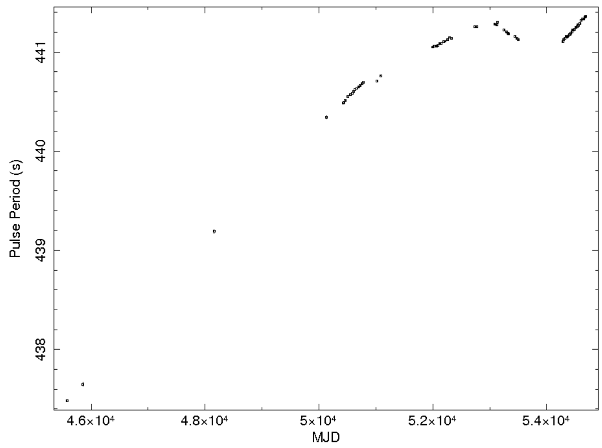

Figure 5.10: Updated pulse period history of 4U 1907+09. Recent spin-down trend of the source is evident between MJD 54281 and MJD 54682.

Table 5.6: Pulse period measurements of 4U 1907+09 from *RXTE* observations.

Date (MJD)	Pulse Period (s)	Date (MJD)	Pulse Period (s)
54281.5	441.1031±0.0372	54470.4	441.2185±0.0039
54291.0	441.1213±0.0038	54486.3	441.2284±0.0043
54315.0	441.1367±0.0021	54509.4	441.2472±0.0021
54338.3	441.1545±0.0041	54532.3	441.2538±0.0044
54353.3	441.1509±0.0046	54546.8	441.2756±0.0046
54367.3	441.1543±0.0047	54561.6	441.2657±0.0043
54381.3	441.1623±0.0046	54584.3	441.2855±0.0022
54396.2	441.1750±0.0042	54607.1	441.3195±0.0043
54410.9	441.1761±0.0047	54629.6	441.3301±0.0022
54426.0	441.1863±0.0041	54652.1	441.3307±0.0043
54442.1	441.1992±0.0040	54667.2	441.3549±0.0044
54456.1	441.2245±0.0055	54682.1	441.3596±0.0044

pulse period history of 4U 1907+09 is plotted in Figure 5.10, which is an updated version of Figure 3.3.

The pulse period evolution of 4U 1907+09 implying a recent torque reversal shows that the spin-up episode continued for a short time when compared to ~15 years-long spin-down episode. The reversal is a rare event for this source, in contrast to most wind-fed pulsars which commonly undergo alternating episodes of spin-up and spin-down (e.g. Vela X-1, Cen X-3). Decade-long distinct episodes, similar to 4U 1907+09, are also observed in systems such as 4U 1626-67 and GX 1+4 (Bildsten et al. 1997). Although torque reversal time-scales of the order of hours to days have been simulated for wind-fed pulsars (Börner et al. 1987, Blondin et al. 1990, Murray et al. 1999), it is difficult to explain time-scales of the order of years with simple accretion torque models.

According to Ghosh & Lamb (1979) model discussed in chapter 2, a net negative torque resulting in a spin-down may arise either from an increase in magnetic field or decrease in mass accretion rate. However such changes in the system should be accompanied with changes in the X-ray flux and spectral characteristics. 4U 1907+09 is rather a challenging example; because no significant flux or spectral variations related to the changes in the spin rate, have been observed (Baykal et al. 2001, 2006; Fritz et al. 2006). Moreover; the spin rates of opposite sign are nearly equal in magnitude, requiring step function-like changes in mass accretion rate which is implausible.

Recent models constructed with the need of a physical explanation to torque reversals are reviewed in section 2.3.3 of the second chapter. Models considering retrograde disks (Makishima et al. 1988, Nelson et al. 1997, Murray et al. 1999), warping and precessing disks (Van Kerkwijk et al. 1998) and angular velocity transitions in the disk (Yi et al. 1997, Yi & Wheeler 1998) also require changes in the X-ray flux and spectral characteristics, therefore they cannot be applied for 4U 1907+09. Models considering the magnetic interactions between the disk and the magnetosphere (Torkelsson 1998, Lovelace et al. 1999, Locsei & Melatos 2004) often try to explain repeated chaotic transitions between spin-up and spin-down, which may not be the case of 4U 1907+07.

The only available model that explains torque reversal episodes without a change in the mass accretion rate (i.e. a change in the flux) is the model of Perna et al. (2006). As discussed in section 2.3.3 of the second chapter; the configuration of this model leads to an asymmetric magnetospheric boundary and solutions show that different regions occur in the disk, such that the propeller effect is locally at work in some regions, while accretion from other regions is possible. This model have been applied to the torque reversals of GX 1+4 and 4U 1626-67 and have given plausible results, so one may conclude that it would also work for the torque reversal of 4U 1907+09 (Fritz et al. 2006). However, the model of Perna et al. (2006) is proposed for persistent prograde accretion discs; whereas the nature of the accretion disc in 4U 1907+09 is of transient nature given that the source shows occasional intensity dips and flares (in't Zand et al. 1997), where QPOs are observed as an indication of formation of a disk during flaring episodes (in't Zand et al. 1998, Mukerjee et al. 2001). Furthermore, this toy model needs to be improved by involving other torque terms such as magnetic and viscous stresses.

More detailed theoretical studies are required to explain the behavior of 4U 1907+07 for the reasons discussed above. Another requirement, for better identification of the nature of the source, is further monitoring. As one can see from Figure 5.10, there is a ~2 years-long gap between the previous study and the *RXTE* results of this work. In fact, *INTEGRAL* observations given in Table 4.3 are selected to cover this gap in the pulse timing measurements. Although, the timing analysis of *INTEGRAL* observations is a future work, preliminary results show that the torque was in an unstable condition undergoing repeated transitions during this time interval (Şahiner et al. 2010).

5.3 Pulse Profiles

The pulse profile of a pulsar is a probe to the emission mechanism, since the X-ray emission arises from the accretion column. Once the pulse period of 4U 1907+09 is measured, a consequent study of the pulse profile can be done. The pulse period given in the timing solution (see Table 5.5) corresponds to the mid-time of all *RXTE* observations. In order to reveal the time averaged pulse profile of the

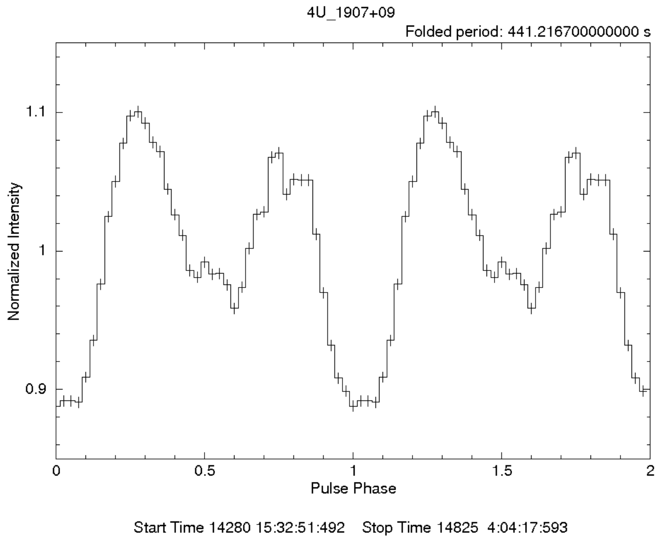

Figure 5.11: Average pulse profile of 4U 1907+09 generated by folding *RXTE - PCA* light curve on the period 441.2167 s. Number of bins is 40.

source, *RXTE - PCA* light curve, created with no energy channel selection, is folded on the period 441.2167 s (see Figure 5.11). Resultant profile has a double peak sinusoidal shape, which indicates that the two hot spots emit comparable number of photons in average.

As a previous study of energy resolved pulse profiles of 4U 1907+09 has shown that the pulse shape changes above 20 keV with one peak disappearing (in't Zand et al. 1998), pulse profiles in three energy bands, i.e. 3 - 10 keV, 10 - 20 keV and 20 - 40 keV are constructed from *RXTE - PCA* light curves (see Figure 5.12), to be able to compare the results with Figure 3.2. The results show that the pulse profile is similar in the first two energy bands, whereas the leading peak significantly loses its intensity in 20 - 40 keV. This result is same as in't Zand et al. (1998), therefore the nature of the source has not changed in time. The implication of this dependence is an asymmetry in the X-ray production at the two poles such that the high energy emission arises only from one hot spot.

Since INTEGRAL is a high energy mission, INREGRAL observations can reveal the nature of the pulse profile in high energies better. The 20 - 40 keV pulse profile generated from the *INTEGRAL IBIS-ISGRI* light curve is given in Figure 5.13 and shows the single peak shape sharper than *RXTE*; therefore confirms the energy

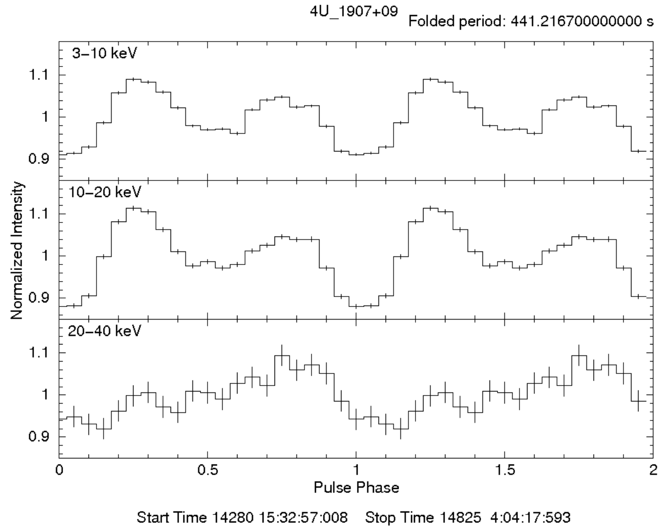

Figure 5.12: Energy resolved pulse profiles of 4U 1907+09 by folding on the period 441.2167 s. Number of bins is 20. The energy bands (3 - 10 keV, 10 - 20 keV and 20 - 40 keV) related to the panels are given at the top left of each panel.

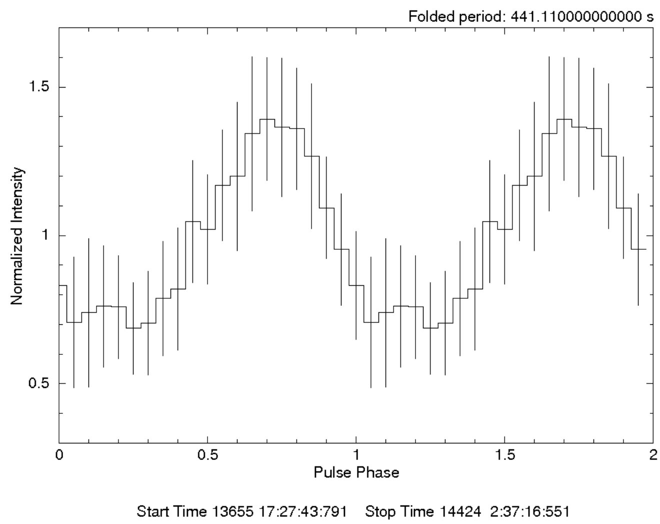

Figure 5.13: 20 - 40 keV pulse profile of 4U 1907+09 generated from *INTEGRAL - IBIS-ISGRI* observations. Number of bins is 20. Folded period is given at top right of the plot.

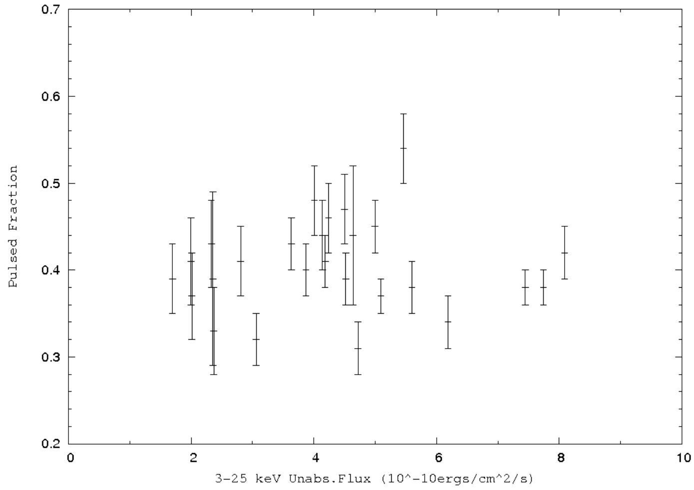

Figure 5.14: Pulsed fraction of individual non-dipping *RXTE* observations versus unabsorbed flux at 3- 25 keV plot shows that pulsed fraction varies independently.

dependence of the pulse profile. This nature of the source is also confirmed in the previous *INTEGRAL* study, as the energy resolved pulse profiles between 15 - 60 keV have shown single peak profiles (Fritz et al. 2006).

Further analysis of pulse profile is done by constructing energy resolved pulse profiles of each non-dipping *RXTE* observation, in order to see if there is a difference in the scenario due to luminosity changes. The plots related to this analysis are presented in Figure A.1 of Appendix A. Pulsed fractions of the observations calculated from energy averaged pulse profiles are listed in Table 4.1, in addition it is confirmed that the pulsed fraction remain the same in all energy bands. The pulsed fraction values show variability between 30% and 50%, in contrast to the results of Mukerjee et al. (2001) who have reported almost constant pulsed fraction (~30%). Pulsed fraction values are plotted over the unabsorbed flux values found in orbital phase resolved spectroscopy, with the purpose of finding a positive relation (see Figure 5.14); however pulse fraction seems to be varying independently.

The pulse profiles in Figure A.1 of Appendix A are very similar to the averaged profiles, although there are small variations in the shape on different days. Both 3 - 10 keV and 10 - 20 keV pulse profiles always have double peak sinusoidal shapes. However the relative intensities of the peaks are variable within days, as it has been reported by Mukerjee et al. (2001). For example; the intensity of the primary peak is larger in the observation 93036-01-04-00, secondary peak is larger in the observation 93036-01-37-00 and the peaks are equal in the observation 93036-01-10-00. No exchange of the larger peak is observed in the different energy bands. Furthermore; the cavity between the two peaks in phase 0.5 sometimes becomes shallower in the energy band 3 - 10 keV (e.g. 93036-01-08-00, 93036-01-12-00), whereas it becomes a sharp minimum occasionally (e.g. 93036-01-25-00).

The high energy pulse profile (20 - 40 keV) is also found to be variable within observations. In most of the observations 20 - 40 keV profile is single peaked, although a small hump is evident in a considerable amount of observations (~9 obs.). The existence of the hump is not correlated with the relative intensity of the peak in lower energy bands. The individual high energy profiles also confirm that the hard X-ray emission from one pole is weaker than the other, as it is found in the averaged profiles.

A detailed analysis of the 20 - 40 keV pulse profiles reveals that the trailing edge of the remaining single peak is shifted ~0.2 in phase relative to the lower energy bands in about half of the observations (e.g. 93036-01-08-00, 93036-01-13-00). This phase shift corresponds to a shift of ~70° in the angle of the pulse beam. As discussed in section 2.4 of the second chapter, there are two beam shapes (pencil and fan) depending on the direction of the emitted radiation. A pencil beam is along the magnetic axis, whereas a fan beam is perpendicular. Although an exchange of the beam shape is related to the luminosity of the source, there are examples (e.g. 4U 1626-67, Her X-1) in which pulse phase reversals between different energy bands are observed and explained by a exchange in the beam shape from pencil to fan (White et al. 1983 and references therein). The pulse shifts of these sources are about ~180°, therefore the shift in the pulse of 4U 1907+09 low when compared to these sources. A modest assertion for the reason of the ~70° shift would be an increased scattering of hard X-ray photons, since pulse modeling is beyond the scope of this thesis.

CHAPTER 6

SUMMARY AND CONCLUSIONS

In this thesis, *RXTE* (39 obs.) and *INTEGRAL* (611 SCWs) observations of 4U 1907+09 spread over ~38 months time interval with a total of ~2000 ks exposure time were extensively analyzed. The plentiful characteristics of 4U 1907+09, has made it possible to test numerous theoretical and observational subjects about accretion powered pulsars such as; accretion mechanisms, accretion torques, X-ray spectral evolution, pulse period evolution, and variation of pulse profile geometry.

The results of energy spectra of *RXTE* and *INTEGRAL* observations have shown that 4U 1907+09 shelters all spectral features attributed to accretion powered pulsars. A simple power law with an exponential cutoff at ~13 keV modified by photoelectric absorption, ~6.4 keV Fe Kα emission and ~18.9 keV CRSF successfully modeled the time-averaged spectra giving consistent results with the previous studies. On the other hand, orbital phase resolved spectroscopy has revealed the highly variable nature of the absorption. The increase of Hydrogen column density just after the periastron and the preservation of the maximal value until apastron have supported the idea that the absorbing material arises from the accretion flow. The increase in X-ray flux due to increased mass accretion rate during periastron passage is also accompanied with a slight spectral softening. Although the attempt to model the second harmonic CRSF at ~39.4 keV was unsuccessful during the spectral fits of *INTEGRAL* spectra; it does not mean that the feature is extinct since the SNR of the spectral bins corresponding to the required energies were low. The parameters of the fundamental CRSF were indeed found to be consistent with the previous results. Another failure was perceived in constraining the Fe line parameters; however the main reason of this was the insensitivity of the instruments. Therefore it is concluded that the source should be observed with high resolution spectroscopic instruments like *XMM-Newton* for a better identification of the line.

The pulse timing measurements done by analyzing *RXTE* observations have revealed a new spin-down episode of 4U 1907+09, which implies that a torque reversal should have occurred before June 2007, since the source was found to be spinning up in the previous timing study. The spin-up interval has taken a short time when compared to the ~15 years-long steady spin-down episode. The dominance of the spin-down episodes may indicate the presence of a retrograde disk or centrifugal inhibition of accretion. Since the source has not yet shown significant changes in the X-ray flux and/or spectral characteristic accompanied with the torque reversals, an exchange of retrograde to prograde disk scenario is unlikely. A propeller mechanism may be responsible for the spin-down episodes as the source undergoes occasional dipping states regularly, in which the count rates are below the detection threshold. Therefore dipping states are candidates of sufficiently low accretion rates such that the accreting material cannot squeeze the magnetosphere resulting in a co-rotation radius much smaller than the magnetospheric radius. Another possible scenario is mentioned in the new model of Perna et al. (2006), in which an asymmetric magnetospheric boundary leads to a dual disk characteristic such that the propeller effect is locally at work in some regions whereas accretion from other regions is possible. Although this model suffers from its ordinary assumptions, it explains the torque reversals without the need of a significant change in the mass accretion rate.

The final analysis of *RXTE* observations contains the measurements of new pulse periods for 4U 1907+09 and search for the possible luminosity and energy dependence of the pulse profile. The pulsed fractions of individual observations have been found to be variable within the range 30 - 50%. Although no luminosity correlation could be found, the energy dependence is evident. The double peak sinusoidal shape of the profile reduces to single peak above 20 keV, which implies that the hard x-ray production arises only from one polar cap. The relative intensities of the two peaks have been confirmed to be varying within different observations. Furthermore in about half of the high energy profiles, the angle of the pulse beam seems to be shifted (~70°) with respect to lower energies. Even if similar energy dependent shifts in other sources had been explained by an exchange of the beam shape from pencil to fan, a modest claim would be an increased scattering of hard X-ray photons.

REFERENCES

[1] Alpar, M. A. and Shaham, J. 1985, Nature, 316, 239

[2] Angelini, L., Stella, L. and Parmar, A. N. 1989, ApJ, 346, 906

[3] Anzer, U., Börner, G. and Monaghan, J. J. 1987, A&A, 176, 235

[4] Apparao, K. M. V. 1994, SSRv, 69, 255

[5] Arons, J. and Lea, S. M. 1976, ApJ, 207, 914

[6] Baade, W. and Zwicky, F. 1934, PhRv, 46, 76

[7] Basko, M. M. and Sunyaev, R. A. 1976, MNRAS, 175, 395

[8] Baykal, A. 2005, in Baykal, A., Yerli, S. K., Inam, S. Ç. and Grebenev, S., The Electromagnetic Spectrum of Neutron Stars, p.263, Springer, Dordrecht

[9] Baykal, A., İnam, S. Ç., Alpar, M. A., et al. 2001, MNRAS, 327, 1269

[10] Baykal, A., İnam, S. Ç. and Beklen, E. 2006, MNRAS, 369, 1760

[11] Bildsten, L., Chakrabarty, D., Chiu, J. et al. 1997, ApJS, 113, 367

[12] Blondin, J. M., Kallman, T. R., Fryxell, B. A. and Taam, R. E. 1990, ApJ, 356, 591

[13] Börner, G., Hayakawa, S., Nagase, F. and Anzer, U. 1987, A&A, 182, 63

[14] Chakrabarty, D., Bildsten, L., Finger, M. H. et al. 1997a, ApJ, 481, L101

[15] Chakrabarty, D., Bildsten, L., Grunsfeld, J. M. et al. 1997b, ApJ, 474, 414

[16] Chitnis, V. R., Rao, A. R., Agrawal, P. C. and Manchanda, R. K. 1993, A&A, 268, 609

[17] Coburn, W., Heindl, W. A., Rothschild, R. E. et al. 2002, ApJ, 580, 394

[18] Cook, M. C. and Page, C. G. 1987, MNRAS, 225, 381

[19] Corbet, R. H. D. 1984, A&A, 141, 91

[20] Corbet, R. H. D. 1986, MNRAS, 220, 1047

[21] Cox, N. L. J., Kaper, L. and Mokiem, M. R. 2005a, A&A, 436, 661

[22] Cox, N. L. J., Kaper, L., Foing, B. H. and Ehrenfreund, P. 2005b, A&A, 438, 187

[23] Cusumano, G., di Salvo, T., Burderi, L. et al. 1998, A&A, 338, L79

[24] Davidson, K. and Ostriker, J. P. 1973, ApJ, 179, 585

[25] Deeter, J. E. and Boynton P. E. 1985, in Hayakawa, S. and Nagase, F., Proc. Inuyama Workshop: Timing Studies of X-Ray Sources, p.29, Nagoya Univ., Nagoya

[26] Elsner, R. F. and Lamb, F. K. 1977, ApJ, 215, 897

[27] Finger, M. H. 1999, in 4th HEAD Meeting, 15.06 Bulletin of the American Astronomical Society, Vol.31, p.712

[28] Finger, M. H., Wilson, R. B. and Harmon, B. A. 1996, ApJ, 459, 288

[29] Fortner, B., Lamb, F. K. and Miller, G. S. 1989, Nature, 342, 775

[30] Frank, J., King, A. and Raine, D. J. 2002, Accretion Power in Astrophysics: Third Edition, Cambridge University Press, Cambridge

[31] Fritz, S., Kreykenbohm, I., Wilms, J. et al. 2006, A&A, 458, 885

[32] Giacconi, R., Gursky, H., Paolini, F. R. and Rossi, B. B. 1962, PhRvL, 9, 439

[33] Giacconi, R., Kellogg, E., Gorenstein, P. et al. 1971a, ApJ, 165, L27

[34] Giacconi, R., Gursky, H., Kellogg, E. et al. 1971b, ApJ, 167, L67

[35] Ghosh, P., Pethick, C. J. and Lamb, F. K. 1977, ApJ, 217, 578

[36] Ghosh, P. 1998, AdSpR, 22, 1017

[37] Ghosh, P. 2007, Rotation and Accretion Powered Pulsars, World Scientific Publishing Co., Pte. Ltd., Singapore

[38] Ghosh, P. and Lamb, F. K. 1978, ApJ, 223L, 83

[39] Ghosh, P. and Lamb, F. K. 1979a, ApJ, 232, 259

[40] Ghosh, P. and Lamb, F. K. 1979b, ApJ, 234, 296

[41] Ghosh, P. and Lamb, F. K. 1991, in Ventura, J. and Pines, D., Neutron Stars: Theory and Observation, p.363, Dordrecht, Kluwer

[42] Goldwurm, A., David, P., Foschini, L. et al. 2003, A&A, 411, L223

[43] Haberl, F., White, N. E. and Kallman, T. R. 1989, ApJ, 343, 409

[44] Haberl, F. and White, N. E. 1990, ApJ, 361, 225

[45] Ho, C. 1988, MNRAS, 232, 91

[46] Hoyle, F. and Lyttleton, R. A. 1939, PCPS, 34, 405

[47] Illarionov, A. F. and Sunyaev, R. A. 1975, A&A, 39, 185

[48] İnam, S. Ç., Şahiner, Ş. and Baykal, A. 2009, MNRAS, 395, 1015

[49] in't Zand, J. J. M., Strohmayer, T. E. and Baykal, A. 1997, ApJ, 479, L47

[50] in't Zand, J. J. M., Baykal, A. and Strohmayer, T. E. 1998, ApJ, 496, 386

[51] Iye, M. 1986, PASJ, 38, 463

[52] Jahoda, K., Swank, J. H., Giles, A. B. et al. 1996, Proc. SPIE, 2808, 59

[53] Jernigan, J. G., Klein, R. I. and Arons, J. 2000, ApJ, 530, 875

[54] Kirsch, M. G., Briel, U. G., Burrows, D. et al. 2005, SPIE, 5898, 22

[55] Klein, R. I., Arons, J., Jernigan, G. and Hsu, J. 1996, ApJ, 457, L85

[56] Kommers, J. M., Chakrabarty, D. and Lewin, W. H. G. 1998, ApJ, 497, L33

[57] Lamb, F. K. 1989, in Ögelman, H., van den Heuvel, E. P. J., Timing Neutron Stars, p.649, Dordrecht, Kluwer

[58] Lamb, F. K. 1988, AdSpR, 8, 421

[59] Lamb, F. K., Pethick, C. J. and Pines, D. 1973, ApJ, 184, 271

[60] Lamb, F. K., Pines, D. and Shaham, J. 1978a, ApJ, 224, 969

[61] Lamb, F. K., Pines, D. and Shaham, J. 1978b, ApJ, 225, 582

[62] Laycock, S., Corbet, R. H. D., Coe, M. J. et al. 2005, ApJS, 161, 96

[63] Leahy, D. A. 1991, MNRAS, 251, 203

[64] Leahy, D. A. 2001, Proc. 27th International Cosmic Ray Conference, p.2528, Copernicus Gesellschaft, Hamburg

[65] Leahy, D. A., Darbro, W., Elsner, R. F. et al. 1983, ApJ, 266, 160

[66] Leahy, D. A., Matsuoka, M., Kawai, N. and Makino, F. 1989, MNRAS, 236, 603

[67] Lebrun, F., Leray, J. P., Lavocat, P. et al. 2003, A&A, 411, L141

[68] Levine, A. M., Bradt, H., Cui, W. et al. 1996, ApJ, 469, L33

[69] Locsei, J. T. and Melatos, A. 2004, MNRAS, 354, 591

[70] Lovelace, R. V. E., Romanova, M. M. and Bisnovatyi-Kogan, G. S. 1999, ApJ, 514, 368

[71] Lund, N., Budtz-Jørgensen, C., Westergaard, N. J. et al. 2003, A&A, 411, L231

[72] Makishima, K., Kawai, N., Koyama, K. and Shibazaki, N. 1984, PASJ, 36, 679

[73] Makishima, K., Ohashi, T., Sakao, T. et al. 1988, Nature, 333, 746

[74] Makishima, K., Ohashi, T., Kawai, N. et al. 1990, PASJ, 42, 295

[75] Makishima, K. and Mihara, T. 1992, in Tanaka Y. and Koyama K., Proc. 28th Yamada Conf.: Frontiers of X-ray Astronomy, p.23, UniversalAcademy Press, Tokyo

[76] Makishima, K., Mihara, T., Nagase, F. and Tanaka, Y. 1999, ApJ, 525, 978

[77] Marshall, N. and Ricketts, M. J. 1980, MNRAS, 193, P7

[78] Markert, T. H., Laird, F. N., Clark, G. W. et al. 1979, ApJS, 39, 573

[79] Mas-Hesse, J. M., Giménez, A., Culhane, J. L. et al. 2003, A&A, 411, L261

[80] Matsuda, T., Inoue, M. and Sawada, K. 1987, MNRAS, 226, 785

[81] McCray, R. A., Shull, J. M., Boynton, P. E. et al. 1982, ApJ, 262, 301

[82] Meszaros, P. 1992, High-Energy Radiation from Magnetized Neutron Stars, Univ. Chicago Press, Chicago

[83] Meszaros, P., Nagel, W. and Ventura, J. 1980, ApJ, 238, 1066

[84] Miceli, M., Decourchelle, A., Ballet, J. et al. 2006, A&A, 453, 567

[85] Mihara, T. 1995, PhD thesis, RIKEN, Tokyo

[86] Mihara, T., Makishima, K., Ohashi, T. et al. 1990, Nature, 346, 250

[87] Motch, C., Stella, L., Janot-Pacheco, E. and Mouchet, M. 1991, ApJ, 369, 490

[88] Mukerjee, K., Agrawal, P. C., Paul, B. et al. 2001, ApJ, 548, 368

[89] Murray, J. R., de Kool, M. and Li, J. 1999, ApJ, 515, 738

[90] Nagase, F. 1989, PASJ, 41, 1

[91] Nagel, W. 1981a, ApJ, 251, 278

[92] Nagel, W. 1981b, ApJ, 251, 288

[93] Nelson, R. W., Bildsten, L., Chakrabarty, D. et al. 1997, ApJ, 488, L117

[94] Nespoli, E., Fabregat, J. and Mennickent, R. E. 2008, A&A, 486, 911

[95] Ohashi, T., Inoue, H., Koyama, K. et al. 1984, PASJ, 36, 699

[96] Parmar, A. N., White, N. E. and Stella, L. 1989, ApJ, 338, 373

[97] Perna, R., Bozzo, E. and Stella, L. 2006, ApJ, 639, 363

[98] Pottschmidt, K., Wilms, J., Fritz, S. et al. 2007, in 211th AAS Meeting, 03.01 Bulletin of the American Astronomical Society, Vol.39, p.723

[99] Pringle, J. E. 1996, MNRAS, 281, 357

[100] Pringle, J. E. and Rees, M. J. 1972, A&A, 21, 1

[101] Roberts, M. S. E., Michelson, P. F., Leahy, D. A. et al. 2001, ApJ, 555, 967

[102] Rothschild, R. E., Blanco, P. R., Gruber, D. E. et al. 1998, ApJ, 496, 538

[103] Schwartz, D. A., Griffiths, R. E., Thorstensen, J. R. et al. 1980, AJ, 85, 549

[104] Seward, F. D., Page, C. G., Turner, M. J. L. and Pounds, K. A. 1976, MNRAS, 175, P39

[105] Shakura, N. I. and Sunyaev, R. A. 1973, A&A, 24, 337

[106] Shapiro, S. L. and Lightman, A. P. 1976, ApJ, 204, 555

[107] Shklovskii, I. S. 1967, ApJ, 148, L1

[108] Slettebak, A. 1988, PASP, 100, 770

[109] Stella, L., White, N. E. and Rosner, R. 1986, ApJ, 308, 669

[110] Şahiner, Ş., İnam S. Ç. and Baykal, A. 2010, in preparation

[111] Tanaka, Y. 1986, in Mihalas, D. and Winkler, K. H., Radiation Hydrodynamics in Stars and Compact Objects, p.198, Springer, Berlin

[112] Tananbaum, H., Gursky, H., Kellogg, E. M. et al. 1972, ApJ, 174, L143

[113] Torkelsson, U. 1998, MNRAS, 298, L55

[114] Trümper, J., Pietsch, W., Reppin, C. et al. 1978, ApJ, 219, L105

[115] Ubertini, P., Lebrun, F., Di Cocco, G. et al. 2003, A&A, 411, L131

[116] Valinia, A. and Marshall, F. E. 1998, ApJ, 505, 134

[117] van der Klis, M., Stella, L., White, N. et al. 1987, ApJ, 316, 411

[118] van der Klis, M. 2006, in Lewin, W. and van der Klis, M., Compact stellar X-ray sources, p.39, Cambridge University Press, Cambridge

[119] van Kerkwijk, M. H., van Oijen, J. G. J. and van den Heuvel, E. P. J. 1989, A&A, 209, 173

[120] van Kerkwijk, M. H., Chakrabarty, D., Pringle, J. E. and Wijers, R. A. M. J. 1998, ApJ, 499, L27

[121] Vedrenne, G., Roques, J. P., Schönfelder, V. et al. 2003, A&A, 411, L63

[122] Wang, Y. M. 1981, A&A, 102, 36

[123] Wang, Y. M. and Welter, G. L. 1981, A&A, 102, 97

[124] Waters, L. B. F. M. and van Kerkwijk, M. H. 1989, A&A, 223, 196

[125] White, N. E., Swank, J. H. and Holt, S. S. 1983, ApJ, 270, 711

[126] White, N. E., Nagase, F., Parmar, A. N. 1995, in Lewin, W. H. G., van Paradijs, J., van den Heuvel, E. P. J., X-ray Binaries, p.1-57, Cambridge University Press, Cambridge

[127] Wijers, R. A. M. J. and Pringle, J. E. 1999, MNRAS, 308, 207

[128] Wijnands, R. 2004, NuPhS, 132, 496

[129] Wilms, J., Nowak, M. A., Dove, J. B. et al. 1999, ApJ, 522, 460

[130] Winkler, C., Courvoisier, T. J. L., Di Cocco, G. et al. 2003, A&A, 441, L1

[131] Yi, I., Wheeler, J. C. and Vishniac, E. T. 1997, ApJ, 481, L51

[132] Yi, I. and Wheeler, J. C. 1998, ApJ, 498, 802

[133] Zel'Dovich, Y. B. and Shakura, N. I. 1969, SvA, 13, 175

APPENDIX A

LIGHT CURVES AND PULSE PROFILES OF *RXTE* OBSERVATIONS

In this appendix, light curves and energy resolved pulse profiles extracted from *RXTE - PCA* observations are presented. The light curves and pulse profiles of non-dipping observations are given in Figure A.1 and the light curves of dipping state observations are given in Figure A.2

All light curves in Figure A.1 and A.2 are 2 s long binned for a clear illustration which is written at the top right of the plots. Corresponding observation IDs are given at the top left and the start and stop times are given below the plots. In Figure A.2, source and dips are not separated in partial dip observations in order to allow one to compare the dipping and non-dipping states.

All energy resolved pulse profiles in Figure A.1 are given at the right of the corresponding light curve. The three energy bands (3 - 10 keV, 10 - 20 keV and 20 - 40 keV) related to the panels are given at the top left of each panel. The folded periods are given at the top right of the plots. As it is discussed in the text, dipping states do not show significant pulsed emission; therefore pulse profiles of dipping observations are not plotted.

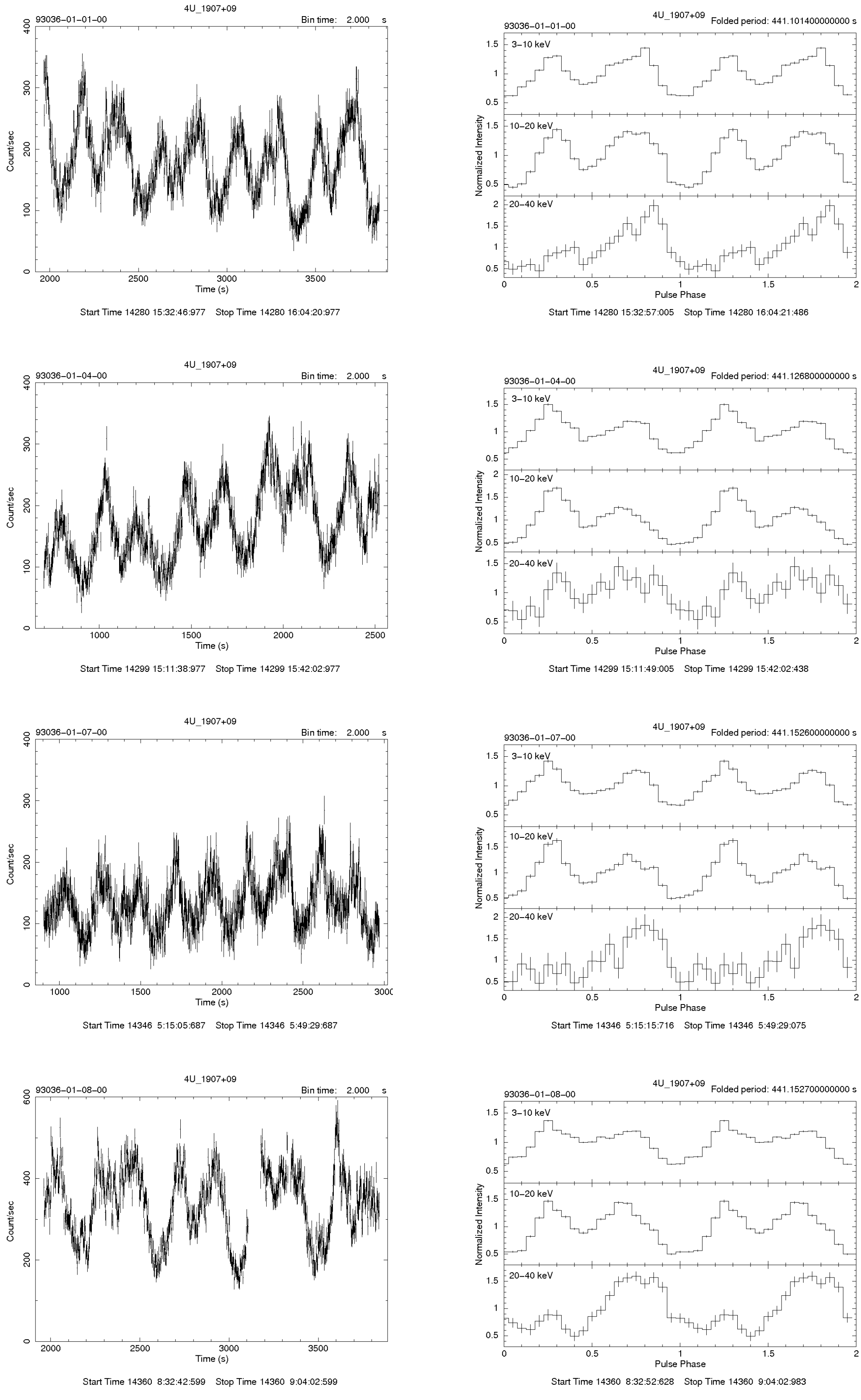

Figure A.1: Light curves and energy resolved pulse profiles of non-dip observations.

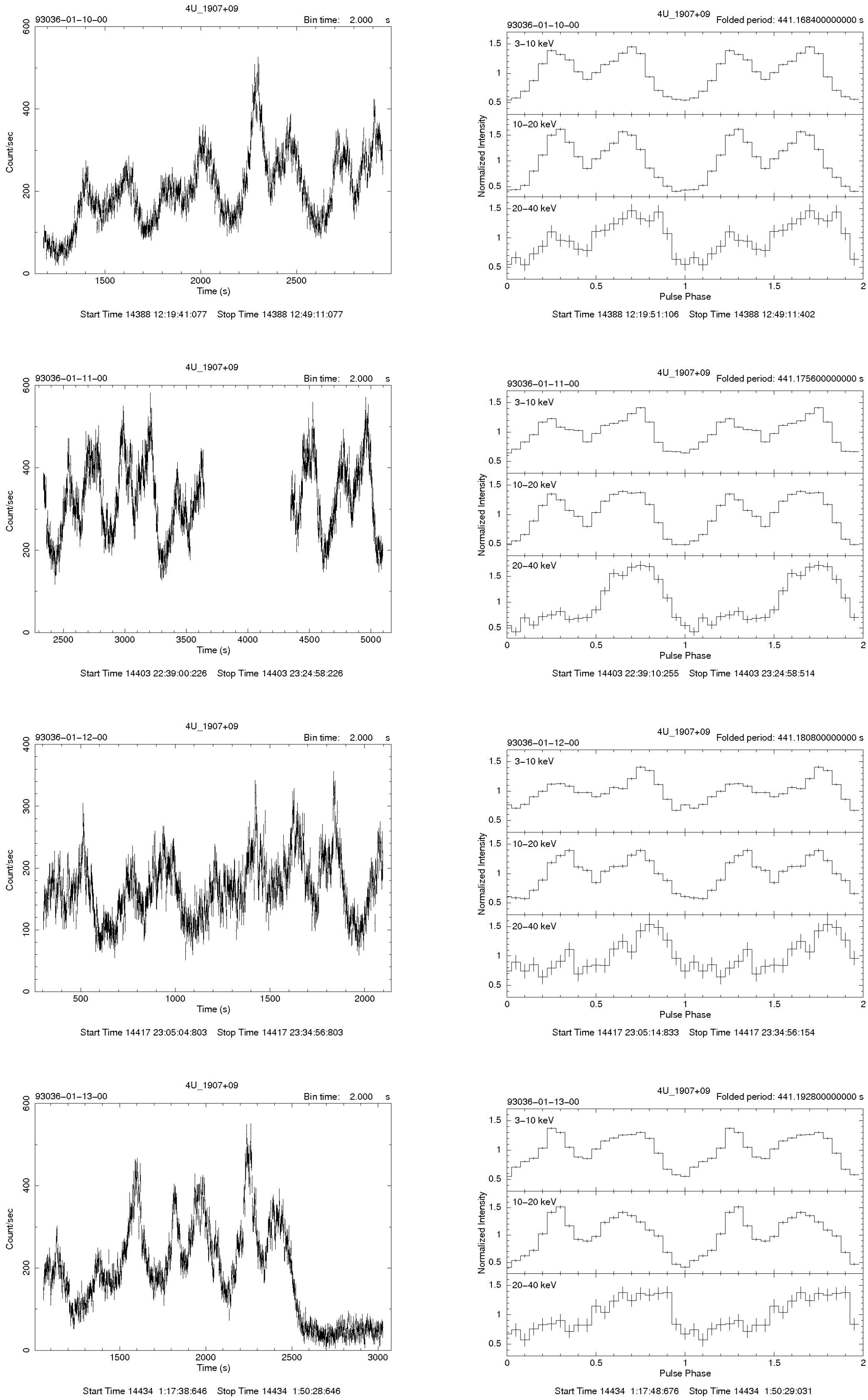

Figure A.1: (continued)

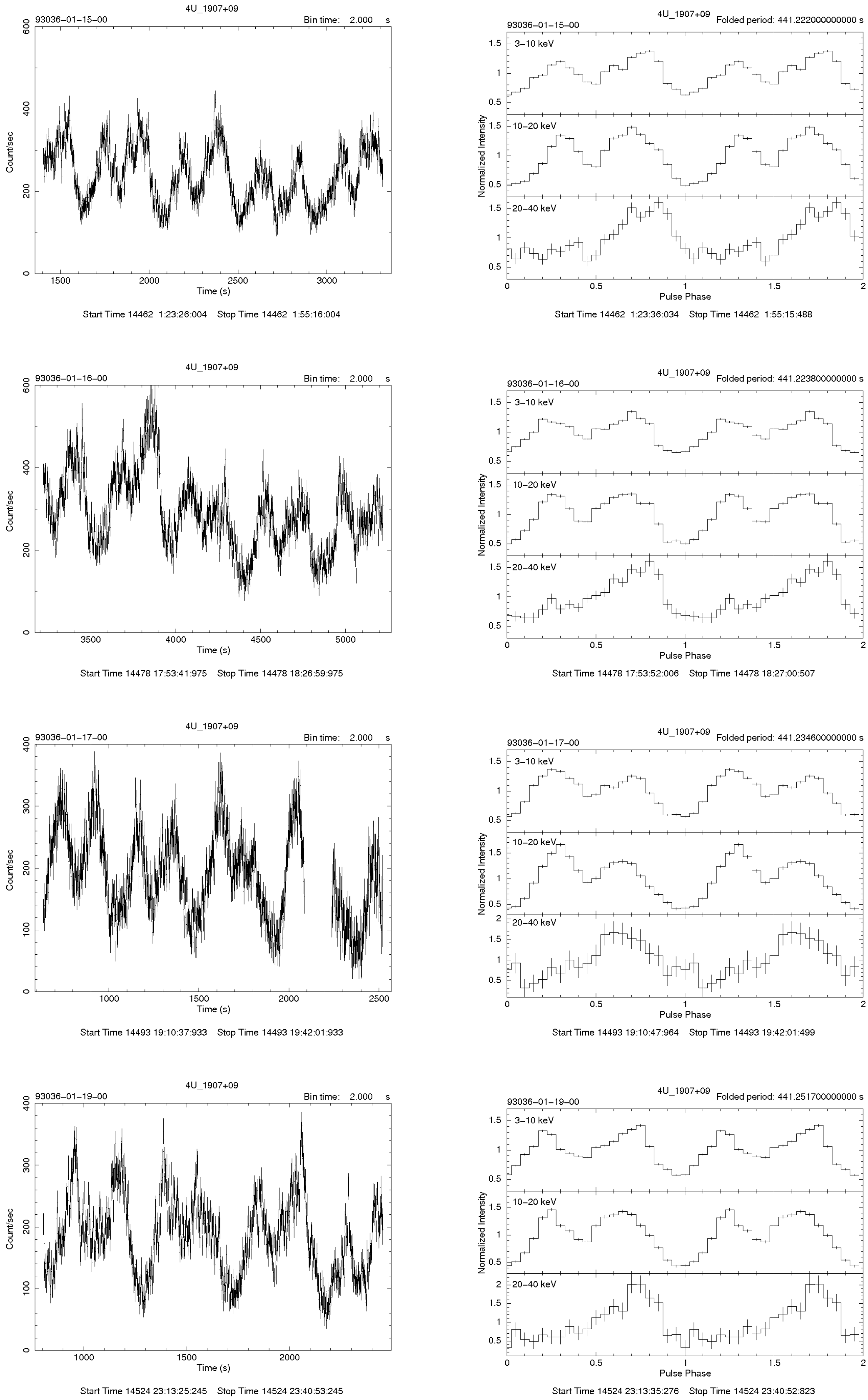

Figure A.1: (continued)

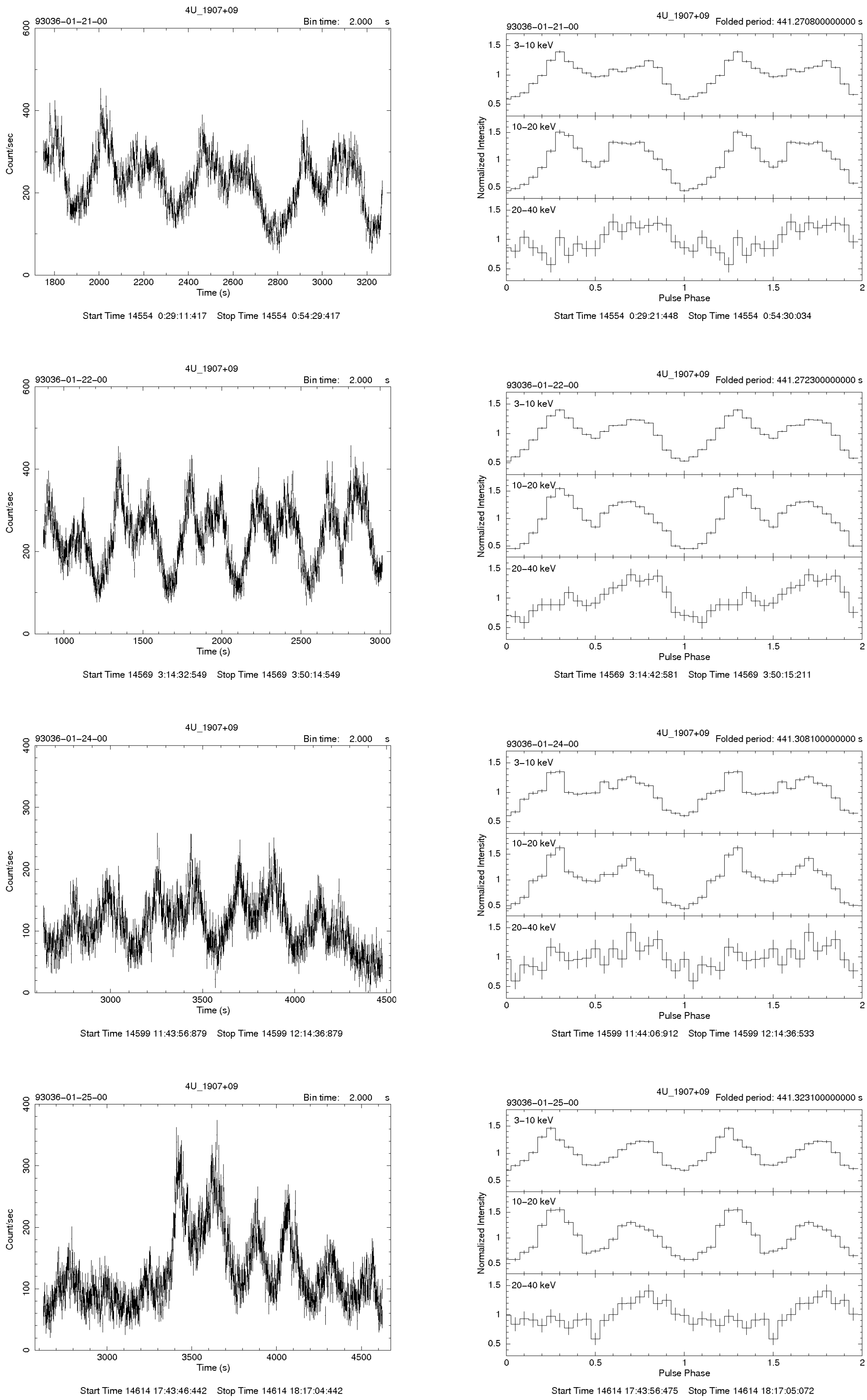

Figure A.1: (continued)

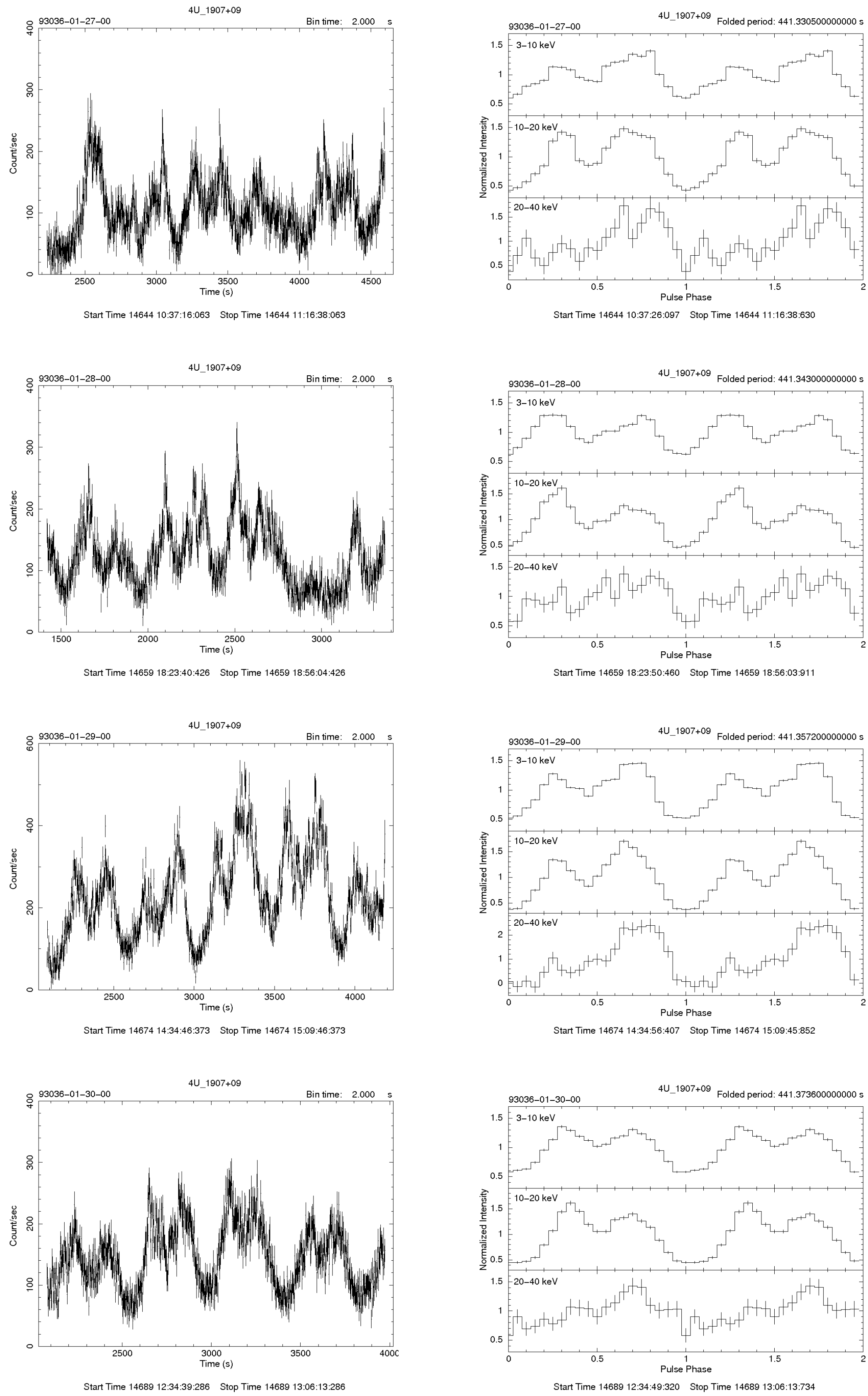

Figure A.1: (continued)

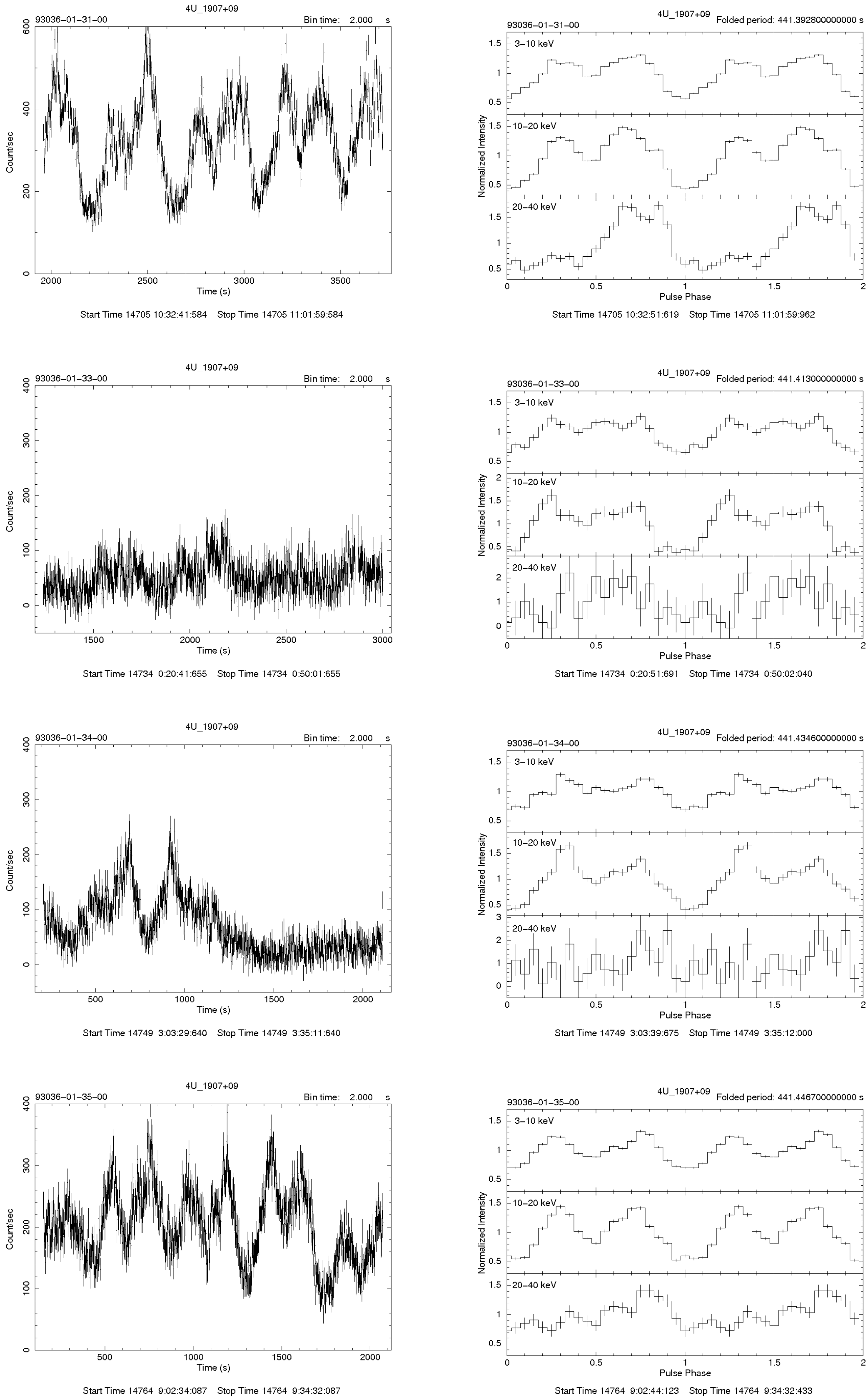

Figure A.1: (continued)

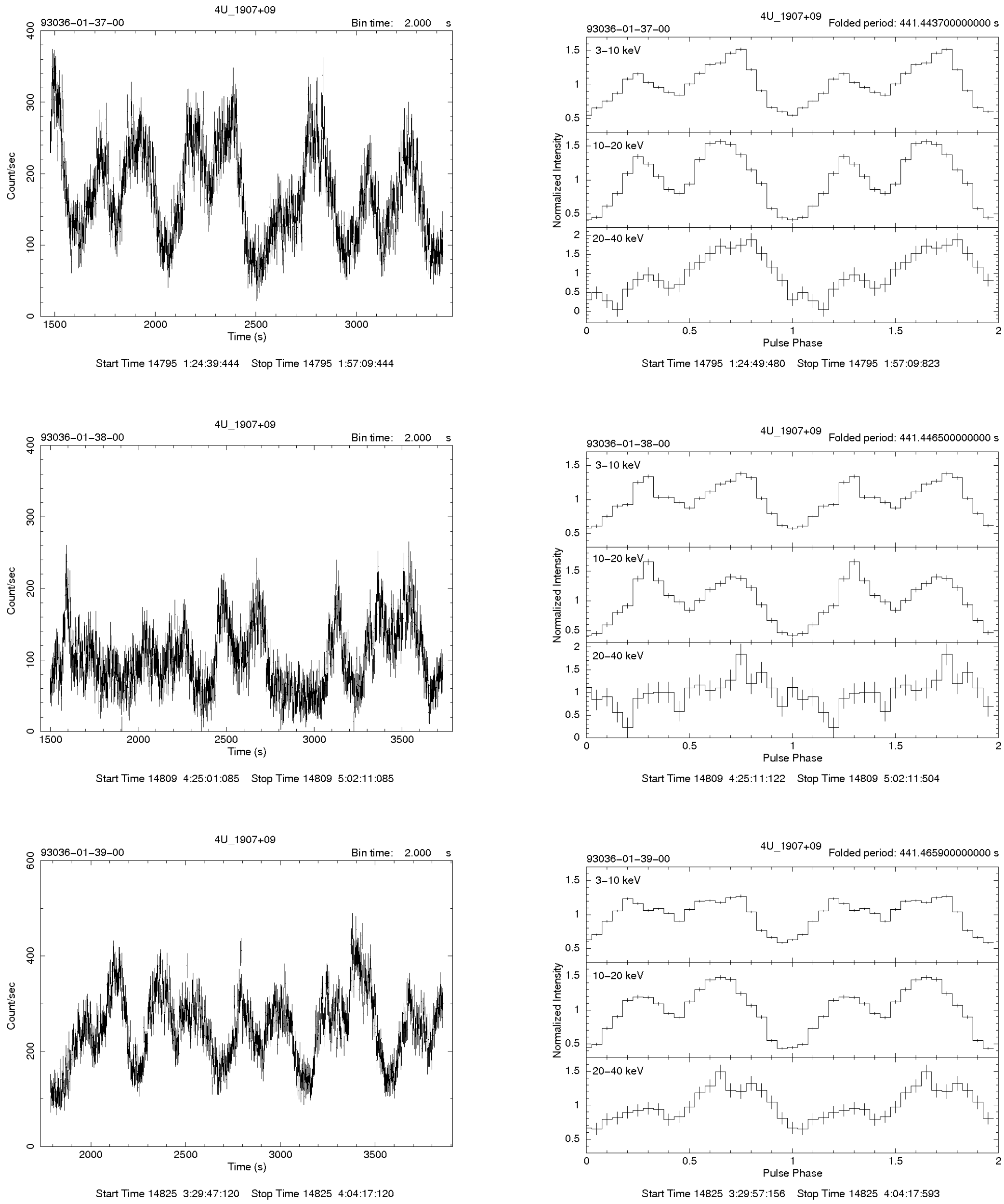

Figure A.1: (continued)

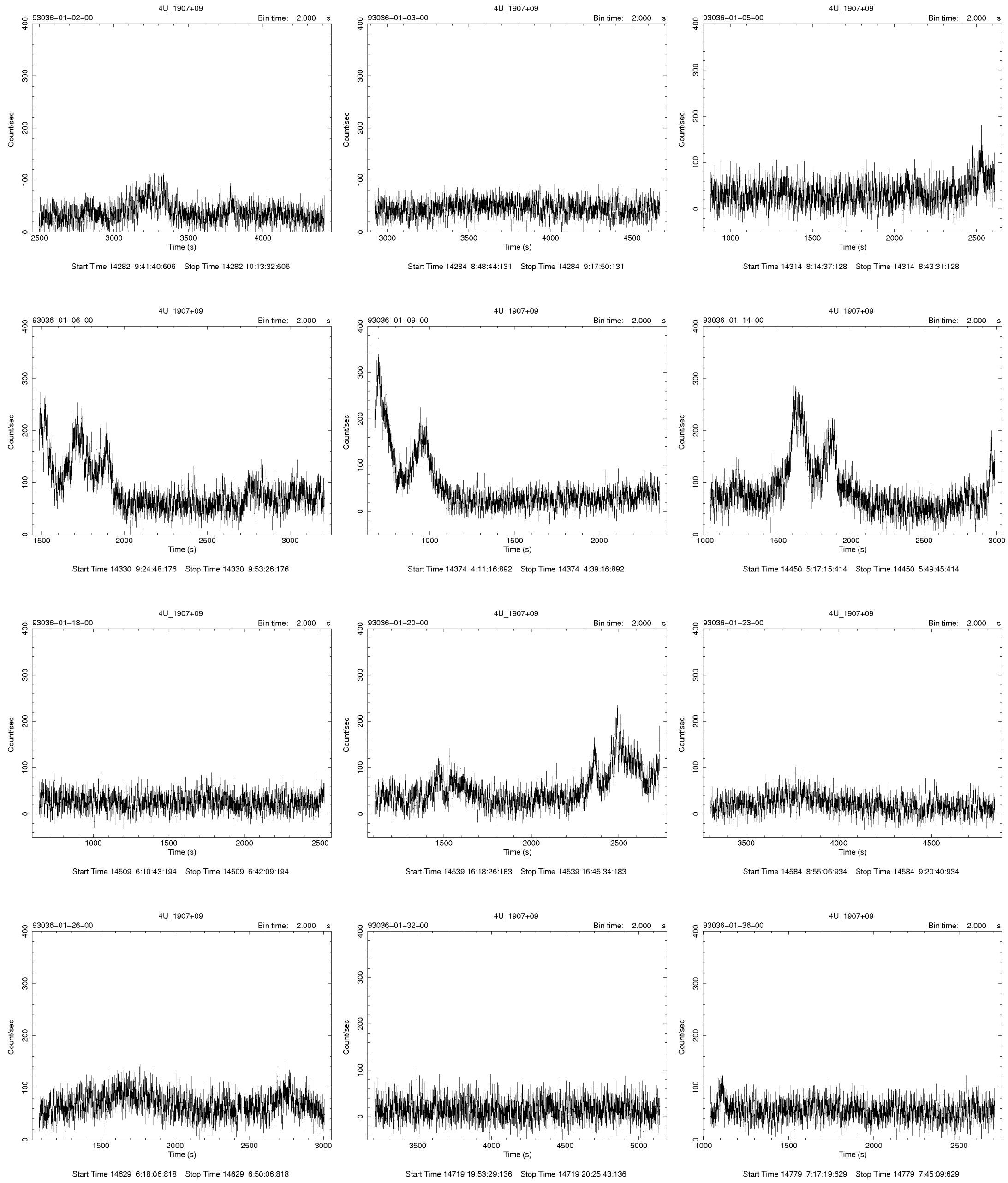

Figure A.2: Light curves of dipping state observations.

APPENDIX B

ENERGY SPECTRA OF NON-DIPPING *RXTE* OBSERVATIONS

In this appendix, energy spectra extracted from non-dipping *RXTE - PCA* observations are presented in Figure B.1. The observation IDs of the spectra are given at the top of the plots. The top panels of the plots show the data and best fit continuum model, whereas other two panels show the residuals of the fits for two different models. The middle panel shows the residuals of composite PL model and the bottom panel shows the residuals of the composite NPEX model.

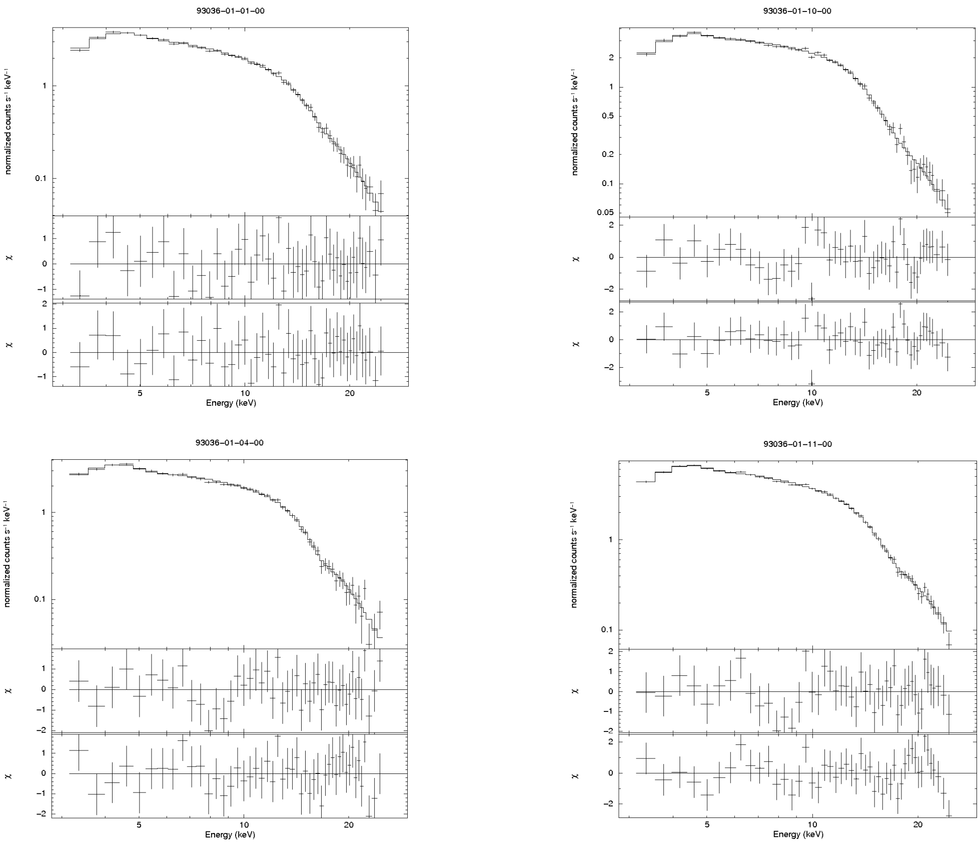

Figure B.1: Energy Spectra of non-dip observations fitted with two different models.

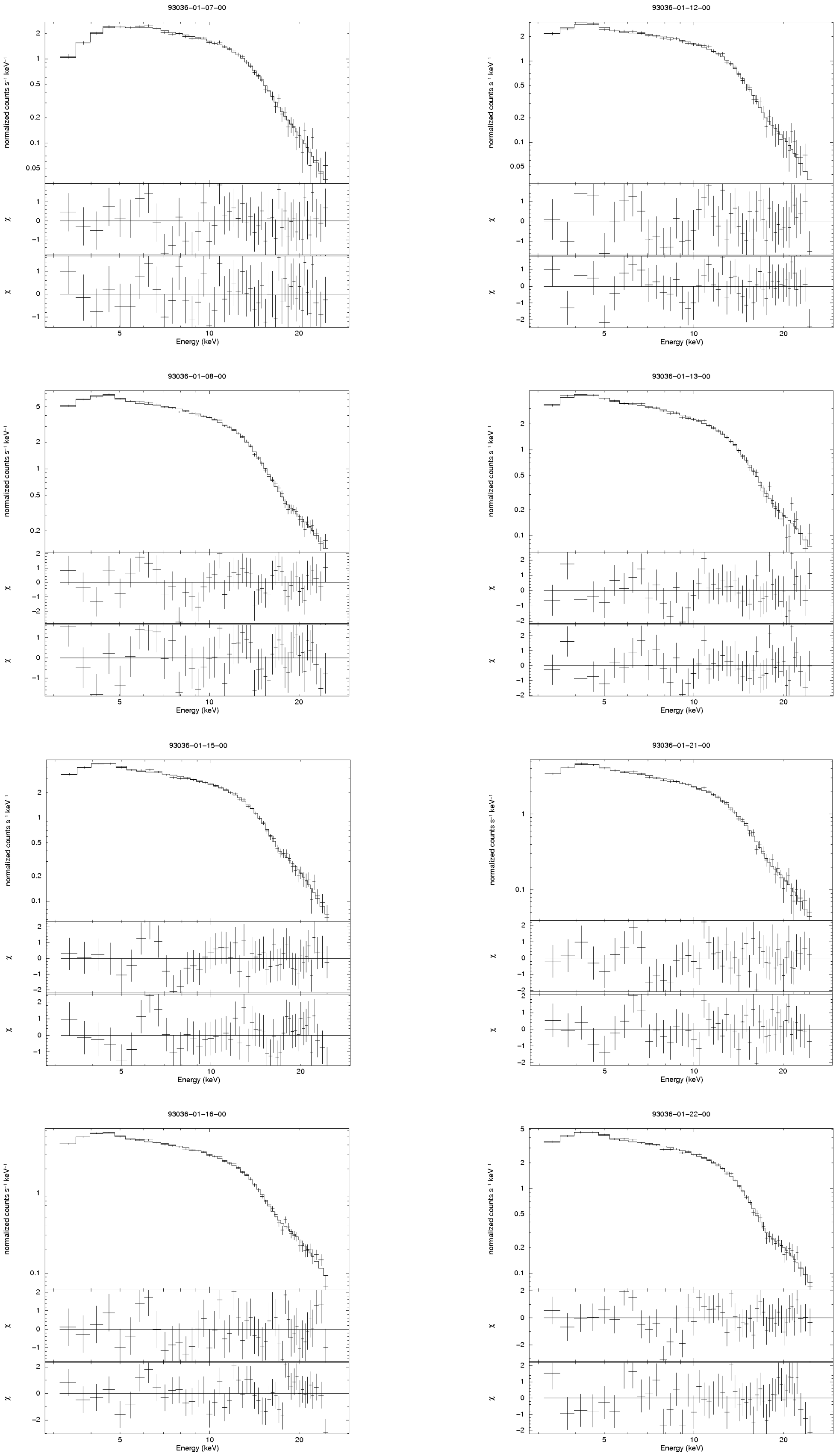

Figure B.1: (continued)

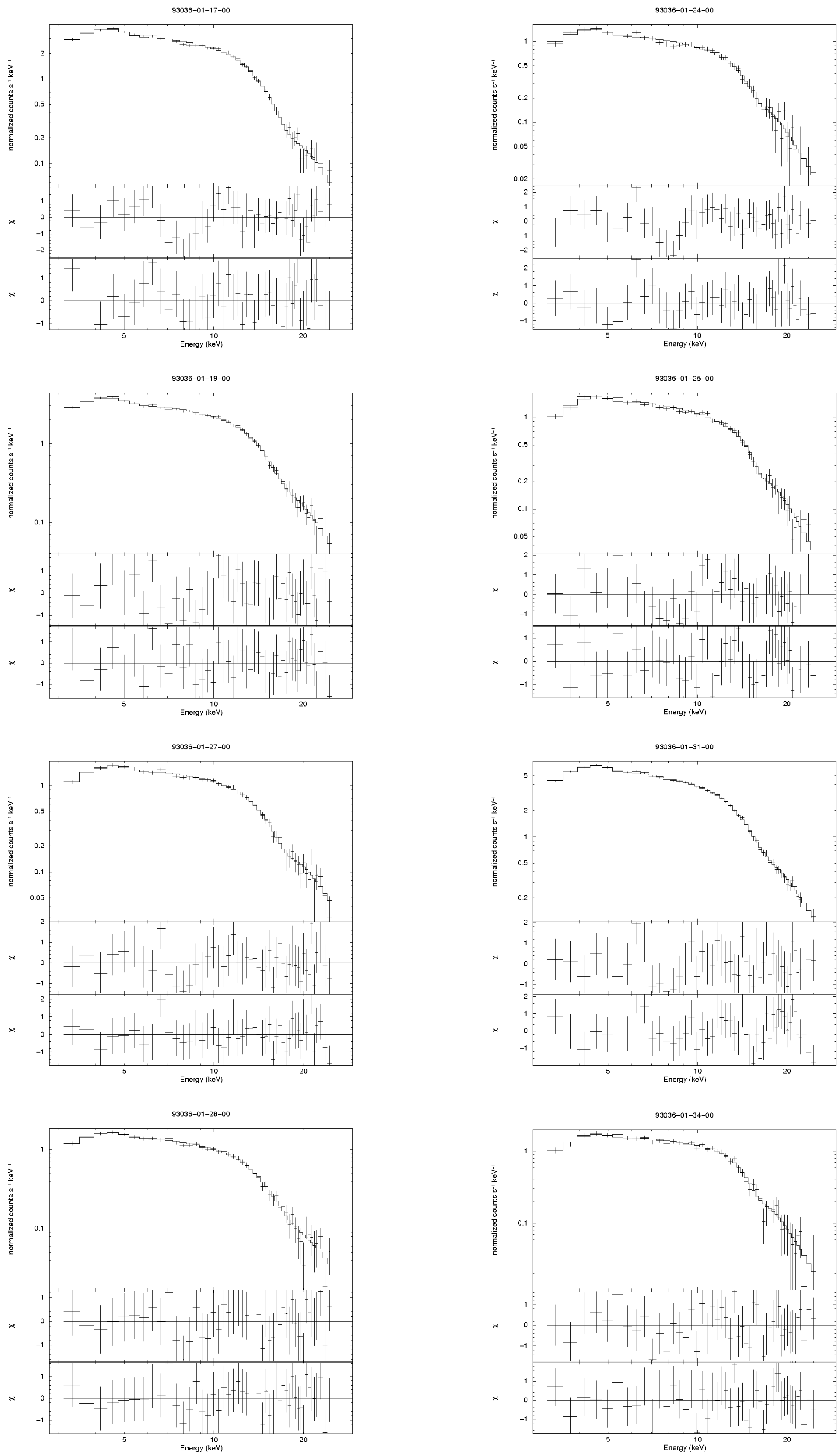

Figure B.1: (continued)

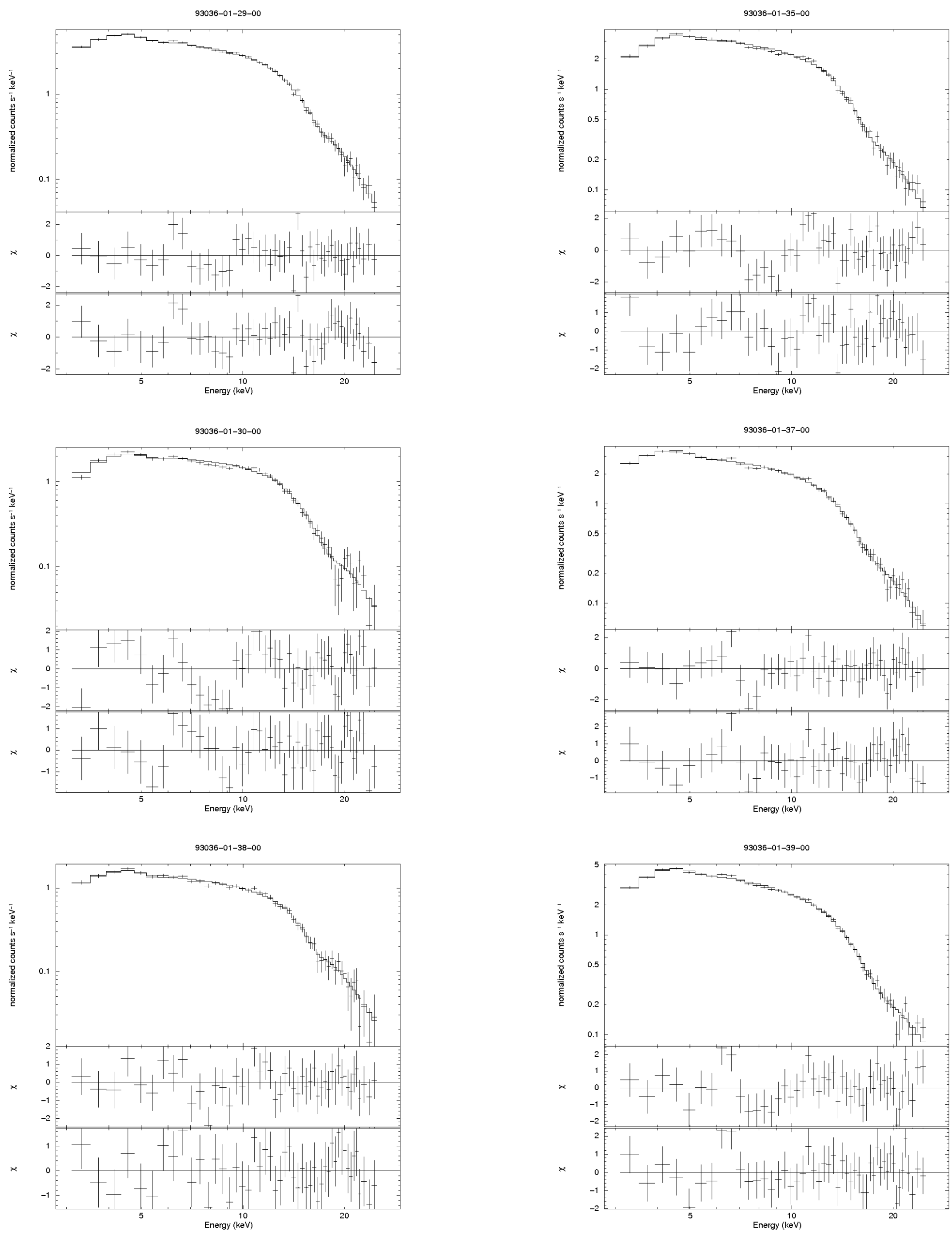

Figure B.1: (continued)